SHEAR TRANSFORMATION ZONES IN METALLIC GLASSES

by

Jong Doo Ju

A dissertation submitted in partial fulfillment
of the requirements for the degree of
Doctor of Philosophy
(Materials Science and Engineering)
in The university of Michigan
2014

Doctoral Committee:

Professor Michael Atzmon, Chair
Professor Ellen M. Arruda
Professor J. Wayne Jones
Adjunct Professor Anton Van der Ven

ACKNOWLEDGEMENTS

In the course of my Ph.D. study at the University of Michigan, I am indebted to many people for their boundless support, which has made a significant contribution directly or indirectly to the research. Without the support, this research would not have been valuable at this level. In this section, I would like to extend my gratitude to all those shortly.

I would foremost like to thank my advisor, Prof. Michael Atzmon. His intuition, insight and enthusiasm, which always inspired me, were invaluable. In addition, I appreciate not only for his guidance for the research, but also for his significant effort made for my academic writing and presentation. His guidance, along with the encouragement and support, were critical to make this research successful.

I am grateful to my committee members, Profs. Ellen M. Arruda, J. Wayne Jones and Anton Van der Ven, for providing comments and suggestions. Their questions on the research from different aspects of materials science were of great value and appreciated. Especially, it was a great pleasure to have individual discussions with Prof. Van der Ven, who made significant efforts to understand our research to provide valuable comments. In addition to the committee members, I also would like to express my special thanks to Prof. Frans A. Spaepen at Harvard University for sharing his wealth of knowledge and insight with us for our research.

I thank Dr. Dongchan Jang, who was a former member of our research group, for performing a number of cantilever bending measurements with great patience at California Institute of Technology. In addition, I deeply appreciate his invaluable encouragement to

stimulate me. I wish him success in his new career, as an assistant professor at Korea Advanced Institute of Science and Technology. I am also grateful to Dr. Amadi Nwankpa at Computer Aided Engineering Network for building computational framework for direct spectrum analysis, which was essential for our analysis of experimental data. It was a great pleasure to have discussions with him for the analysis, which allowed me to learn a great deal about the codes from him as well.

I thank wonderful administrative/technical staffs for their support in the department of both “Materials Science and Engineering” and “Nuclear Engineering and Radiological Sciences”. Especially, I am grateful to Renee Hilgendorf and Patti Vogel for their kind support/help that allowed me to focus on my research and teaching. They are experts in what they do, and nice people to boot. I would like to extend my gratitude to Profs. John Allison, Jinsang Kim and Steven Yalisove that I worked with as a graduate student instructor. Their enthusiasm for their teaching and research was an inspiration to my graduate studies.

Finally, I thank my father for his endless encouragement and support throughout my life. I never forget my grandmother and aunt, who raised me when I was a little kid and passed away. Their endless love was crucial to make this possible.

I am lucky to have met all these wonderful people, and am honored to have been a part of this research.

This work, and my education, were funded in part by NSF Grant No. DMR-0605911.

TABLES OF CONTENTS

CHAPTERS

LIST OF TABLES

Table

LIST OF FIGURES

Figure

LIST OF APPENDICES

APPENDIX

ABSTRACT

While mechanical behavior of crystalline materials has been well-understood in terms of lattice defects, metallic glasses pose significant challenges in defining the defects due to disordered structure. Physical/computational simulations have shown that equiaxed clusters, termed shear transformation zones (STZs), undergo shear transformations by atomic rearrangement in them to accommodate macroscopic strain. Properties of the STZs in amorphous $Al_{86.8}Ni_{3.7}Y_{9.5}$ were characterized using their anelasticity as a probe. A combination of cantilever bending and bend-stress relaxation measurements was employed to measure quasi-static anelastic strain over ~ 1 *sec.* – 8 × 10^7 *sec*. Direct spectrum analysis (DSA), the reliability of which was assessed with simulated data including noise, was performed to obtain the relaxation-time spectra. The spectra exhibit distinct peaks, which were analyzed in terms of the standard anelastic solid model with a linear combination of spring-dashpot, in conjunction with transition-state theory. The analysis provided the size of STZs: Active STZs consist of 14 – 21 atoms, resolved by a single atomic volume. The present model elucidates prior observations, (a) activation energy spectra obtained by the temperature-stepping method and (b) α and β relaxations in loss moduli.

The same STZ sizes were observed in both as-quenched and relaxed samples, suggesting that the activation energies are not altered by structural relaxation. The volume fraction of potential STZs (c_n), however, decreases substantially due to relaxation. These are interpreted in

terms of the free-volume model, modified to account for STZs as basic units. The resulting expression, fitted to c_n, indicates that ~ 2 % decrease in free-volume reduces c_n substantially, leading to a viscosity rise.

Published dynamic behavior of amorphous $Zr_{46.8}Ti_{8.2}Cu_{7.5}Ni_{10}Be_{27.5}$ was analyzed in order to evaluate the model used. DSA, performed with loss modulus data, yielded distinct peaks in the relaxation-time spectra, consistently for all data sets. The analysis of these spectra, employing simultaneous fits to account for Arrhenius behavior of respective time constants and their size-dependence, yielded STZs sizes of 25 – 33 atomic volumes. Compatibility of the size, attempt frequency and transformation strain of an STZ below and above T_g is noted. The characterized STZ volumes are part of a wider hierarchy, and the window observed is determined by the experimental conditions.

Chapter 1

INTRODUCTION

1.1 PROPERTIES OF METALLIC GLASSES

Metals lacking long-range atomic order were first reported 60 years ago.[1–3] Although they can be produced by various techniques, the underlying principle of the methods to achieve the disordered structure was rapid removal of energy below the crystallization temperature, bypassing crystal nucleation. Since the discovery of this new class of metallic materials, termed metallic glasses, progress has been made to explore solidification methods via rapid cooling, such as melt-spinning, physical vapor deposition or pulsed laser quenching. Cooling rates of the order of 10^5 to 10^{12} $K/sec.$ can be achieved by these techniques, which limit the typical thickness to $\leq \sim 100\ \mu m$.

As an alternative of producing metallic glasses, instead of enhancing the cooling efficiency, significant efforts have been made to lower the critical cooling rate for the metallic glass formation, thereby improving the glass forming ability. The discovery of alloy compositions for the bulk forming elemental combinations represents one of the impressive successes.[4,5] A wide variety of alloy systems have been investigated to find the bulk-glassy-forming metallic alloys, and some of the alloys were reported to solidify to an amorphous structure at cooling rates as low as 1 K/sec.[6,7]

Metallic glasses have received much attention from scientists due to their unique properties originating from the amorphous structure. Mechanical properties are among those distinct from those of the crystalline materials.[5,6,8] Metallic glasses show high compressive yield strength on the order of several *GPa* at room temperature. They exhibit larger elastic strain up to ~ 2 – 3 %, with elastic moduli comparable to those of crystalline alloys. Plastic deformation, however, is generally limited because of the flow localization in narrow shear bands due to work softening leading to fracture.

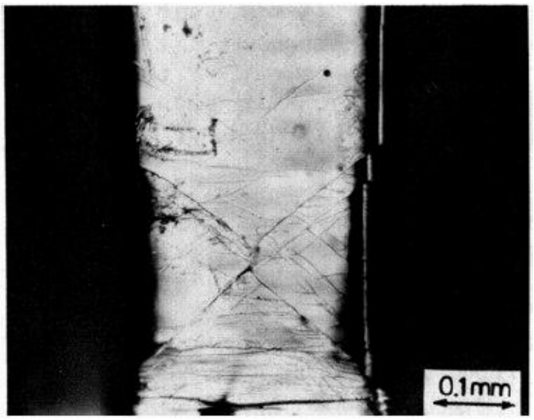

Figure 1.1 An optical micrograph of an as-quenched tensile specimen ($Pd_{78}Cu_6Si_{16}$ in *at.* %) loaded along the longitudinal direction at a constant strain rate of 10^{-4}/*sec*.[10]

Typical fracture of brittle metals during uniaxial tests occurs via flaw propagation along the direction perpendicular to the loading axis, where stress concentration at the crack tip is maximum. Experimental observations of shear banding angles, typically ~ 45 – 55° inclined to the loading direction, in metallic glasses, however, suggest the deformation is a shear process, and their limited strain to failure is attributed to the shear instability due to work softening.[9] Figure 1.1 shows the shear-band morphology of an amorphous $Pd_{78}Cu_6Si_{16}$ sample subjected to tensile test.[10] In addition, structural changes accompany the shear process, such as shear dilatation, as experimentally observed in preferential etching,[11] enhanced diffusion rate,[12] crystallization[13] and nanometer-scale voids formation[14] in the shear bands.

Even though plastic deformation of metallic glasses is generally limited because of flow localization in narrow shear bands, many studies have revealed that the strain to failure can be improved substantially by incorporating reinforcements into the glassy matrix, such as ductile crystalline particles.[15, 16] Recently, the $Pd_{79}Ag_{3.5}P_6Si_{9.5}Ge_2$ glass have been reported to demonstrate remarkable fracture toughness in excess of that of low-carbon steels by the extensive shear-band sliding near crack tips.[17]

In addition to their outstanding strength, flow in the metallic glasses has been of interest to many engineers. Their unique rheological properties at high temperature, near the supercooled liquid regime, allow for net-shape processing via direct casting or thermoplastic forming.[18,19] In order to employ these processing techniques for metallic glass forming alloys, however, challenges still remain, since crystallization in the supercooled liquid can significantly degrade their rheological properties. Therefore, experiments on the crystallization kinetics have been carried out extensively to study the optimum processing routes by constructing time-temperature-transformation diagrams for their applications.[20,21]

While experiments on the mechanical properties of metallic glasses have led to a wide range of industrial structural applications, fundamental studies on their deformation behavior are required to take advantage of their remarkable properties. Basic studies on mechanical behavior of crystalline materials by physicists and materials scientists have allowed for development of engineering materials through controlling defects, such as precipitates, grain boundaries and dislocations. Microscopic description at an atomic level that accounts for the deformation of metallic glasses, however, is extremely challenging due to the lack of atomic-scale periodicity in the matrix. The inherent disordered structure makes it difficult to characterize the deformation evolution on the atomic scale directly using electron microscopy as well, since there is no known contrast mechanism for imaging microscopic defects.

Attempts have been made to describe deformation of metallic glasses in terms of dislocation mechanics.[22] Subsequent investigations, however, have not supported the notion of dislocation-mediated deformation, even though a dislocation line may be created artificially by the classical procedure: an amorphous model can be displaced through making a planar cut by Burgers vector, followed by rejoining the displaced parts except for an extra half plane, the edge of which is a dislocation line. In fact, the Burgers vector, defined by making a close-circuit encompassing dislocation core, cannot be even clearly designated in an amorphous structure. Moreover, once an artificial dislocation is created in amorphous solids, because of the stress field existing around the dislocation core, it should be relaxed by consequent local rearrangements of atoms, made possible by the lack of translational symmetry, eliminating the supposed dislocation.[23] In addition, mechanical properties of amorphous materials are not determined by interactions between dislocations, as commonly observed in crystalline materials, which are strengthened when the dislocation density increases. In contrast, cold working does not strain harden metallic glasses.

Pioneering work that has triggered a wide range of fundamental studies on mechanical behavior of metallic glasses was published by Spaepen in the late 1970s.[24] Its model is based on the original study on the role of free volume in molecular transport by Cohen and Turnbull.[25] Spaepen’s model has expanded their study to derive constitutive equations for the deformation of metallic glasses, and the model has been successful in explaining a range of experimental observations including flow localization. Two years later, microscopic details on the deformation of metallic glasses were added by Argon,[26] based on a physical analogue, namely two-dimensional bubble rafts.[27] Analysis of the microscopic strain in sheared bubble rafts showed spatially distributed equiaxed clusters of bubbles that rearrange in response to the applied shear. These clusters were termed shear transformation zones (STZs). The STZs model introduced by Argon allows for a continuum description of deformation of amorphous solids. Recent experiments on 3-D colloidal glass as a physical analogue[28] and computer simulations[29] are in qualitative agreement with the 2-D bubble raft results. The two studies by Spaepen[24] and Argon[26] are still widely used for explaining mechanical properties of metallic glasses.

Deformation of metallic glasses shows diverse modes, and the characteristic behavior can be separated in terms of its reversibility and time-dependence. Under an applied stress, instantaneous elastic, i.e., reversible deformation is followed by time-dependent deformation. The time-dependent strain consists of two distinct components: anelasticity and viscoplasticity. While viscoplastic component leads to permanent deformation, anelastic strain is reversible.

A microscopic mechanism that results in the anelastic deformation of metallic glassses is attributed to the activation process of STZs by Argon as observed in bubble rafts experiments.[27,30] In addition, mapping local shear strain in sheared bubble rafts suggests that the STZs are spatially isolated at low strain, confined by their elastic surroundings.[27] Upon removal of the constraint, elastic back-stress reverses the isolated STZs, leading to anelasticity, whereas larger accumulation of the strain increases the sheared volume elements near the preexisting STZs, resulting loss of back stress and in irreversible viscoplasticity.

While low-temperature annealing of crystalline materials barely changes their physical properties, metallic glasses undergo structural relaxation during heat treatment. It results in densification, leading to dramatic property changes, such as atomic transport, electrical and magnetic properties.[31] For example, the viscosity increases significantly as a result of the structural relaxation.[32] Although its effects on physical properties of metallic glasses have been observed from many experiments, a microscopic mechanism governing structural relaxation is the subject of considerable debate.[33,34] While it is difficult to draw a clear conclusion for the mechanism of structural relaxation, it is clear that it involves annealing of defect sites. The challenge is to obtain both qualitative and quantitative information on these sites.

Cohen and Turnbulls' study provides a statistical description of the distribution of free volume in amorphous structure, and an expression for the probability that an atom can hop to a neighboring site for atomic transport.[25] The result has been incorporated by Spaepen,[24] and free volume fluctuation has been used as an important criterion for deformation sites: when the free volume associated with an atom is greater than a critical free volume, v^*, which is close to an atomic volume, a local transformation may result. Schematic illustration of an atomic jump suggested by Spaepen in an amorphous system is shown in Fig. 1.2.[24] Total probability of finding a hole of volume exceeding v^* is given by:

$$\int_{v^*}^{\infty} \frac{\gamma}{v_f} \exp\left(-\frac{\gamma v}{v_f}\right) dv = \exp\left(-\frac{\gamma v^*}{v_f}\right), \tag{1.1}$$

where v_f is the average free volume of an atom and γ is a geometrical factor between 1/2 and 1.[25]

The free volume criterion given in Eqn. (1.1) has been widely used to interpret a range of experimental data, especially for the effect of structural relaxation on diffusivity or shear viscosity of metallic glasses.[32,35–38] As an example of the observations, shear viscosity rise by orders of magnitude due to structural relaxation[32,37] has been attributed to the annihilation of free volume, e.g., by a bimolecular process.[33] Similarly, Egami[39,40] has suggested that recombination of two distinct deformable sites, in which negative and positive pressures are stored, results in the dramatic change in shear viscosity due to annealing. While no energy change during the redistribution of free volume among all the atoms has been assumed by Cohen and Turnbull,[25] Egami's model[41,42] is based on microscopic stresses acting on individual atoms observed in computer simulation studies.

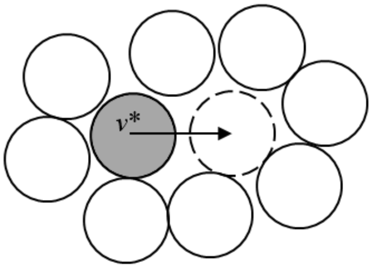

Figure 1.2 Schematic illustration of an atomic jump for diffusion or flow in an amorphous system.[24]

This dissertation addresses microscopic details for the deformation of metallic glasses with quantitative analyses of STZs using experimental results on anelastic relaxation. In order to measure the anelastic strain in a wide range of time spans, a combination of two experimental techniques, cantilever bending and bend-stress relaxation experiments, are employed. Details on the experimental procedures including underlying mechanics are discussed in Chapter 3. Using the experimental data, the direct spectrum analysis[43] has been performed to obtain the relaxation-time spectra. Surprisingly, the relaxation-time spectra show several distinct peaks for metallic glasses, which reveal a quantized hierarchy of STZs with increments of a single atomic volume, ranging from 14 to 21 atoms.

In addition to the quantized properties of STZs, the volume fraction of potential STZs is obtained. These are atomic clusters capable of undergoing shear transformations. While the volume of STZs and their quantized properties obtained from the relaxation-time spectra show less than one percent difference between as-quenched and relaxed samples, the volume fraction of potential STZs decreases substantially upon structural relaxation, leading to a viscosity rise. The annihilation of potential STZs have been interpreted in terms of the free volume model, modified to account for STZs as basic units. These analyses allow us to explore the microscopic mechanisms of changes in mechanical properties driven by structural relaxation in metallic glasses.

1.2 REFERENCES

[1.1] A. Brenner, D. D. Couch and E. K. Williams, *J. Res. Nat. Bur. Stds.* **44**, 109 (1950).
[1.2] W. Buckel and H. Hilsch, *Z. Phys.* **132**, 420 (1952).
[1.3] W. Klement, R. H. Willens, and P. Duwez, *Nature* **187**, 869 (1960).
[1.4] H. S. Chen, *Acta Metall*. **22**, 1505 (1974).
[1.5] C. A. Schuh, T. C. Hufnagel and U. Ramamurty, *Acta Mater*. **55**, 4067 (2007).
[1.6] W. L. Johnson, C. T. Liu and A. Inoue, Bulk metallic glasses, (*Materials Research Society*, Warrendale, PA 1999).
[1.7] H. W. Kui, A. L. Greer and D. Turnbull, *Appl. Phys. Lett*., **45**, 615 (1984).
[1.8] M. M. Trexler and N. N. Thadhani, *Prog. Mater. Sci*. **55**, 759 (2010).
[1.9] P. S. Steif, F. Spaepen and J. W. Hutchinson, *Acta Metall*. **30**, 447 (1982).
[1.10] H. Kimura and T. Masumoto, *Metall. Trans.* **A14**, 709 (1983).
[1.11] C. A. Pampillo, *Scripta Metall*. **6**, 915 (1972).
[1.12] J. Bokeloh,S. V. Divinski, G. Reglitz and G. Wilde, *Phy. Rev. Lett*. **107**, 235503 (2011).
[1.13] W. H. Jiang and M. Atzmon, *Acta Mater*. **51**, 4095 (2003).
[1.14] W. H. Jiang and M. Atzmon, *Scripta Mater*. **54**, 333, (2006).
[1.15] A. Inoue and X. M. Wang, *Acta Mater*. **48**, 1383 (2000).
[1.16] H. Choi-Yim, R. D. Conner, F. Szuecs and W. L. Johnson, *Acta Mater*. **50**, 2737 (2002).
[1.17] M. D. Demetriou, M. E. Launey, G. Garrett, J. P. Schramm, D. C. Hofmann, W. L. Johnson and R. O. Ritchie, *Nature Mater.* **10**, 123 (2011).
[1.18] N. Nishiyama and A. Inoue, *Mater. Trans., JIM* **40**, 64 (1999).
[1.19] J. Schroers, *J. of Metals* **57**, 35 (2005).
[1.20] J. Schroers, Y. Wu, R. Busch and W. L. Johnson, *Acta Mater*. **49**, 2773 (2001).
[1.21] M. D. Demetriou and W. L. Johnson, *Acta Mater*. **52**, 3403 (2004).

[1.22] J. J. Gilman, *J. Appl. Phys*. **44**, 675 (1973).
[1.23] F. Spaepen, *J. Non-Crys. Sol.* **31**, 207 (1978).
[1.24] F. Spaepen, *Acta Metall*. **25**, 407 (1977).
[1.25] M. H. Cohen and D. Turnbull, *J. Chem. Phys.* **31**, 1164 (1959).
[1.26] A. S. Argon, *Acta Metall*. **27**, 47 (1979).
[1.27] A. S. Argon and H. Y. Kuo, *Mater. Sci. Eng*. **39**, 101 (1979).
[1.28] P. Schall, D. Weitz, F. Spaepen, *Science* **318**, 1895 (2007).
[1.29] M. L. Falk and J. S. Langer, *Phy. Rev.* ***E*57**, 7192 (1998).
[1.30] A. S. Argon and L. T. Shi, *Acta Metall*. **4**, 499 (1983).
[1.31] F. E. Luborsky ed., *Amorphous metallic alloys*, Butterworths, (1983).
[1.32] A. I. Taub and F. Spaepen, *Acta Metall*. **28**, 1781(1980).
[1.33] F. Spaepen, *Scripta Mater*. **54**, 363 (2006).
[1.34] T. Egami, *Intermetallics* **14**, 882 (2006).
[1.35] D. Gupta, K. N. Tu and K. W. Asai, *Phys. Rev. Lett*. **35**, 796 (1975).
[1.36] H. S. Chen, L. C. Kimerling, J. M. Poate and W. L. Brown, *Appl. Phys. Lett*. **32**, 461 (1978).
[1.37] A. L. Greer and F. Spaepen, *Annals NY Acad. Sci.* **371**, 218 (1981).
[1.38] P. A. Duine, J. Sietsma and A. van den Beukel, *Acta Metall. Mater*. **40**, 743 (1992).
[1.39] T. Egami, *Prog. Mater. Sci*. **56**, 637 (2011).
[1.40] T. Egami, *J. Alloys Comp.* **509S**, S82 (2011).
[1.41] T. Egami, K. Maeda and V. Vitek, *Phil. Mag. A* **41**, 883 (1980).
[1.42] D. Srolovitz, K. Maeda, V. Vitek and T. Egami, *Phil. Mag.* ***A*44**, 847 (1981).
[1.43] J. R. Cost, *J. Appl. Phys.* **54**, 2137 (1983).

Chapter 2

BACKGROUND

The first section, 2.1, in this chapter comprises a review of anelasticity. The discussion in Section 2.1 begins with macroscopic time-dependent phenomena, in response to experimentally controlled mechanical variables. The mechanical variables can be quasi-static or dynamic, and depending on their types, the anelastic material shows distinct responses. Anelastic responses under quasi-static constraint are discussed in Section 2.1.1, and dynamic properties are discussed in Section 2.1.2.

The next section, 2.2, reviews microscopic mechanisms that allow for understanding of mechanical behavior of metallic glasses. Basic microscopic units that undergo strain to accommodate deformation are discussed in Section 2.2.1 in terms of shear transformation zones (STZs) and transition-state theory. The section is followed by discussion of the free volume theory, which was developed to determine the rate of atomic jumps for diffusion in metallic glasses,[1] and discussion of structural relaxation in Section 2.2.2. Finally, prior experimental determination of the activation energy spectrum for anelastic relaxation in metallic glasses is discussed in Section 2.2.3.[2]

2.1 ANELASTICITY

The term "anelasticity" refers to time-dependent, reversible relaxation of materials in response to external forces. The forces are not only stress or strain, but can also be electric or magnetic fields. In general, when a constant mechanical variable, e.g. a constant stress, is turned on, a material exhibits instantaneous strain followed by time-dependent strain. The instantaneous strain is termed elastic, and is usually expressed in terms of Hooke's law. Upon removal of the external stress, recovery of the elastic strain is instantaneous, but part or all of the remaining strain components is recovered in a time-dependent manner, a process termed anelasticity.

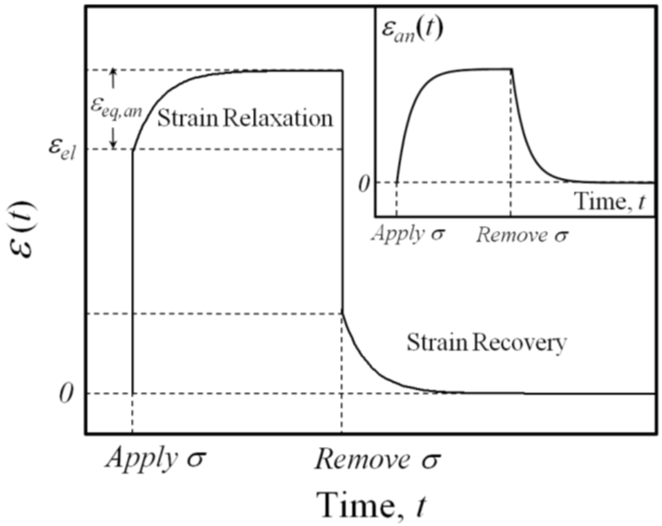

Figure 2.1 When a constant stress, σ, is turned on, instantaneous elastic strain (ε_{el}) is followed by the time-dependent anelastic strain $\varepsilon_{an}(t)$. The anelastic strain increases as a function of time, t, from zero to the equilibrium value ($\varepsilon_{eq.an}$). Upon removal of the external constraint, σ, the anelastic strain, ε_{an}, which depends on the prior constraining time, recovers as a function of time. The inset shows anelastic strain components only.

A schematic diagram of anelastic strain is given as a function of time in Fig. 2.1 for the case in which the entire time-dependent strain component is reversible. For many materials, the anelastic strain at a given time is linear in the external stress in the low stress regime.[3,4] The linearity of anelastic relaxation has been embodied in the Boltzmann superposition principle, and it has been observed in many relaxation experiments on metallic glasses as well.[5−7] Prior experimental studies on the anelastic properties of metallic glasses are discussed in Section 2.2.3.

2.1.1 QUASI-STATIC BEHAVIOR

When a mechanical variable, such as a constant stress, is applied to a material, it relaxes from the elastic equilibrium to its new equilibrium state by a continuous process of anelastic relaxation. While elastic equilibrium is achieved instantaneously, equilibration of the anelasticity is accompanied by time-dependent changes in states of mechanical variables, e.g., strain, that are conjugate to the experimentally controlled variables, such as stress. According to Nowick and Berry,[8] relaxation is termed as the self-adjustment of a thermodynamic system with time toward a new equilibrium state in response to a change in an external variable.

A time-dependent-stress-strain relation is used here to explain the deformation behavior of an anelastic solid. The anelastic model employed to derive expressions for this relation consists of springs and dashpots, as shown in Fig. 2.2. This model is termed the standard linear solid model.[8,9] It is assumed that there is no time-dependent permanent deformation. Subjected to a constant uniaxial stress, σ, a spring element accommodates instantaneous elastic strain, which is expressed in terms of Hooke's law:

$$\sigma = E\varepsilon , \tag{2.1}$$

where E is the elastic modulus and ε is the elastic strain. Unlike for the spring element, instantaneous deformation cannot be imposed on the dashpot element, because an infinite stress should be applied to the dashpot to achieve a step change in strain.[4] Instead, the dashpot exhibits linear viscous flow in response to the applied stress, as given by:

$$\sigma = 3\eta \frac{d\varepsilon}{dt}, \tag{2.2}$$

where η is the shear viscosity and $d\varepsilon / dt$ is the strain rate. The factor of 3 accounts for the conversion of unaxial to shear viscosity,[10] as derived in Appendix A. 1.

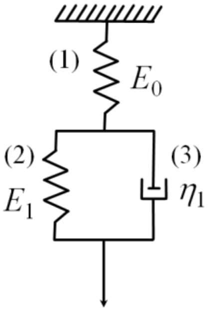

Figure 2.2 Standard linear solid model[8,9] consisting of a spring (1) in series with a parallel combination of a spring (2) and a dashpot (3), termed a Voigt unit. The spring element in (1) accounts for instantaneous deformation, while the Voigt unit exhibits anelasticity.

For introductory purpose, the model depicted in Fig. 2.2 assumes a single process. Expressions for the time-dependent strain for a combination of the springs and dashpots are useful in analyzing experimental data on anelastic properties of materials. In fact, the standard linear solid model illustrated in Fig. 2.2 is of basic importance since it can help explain experimental data at a microscopic level. For example, the model has been incorporated into dislocation models to explain the mechanisms of internal friction in crystalline thin films.[11] An application of the model to the interpretation of anelasticity of a metallic glass will be discussed in Chapter 4 in detail.

When the anelastic solid model is subjected to a constant stress, the stress is first predominantly sustained by the dashpot element in a Voigt unit, as illustrated in Fig. 2.1. As time elapses, however, the stress is transferred to the spring (2) as the dashpot (3) undergoes deformation. Mechanical equilibrium is achieved when the stress is completely transferred to the spring element. At this point, the stress reaches a steady state.

Expressions for the time-dependent deformation of the model in Fig. 2.2 can be derived starting from the relations between properties of each element and those of the model system, such as applied stress: σ and total strain: ε. The relations are given by:

$$\begin{aligned}\sigma &= \sigma_{(1)} = \sigma_{(2)} + \sigma_{(3)} \\ \varepsilon &= \varepsilon_{(1)} + \varepsilon_{(2)} = \varepsilon_{(1)} + \varepsilon_{(3)}\end{aligned}, \tag{2.3}$$

where the subscripts (i) refer to the corresponding elements. Recalling Eqns. (2.1) and Eqn. (2.2), a differential equation for the anelastic model is obtained from Eqn. (2.3), eliminating all $\sigma_{(i)}$ and $\varepsilon_{(i)}$:

$$\sigma\left(1+\frac{E_1}{E_0}\right)+\frac{3\eta_1}{E_0}\left(\frac{d\sigma}{dt}\right)=E_1\,\varepsilon+3\eta_1\left(\frac{d\varepsilon}{dt}\right), \tag{2.4}$$

where E_1 is the effective modulus, η_1 is the effective shear viscosity and E_0 is Young's modulus of the material. A solution to Eqn. (2.4) is obtained for strain relaxation under a constant external stress. If σ is switched on at $t = 0$, with instantaneous strain, ε_0:

$$\varepsilon(t)=\sigma\left\{\frac{1}{E_0}+\frac{1}{E_1}\left(1-\exp\left[-\frac{t}{\tau}\right]\right)\right\}=\varepsilon_0+\frac{\sigma}{E_1}\left(1-\exp\left[-\frac{t}{\tau}\right]\right)\equiv\varepsilon_0+\varepsilon_{an}(t), \tag{2.5}$$

where $\varepsilon_0 = \dfrac{\sigma}{E_0}$, $\tau = \dfrac{3\eta_1}{E_1}$ is the relaxation time constant, $\varepsilon_{an}(t)$ is the anelastic component of the strain. When the loading time, t, reaches τ, the anelastic strain increases to $(1\text{-}e^{-1})$ of its equilibrium value, which corresponds to ~ 63% of the strain. The equilibrium anelastic strain that is achieved after $t >> \tau$ is given by: $\varepsilon_{eq,an} = \dfrac{\sigma}{E_1}$. Equation (2.5) shows the linearity of elastic and anelastic strain in the applied stress.

Upon removal of the constraint at $t = 0$, an instantaneous elastic recovery by the spring (1) is followed by the anelastic strain recovery, as illustrated in Fig. 2.1. The equilibration process of anelastic recovery is achieved as the dashpot element that predominantly sustains the elastic stress flows until the stresses stored in both the dashpot (3) and spring (2) vanishes. An expression for the strain recovery can be also formulated from Eqn. (2.4) at $\sigma = 0$:

$$\varepsilon_{an,sf}(t) = \varepsilon_{an}(t_c)\exp\left[-\frac{t}{\tau}\right], \tag{2.6}$$

where $\varepsilon_{an}(t_c)$ is the anelastic strain developed under a constant stress for time t_c. If t_c is large enough so that $\varepsilon_{an}(t_c)$ is close to its equilibrium value, the subsequent initial stress-free relaxation rate is equal to those at the constant stress. However, if the system is constrained for a duration $t_c << \tau$, the subsequent strain relaxation rate is smaller than that under constraint by a factor of t_c/τ.[10]

2.1.2 DYNAMIC BEHAVIOR[3,4,8]

Quasi-static experiments, introduced in Section 2.1.1, allow for exploring anelastic properties in a range of time scales, from sub-seconds up to years. Another experimental technique that is widely used to measure anelasticity involves dynamic experiments: an oscillatory mechanical variable is applied and the material response is measured as a function of frequency. Although problems associated with accuracy, sensitivity and stability of instrumentation are more difficult to resolve in a dynamic than a quasi-static experiment, it is useful in measuring anelastic response at a wide range of sub-millisecond time constants, which are relevant to, e.g., impact tests.

When a periodic stress with constant amplitude is imposed on the anelastic solid, there is a phase lag of strain behind the stress. An example of the strain lag in response to the sinusoidal stress is schematically plotted in Fig. 2.3. If the applied stress has a single frequency, an expression for the period stress is given by:

$$\sigma = \sigma_0 e^{i\omega t}, \tag{2.7}$$

where σ_0 is the stress amplitude and ω is the angular frequency: $\omega = 2\pi f$, where f is the cycle frequency.

Linear anelastic solids show two characteristic steady-state strain responses in dynamic experiments. First, the strain amplitude, $\varepsilon_{0,osc}(\omega)$, is linear in the applied stress amplitude, σ_0. Second, the strain oscillates at the same frequency as that of the periodic stress as shown in Fig. 2.3. The strain is given by:

$$\varepsilon = \varepsilon_{0,osc}(\omega) e^{i(\omega t - \delta)}, \tag{2.8}$$

where δ is the phase lag angle, also called the loss angle, and is a material property.

The strain in Eqn. (2.8) is a sum of two distinct strain components in the complex plane. Since $e^{-i\delta}$ is equal to (cos $\delta - i$ sin δ), it can be rewritten as:

$$\varepsilon = \varepsilon_{0,osc}(\omega)(\cos\delta - i\sin\delta)e^{i\omega t} = (\varepsilon_{0,1}(\omega) - i\,\varepsilon_{0,2}(\omega))e^{i\omega t}, \tag{2.9}$$

where $\varepsilon_{0,1}(\omega) = \varepsilon_{0,osc}(\omega)\cos\delta$ and $\varepsilon_{0,2}(\omega) = \varepsilon_{0,osc}(\omega)\sin\delta$ are the real and imaginary parts of $\varepsilon_{0,osc}(\omega)$ on the complex plane. While $\varepsilon_{0,1}(\omega)$ is in phase with the periodic stress, $\varepsilon_{0,2}(\omega)$ is 90^o out of phase: $\tan(\delta) = \varepsilon_{0,2}(\omega)/\varepsilon_{0,1}(\omega)$.

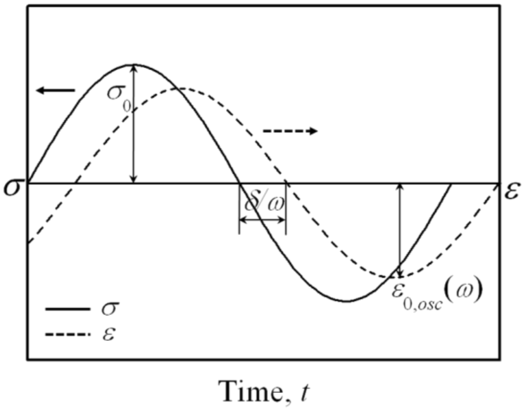

Figure 2.3 Schematic plots of strain, ε, lagging behind the periodic stress, σ, by a phase lag angle, δ. σ_0 and $\varepsilon_{0,osc}(\omega)$ are the amplitudes of the oscillating σ and ε, respectively.

Since ε consists of a real and imaginary part, Eqn. (2.9) can be simplified in terms of the in-phase and out-of-phase strains as a function of angular frequency:

$$(\varepsilon_{0,1}(\omega) - i\,\varepsilon_{0,2}(\omega))e^{i\omega t} = \varepsilon_1(\omega) - i\,\varepsilon_2(\omega), \tag{2.10}$$

where $\varepsilon_1(\omega)$ is termed the storage strain and $\varepsilon_2(\omega)$ the loss strain.

The storage and loss strains are of physical significance since they are associated with the specific energies stored and dissipated during cyclic work, respectively.[3,4,8] While the dissipated energy per cycle in a unit volume (ΔW) is equal to the work done ($\sigma\,\mathrm{d}\varepsilon$) by an anelastic solid over a complete cycle (the energy lost per cycle), the maximum stored energy (W) in a cycle is equal to the ideal elastic work without the phase lag, δ. These specific energies and their relationships with ε_1 and ε_2 are given by:

$$\begin{aligned} \Delta W &= \oint \sigma\, d\varepsilon = \int_0^T \sigma_0 \cos(\omega t)\, \varepsilon_{0,osc}(\omega)\, \omega \sin(\delta - \omega t)\, dt = \pi\, \sigma_0\, \varepsilon_{0,osc}(\omega) \sin(\delta) = \pi\, \sigma_0\, \varepsilon_{0,2}(\omega) \\ W &= \int_0^{T/4} \sigma\, d\varepsilon = \int_0^{T/4} \sigma_0 \cos(\omega t)\, \varepsilon_{0,osc}(\omega)\, \omega \sin(\omega t)\, dt = \frac{\sigma_0\, \varepsilon_{0,osc}(\omega)}{2} \end{aligned}, \tag{2.11}$$

where $T = \dfrac{2\pi}{\omega}$ is the period of the oscillation.

The specific damping capacity (SDC), defined as $\Delta W/W$, is a measure of a material's ability to reduce amplitudes of oscillation in a vibrating system. It is given by:

$$\frac{\Delta W}{W} = 2\pi \frac{\varepsilon_{0,2}(\omega)}{\varepsilon_{0,osc}(\omega)} = 2\pi \sin(\delta)\,. \tag{2.12}$$

Since δ is a measure of the damping capacity, it is often called the internal friction of a material.[8] Note that SDC is independent of stress or strain but is a function of the phase lag angle, δ.

In order to obtain expressions for the storage and loss strain under applied periodic stress for the standard anelastic solid model, Eqns. (2.7) and (2.9) are substituted into Eqn. (2.4):

$$\sigma_0\, e^{i\omega t}\left(1 + \frac{E_1}{E_0}\right) + \frac{3\eta_1}{E_0}(\sigma_0\, e^{i\omega t}\, i\,\omega) = E_1(\varepsilon_1 - i\,\varepsilon_2)e^{i\omega t} + 3\eta_1(\varepsilon_1 - i\,\varepsilon_2)e^{i\omega t}\, i\,\omega\,. \tag{2.13}$$

When Eqn. (2.13) is reorganized in terms of real and imaginary components that are in phase and out of phase with the periodic stress, respectively, as given in Eqn. (2.10), the storage and loss strains are obtained, respectively:

$$\varepsilon_1(\omega) = \frac{\sigma_0}{E_0} + \frac{\sigma_0}{E_1}\frac{1}{1+\omega^2\tau^2} \tag{2.14}$$

$$\varepsilon_2(\omega) = \frac{\sigma_0}{E_1}\frac{\omega\tau}{1+\omega^2\tau^2}\,. \tag{2.15}$$

Figure 2.4 shows schematic plots of storage, loss strains and their ratio, tan(δ), as a function of angular frequency, ln(ω). At high frequency of applied periodic stress, the anelastic strain is negligible because of the short time allowed for a material to show anelastic response to the high frequency stress, resulting in low storage and loss strain. On the other hand, when the stress frequency is very low, time for an anelastic solid to respond is long enough to achieve an equilibrium anelastic strain. The loss strain, however, is also low at low frequency, because the energy loss for both extreme frequency ranges is negligible. Therefore, the storage strain in the high frequency regime is equal to the elastic strain, $\varepsilon_0 = \sigma_0/E_0$, and it approaches an equilibrium value, $\varepsilon_{eq,an} = \sigma_0/E_1$, with decreasing angular frequency. The loss strain shows a peak at $\omega = 1/\tau$, called a Debye peak.[6] The peak of phase angle, tan (δ), appears at $\omega_{p,\tan(\delta)} = \frac{1}{\tau}\sqrt{\frac{\varepsilon_0 + \varepsilon_{eq,an}}{\varepsilon_0}} > 1/\tau$, and its height is $\frac{1}{2}\frac{\varepsilon_{eq,an}}{\sqrt{\varepsilon_0(\varepsilon_0 + \varepsilon_{eq,an})}}$.

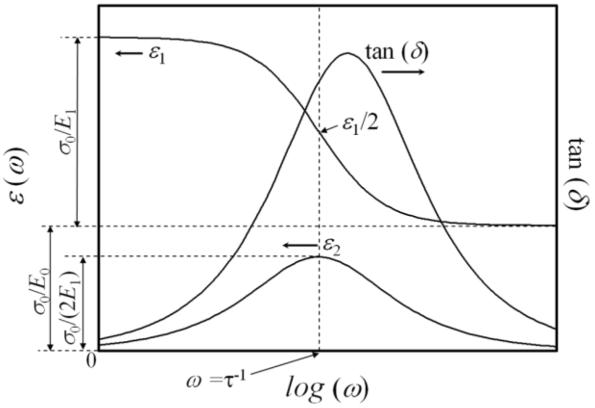

Figure 2.4 Schematic plots of the storage strain, $\varepsilon_1(\omega)$, loss strain, $\varepsilon_2(\omega)$, and their ratio, tan (δ) for the standard anelastic solid. While $\varepsilon_2(\omega)$ is symmetric with respect to ln(ω) and shows a peak at $\omega = 1/\tau$, $\varepsilon_1(\omega)$ decreases from ($\varepsilon_0 + \varepsilon_{eq,an}$) to ε_0 as a function of ω.

For simple Arrhenius behavior with a single activation energy, ΔE_a, the time constant, τ, at temperature T can be directly obtained experimentally from the peak in loss strain measured as a function of frequency, since the peak position is given by $\omega_p = 1/\tau$. Similarly, the activation energy can be estimated from the peak in loss strain measured at fixed frequency as a function of temperature as well. Assuming that $\tau(T)$ is expressible by an Arrhenius relation:

$$\tau(T) = \tau_0 \, e^{-\Delta E_a / kT} , \tag{2.16}$$

where τ_0 is the pre-exponential factor, k is the Boltzmann constant and ΔE_a is the activation energy, the loss strain at fixed angular frequency shows a peak at absolute temperature, $T_P = -\Delta E_a / (k \ln[\tau_0 \, \omega])$, which is symmetric with respect to the reciprocal absolute temperature, T^{-1}.

Instead of measuring the strain response to periodic stress, dynamic properties can also be measured by monitoring the stress response under oscillating strain. Since strain is controlled experimentally, the complex stress, which is a sum of a real and imaginary component, σ_1 and σ_2, is obtained. The stress components in response to experimentally controlled periodic strain, $\varepsilon = \varepsilon_0 \, e^{i\omega t}$, are given by:

$$\sigma = \sigma_{0,osc}(\omega) \, e^{i(\omega t - \delta)} = (\sigma_{0,1}(\omega) - i\,\sigma_{0,2}(\omega))\, e^{i\omega t} = \sigma_1(\omega) - i\,\sigma_2(\omega) , \tag{2.17}$$

where $\sigma_1(\omega) = \sigma_{0,osc}(\omega) \cos\delta$ and $\sigma_2(\omega) = \sigma_{0,osc}(\omega) \sin(\delta)$, which are the amplitudes of the real and imaginary components of $\sigma_{0,osc}(\omega)$. While $\sigma_1(\omega)$ is in phase with the periodic stress, σ, $\sigma_2(\omega)$ is 90^o out of phase, yielding $\tan(\delta) = \sigma_2/\sigma_1$. When $\sigma_1(\omega)$ and $\sigma_2(\omega)$ are normalized by the amplitude of the oscillating strain, ε_0, the storage (E') and loss moduli (E'') are obtained. In order to obtain expressions for the complex moduli, it is convenient to employ a Maxwell unit, which consists of a spring (2) in series with a dashpot (3), the elastic modulus and shear modulus of which are $E_{1,\mathrm{M}}$ and $\eta_{1,\mathrm{M}}$, respectively, attached in parallel to a spring element (1). Schematic illustration of this model is given in Fig. 2.5 (a). Note that this model is equivalent to the standard linear solid model in Fig. 2.2 under periodic stress. $E'(\omega)$ and $E''(\omega)$, derived from the model system, are given by:

$$E'(\omega) = \frac{\sigma_1(\omega)}{\varepsilon_0} = E_{0,M} + E_{1,M}\,\frac{\omega^2\,\tau^2}{1+\omega^2\,\tau^2} \tag{2.18}$$

$$E''(\omega) = \frac{\sigma_2(\omega)}{\varepsilon_0} = E_{1,M}\,\frac{\omega\,\tau}{1+\omega^2\,\tau^2}\,, \tag{2.19}$$

where $\tau = \frac{3\eta_{1,M}}{E_{1,M}}$. In addition to the storage and loss moduli in Eqn. (2.18) and (2.19), their ratio, $\tan(\delta)$, is plotted as a function of ω in Fig. 2.5 (b).

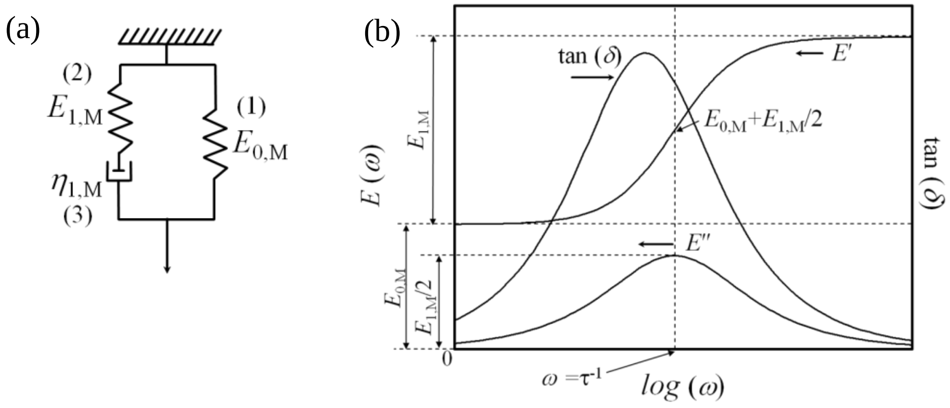

Figure 2.5 (a) A Maxwell unit is attached in parallel to a spring element. (b) Schematic plots of the storage, $E'(\omega)$, loss moduli, $E''(\omega)$ and tan (δ) as a function of angular frequency.

The behavior of the dynamic moduli on angular frequency is akin to that of the dynamic strains plotted in Fig. 2.4. The main difference is that unlike the storage strain, the storage modulus, $E'(\omega)$, increases with increasing angular frequency. However, physical interpretation can be made in the same manner as given for the standard anelastic solid: At high strain frequency, a material behaves like a rigid solid, stress of which is supported by both spring elements (1) and (2), resulting in large storage modulus ($E_{0,\mathrm{M}}$+$E_{1,\mathrm{M}}$) whereas the rigidity decreases with frequency because of the increasing time for a material to flow until the stress in a spring (2) is completely relaxed, leading to the decrease in storage modulus up to $E_{0,\mathrm{M}}$ in the low frequency limit. Since $E'(\omega)$ increases as a function of ω, and $E''(\omega)$ shows a peak at $1/\tau$, plotted in Fig.2.5 (b), their ratio, tan (δ) = $E''(\omega)/E'(\omega)$ shows a peak at $\omega = \frac{1}{\tau}\sqrt{\frac{E_{0,M}}{E_{0,M}+E_{1,M}}} < 1/\tau$, with a height of $\frac{1}{2}\frac{E_{1,M}}{\sqrt{E_{0,M}(E_{0,M}+E_{1,M})}}$.

2.2 MICROSCOPIC PROCESSES RELAVANT TO DEFORMATION OF METALLIC GLASSES

Permanent strain of a solid is accommodated by microscopic defects. In a metallic glass, while shear bands accommodate large plastic strain within narrow region by progressive atomic disordering at high stress, leading to inhomogeneous flow,[12–14] local atomic clusters in which atoms rearrange are believed to accommodate macroscopic strain in the low stress regime.[12,13,15,16] These atomic clusters are termed shear transformation zones (STZs). Because of the inherent disordered structure of metallic glasses, the characterization of STZs has been an extreme challenge, and has been successful only in physical analogues, bubble rafts and colloids.[16,17] However, observations in these analogues have provided important properties of STZs.

Experimental observations of physical analogues have shown that the local regions in which microscopic strain develops consist of originally equiaxed clusters of atoms.[16,17] When an external stress is applied, the clusters undergo thermally-activated strain, resulting in a shear transformation into ellipsoidal shapes.

The properties of STZs reported in physical analogues allow for detailed quantitative description of the deformation of metallic glasses. Transition-state theory has been adopted to yield expressions for flow in terms of thermally activated shear transformations.[12,13] The flow equations consist of physically measurable parameters, which are useful in physical interpretation of experimental data. The constitutive equations have been developed by employing the Eshelby inclusion theory,[16,18] based on detailed observations of local STZ strains in physical analogues.[16]

In this section, deformation mechanisms of metallic glasses are expressed in terms of STZ properties. Governing kinetic equations are used to quantitatively express the macroscopic strain response. Next, the free volume theory[1,12] that has been used to describe structural relaxation is discussed, since relaxation greatly affects atomic transport. Finally, experimental studies on anelasticity of metallic glasses carried out by Argon and Kuo,[2] in which the spectrum of the activation free energies has been determined, are reviewed.

2.2.1 SHEAR TRANSFORMATION ZONES

A schematic illustration of an STZ is shown in Fig. 2.6 (a). It is based on Argon's two-dimensional bubble rafts experiments,[13,16] later confirmed by three-dimensional colloidal experiments as well.[17] The figure shows, in an amorphous structure, a local equiaxed cluster of volume Ω undergoing irreversible shear strain, γ_0^T, in response to an external shear stress, σ_s.

The dashed circle shows a projection of an equiaxed cluster, and the dark solid ellipse shows a projection of the STZ, i.e., the transformed cluster.

The activation energy barrier for the microscopic event of an STZ is illustrated in Fig. 2.6 (b) as a function of the local shear strain coordinate, γ. In the absence of an external shear stress, shear transformation can occur in random directions by thermal fluctuations, the rate of which is determined by the height of activation energy barrier, ΔE_a, discussed below, and the temperature.[12,13] The microscopic events, however, do not produce macroscopic strain, since net number of transformations across the barrier is the same in both forward and backward directions.

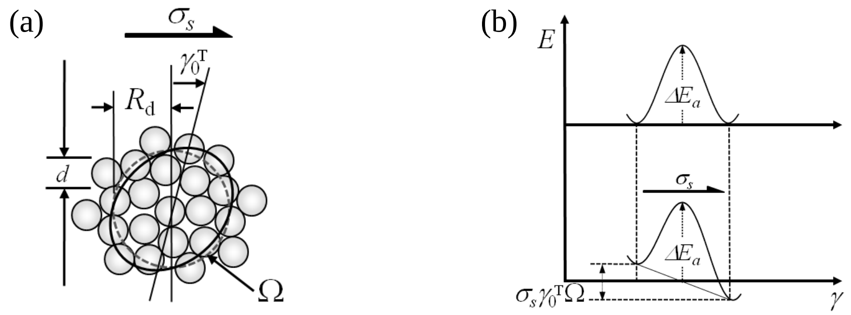

Figure 2.6 (a) Schematic illustration of an STZ undergoing transformation shear strain, γ_0^T, in response to an external shear stress, σ_s. (b) Schematic energy barrier for the activation process of an STZ without (top) and with the application of σ_s (bottom), respectively, as a function of the shear strain, γ.

On the other hand, under an external stress, the activation energy is biased by irreversible work done on the system, $\sigma_s \gamma_0^T \Omega$, resulting in changes in the original barrier height (ΔE_a) by

$\pm(\sigma_s \gamma_0^T \Omega)/2$ for forward and backward directions, respectively: The number of transformations in the direction of shear is greater than that in the backward direction, leading to evolution of macroscopic strain. Assuming Ω to be the same for all STZs, it is now possible to write a quantitative expression for the macroscopic strain rate, $\dot{\gamma}$, according to the transition-state theory:[12,13]

$$\dot{\gamma} = 2c\,\gamma_0^C\,\nu_G \exp\left(-\frac{\Delta E_a}{k_B T}\right)\sinh\left(\frac{\sigma_s \gamma_0^T \Omega}{2k_B T}\right), \tag{2.20}$$

where ν_G is the attempt frequency, which is on the order of Debye frequency, *c* is the volume fraction of *potential* STZs and $\gamma_0^C = \frac{2(4-5\nu)}{15(1-\nu)}\gamma_0^T$ is the irreversible shear strain under constraint by the surrounding matrix, where ν is the Poisson's ratio. At a low shear stress level, the strain rate in Eqn. (2.20) is proportional to σ_s, i.e., the flow is Newtonian.

Argon[13, 19] employed the Eshelby inclusion theory[18] to obtain an expression for the activation energy barrier height for an STZ, ΔE_a. In an Eshelby problem, an inclusion that undergoes transformation strain γ_0^T when unconstrained, also called an eigenstrain,[20] produces elastic energy when constrained by elastic surroundings. The net resulting elastic strain energy is obtained by superposing elastic work that an inclusion experiences during Eshelby procedures: cutting, shearing and welding an inclusion. The activation barrier[13,19] is given by:

$$\Delta E_a = \left[\left(\frac{(7-5\nu)}{30(1-\nu)} + \frac{2(1+\nu)}{9(1-\nu)}\bar{\beta}^2\right)\gamma_0^T + \frac{1}{2}\frac{\bar{\sigma}_{STZ}}{\mu}\right]\mu\,\gamma_0^T\,\Omega, \tag{2.21}$$

where $\bar{\beta}$ is the dilatancy factor, which is the ratio of volume to shear strain: $\bar{\beta} = \varepsilon_0^T/\gamma_0^T$, ε_0^T the volume strain, μ the shear modulus and $\bar{\sigma}_{STZ}$ the shear resistance of an STZ.

The expression for the activation barrier in Eqn. (2.20) consists of three parts: The first term is a shear strain energy produced by the constrained ellipsoidal inclusion that exhibits constrained shear strain, γ_0^C, in the matrix. The second term arises from the temporary dilatation of an STZ that allows for atomic rearrangements, and is the strain energy stored by the dilated inclusion inside and outside the inclusion, i.e. surrounding medium. Experimental observations in bubble rafts have shown that the dilatational normal strain is about equal to the transformation strain, $\bar{\beta} \sim 1$.[19,21] The third term is the strain energy necessary to achieve shear displacement of a hard sphere atom against the approximately sinusoidal shear resistance up to the maximum value, $\bar{\sigma}_{STZ}$. According to Ref. 19, the contribution of this term to Eqn. (2.20) is small compared to the first two parts.

2.2.2 FREE VOLUME AND STRUCTURAL RELAXATION

A metallic glass is a thermodynamically non-equilibrium state. In order to lower its free energy, it undergoes changes in its state toward a metastable equilibrium state spontaneously,[22] involving a series of microscopic structural changes, a process called structural relaxation. It is a distinct phenomenon in amorphous solids, where atomic long-range translational symmetry is lacking. A high cooling rate from the liquid leads to a less-relaxed state of a metallic glass, resulting in more significant subsequent structural relaxation.[23] Structural relaxation involves densification, which can lead to local atomic coordination number changes as well.[24]

In a wide range of experimental studies,[23–26] changes in many properties of metallic glasses have been observed as a result of structural relaxation. While the elastic modulus and electrical resistivity show a few percent changes on annealing, physical properties associated with atomic transport are altered drastically, as manifested by diffusion[24,26] and creep experiments.[22,24,27] In addition, in contrast with crystallization that involves a first order transition, those properties evolve continuously during structural relaxation.[23]

Of central importance in understanding property changes by structural relaxation is the free volume.[1,28] It is defined as the difference between the average atomic volume and that of dense random packing of hard spheres.[29] Its concept was originally introduced by Fox and Flory,[28,30] and a quantitative expression of its distribution, computed by Cohen and Turnbull, has been successful in explaining a molecular transport in metallic liquids.[1] This expression, given in Eqn. (1.1), describes the probability distribution of free volume fluctuations. Cohen and Turnbull used it to express diffusion rates in glasses.[1] This concept was adopted and expanded by Spaepen[12] to express the critical condition for an atomic jump leading to macroscopic deformation. Although the fundamental process is assumed to consist of a single atomic jump in the model,[12] it accounts for many mechanical properties in terms of free volume.[14,22,27] A good example in which we can observe the free volume effects on mechanical properties is the cooling-rate dependence of shear viscosities: with increasing cooling rates, a metallic glass has lower density, i.e., greater free volume, and shows lower shear viscosity.[23]

Structural relaxation, leading to densification, results in a viscosity rise by several orders of magnitudes, which has been attributed to the annihilation of free volume that may allow for an atomic hop.[22,27] While a free-volume criterion by Cohen and Turnbull[1] for atomic diffusion in metallic glasses has been developed and widely used to explain the viscosity rise of metallic glasses,[22,27,31] it has been argued that the criterion based on a series of single atomic hops suffers from a discrepancy between changes in density and in viscosity.[32] On the other hand, Cohen and Turnbull point out that the local free volume necessary for an atomic jump in a metal is the ionic radius, which is much smaller than the atomic radius in Ref. 32. It is crucial to elucidate what permits atomic clusters to undergo microscopic strain, i.e., make it a potential STZ, in order to account for the structural relaxation.

In addition to the role of free volume in structural relaxation, the spectrum of structural relaxation processes observed in calorimetric studies is noted.[26,33] Chen observed changes in the specific heat at constant pressure, ΔC_p, upon the structural relaxation with varying annealing temperature and time. It is endothermic compared to the as-quenched state. Temperatures, T_m, at which peaks of ΔC_p were observed for fixed annealing time, t_a, and the peak amplitudes increase with increasing annealing time and temperature.

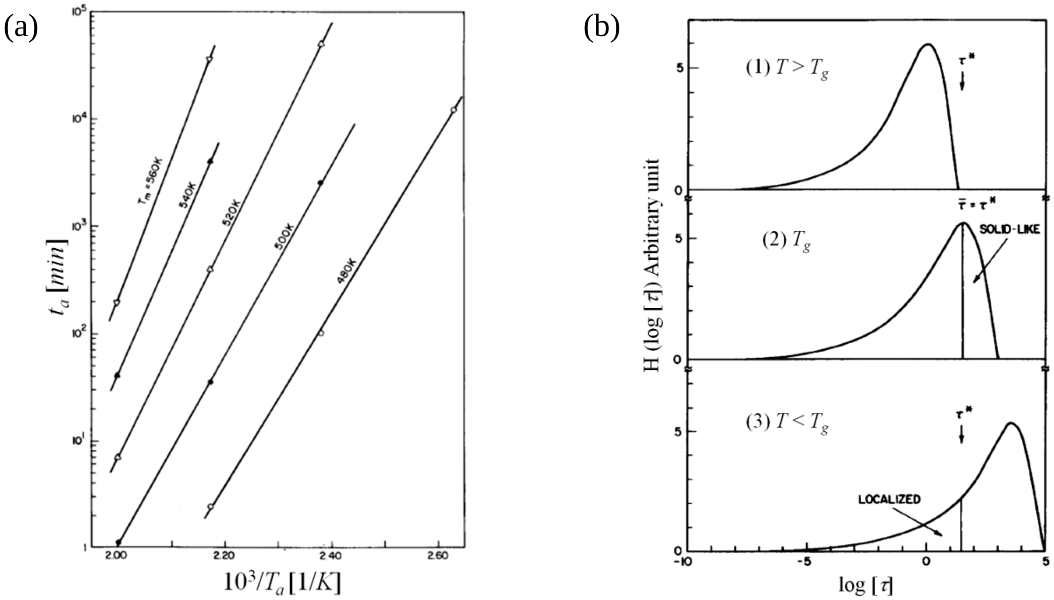

Figure 2.7 (a) Annealing time, t_a, for which the peak of ΔC_p is observed at T_m as a function of reciprocal annealing temperature, $10^3/T_a$. (b) A schematic diagram of the spectrum of relaxation-time constants that has been proposed by Chen in calorimetric studies of a Pd-based metallic glass ($Pd_{48}Ni_{32}P_{20}$) (1) above, (2) at and (3) below the glass transition temperature, T_g.[26,33]

A plot of t_a, for which ΔC_p peaks are observed at T_m, as a function of $10^3/T_a$ at various T_a values is shown in Fig. 2.7 (a). Chen showed an Arrhenius relationship between t_a and $1/T_a$, with different activation energies, ranging from 1 to 2.5 *eV*. He proposed that structural relaxation in metallic glasses involved distributed relaxation processes with distinct Arrhenian dependence on T_a. Figure 2.7 (b) shows a schematic diagram of the spectrum of relaxation-time constants proposed by Chen.[26,33] It was suggested by Chen[26,33] that the atomic groups in which relaxation occurs (termed liquid-like sites) are independently distributed over a wide range of time constants at low temperature, and the spectrum becomes narrower with increasing temperature, leading to an increase in the volume fraction of liquid-like sites. Although physical interpretation of the proposed spectrum was not given in detail, the results suggest distributed properties in metallic glasses, which are discussed in Section 2.2.3.

2.2.3 EXPERIMENTAL STUDIES OF ACTIVATION ENERGY SPECTRA IN METALLIC GLASSES

Several authors proposed that mechanical relaxation of metallic glasses has a wide spectrum of activation energies.[2,23] In fact, theoretical attempts have been made to formulate the kinetics for a system with distributed activation energies, [34] but physically meaningful conclusions can hardly be drawn from the model. However, one of the straightforward experimental results that can provide insights on the spectrum of activation energies has been obtained from dynamic experiments, in which the loss modulus is measured as a function of frequency.[35]

In dynamic experiments, the activation energy for simple Arrhenius behavior can be estimated by performing a series of measurements as a function of angular frequencies, ω, at different temperatures, T.[8] For example, assuming a single time constant for simple Arrhenius behavior, given in Eqn. (2.16), an expression for the time constant, τ, at temperature T is given by:

$$\ln(\tau) = \ln(\tau_0) - \Delta E_a/(kT). \tag{2.22}$$

Since τ is equal to the reciprocal ω_p, at which the loss modulus peak is observed at constant temperature, according to Eqn. (2.19), Eqn. (2.22) allows for estimating the activation energy from a plot of $\tau = 1/\omega_p$ against $1/T$ measured in a series of dynamic measurements performed as a function of ω at different T.

Based on the method explained above, ΔE_a was estimated with a $Zr_{55}Cu_{30}Ni_5Al_{10}$ metallic glass, and experimental results were compared with calculated Debye peaks.[36] While a peak in the loss modulus was observed at ω_p, experimental results showed a much broader spectrum than a Debye peak with asymmetry. The full width at half maximum of the Debye peak for a single activation process on the logarithmic scale, $\Delta\log_{10}(\omega)$, is ~ 1.531, which is slightly greater than 1.5 decades in ω, but that of the loss modulus measured at ~ $420^{o}C$[36] was ~ 3 decades in ω.

It is also important to note experimental studies[37,38] of the loss modulus, measured as a function of T at fixed ω in different metallic glasses, showing a significant low-temperature tail. Figure 2.8 (a) shows the temperature dependence of loss moduli measured at constant frequency of 1 Hz in six different metallic glasses.[37] Loss modulus and temperature were normalized by the apparent peak value (E''_p) and the temperature, at which the peak was observed (T_p), respectively. The loss modulus for every metallic glass showed a low-temperature tail followed by the apparent peak at T_p upon heating. The low-temperature tail in Fig. 2.8 (a) was unexpected according to Eqn. (2.19): when the loss modulus, which is symmetric in T^{-1}, is plotted vs. T, it shows a mild high-temperature tail, because the decrease in T for the unit increase in $\Delta(1/T)$ becomes smaller with increasing T. The experimental observations,[37,38] therefore, suggest that the anelastic relaxation in metallic glasses is not mono-energetic, but involves a range of activation processes.

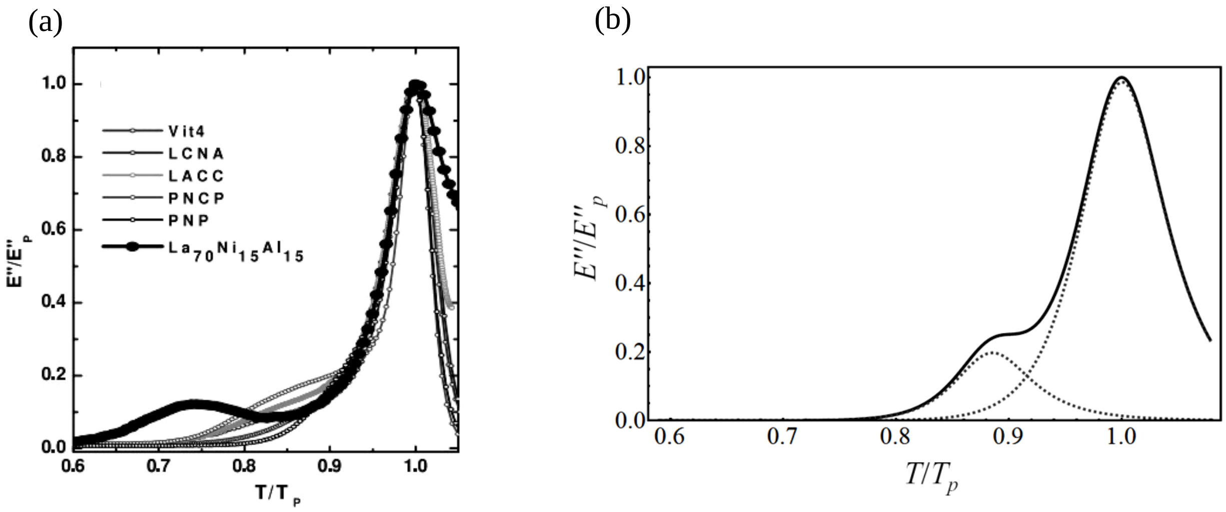

Figure 2.8 (a) Loss moduli (E'') normalized by the apparent peak value (E''_p) measured at constant frequency of 1 *Hz* as a function of temperature, normalized by the peak temperature, T_p, in six different metallic glasses: $Zr_{46.75}Ti_{8.25}Cu_{7.5}Ni_{10}Be_{27.5}$ (Vit4), $La_{57.5}(Cu_{50}Ni_{50})_{25}Al_{17.5}$ (LCNA), $La_{68}Al_{10}Cu_{20}Co_2$ (LACC), $Pd_{40}Ni_{10}Cu_{30}P_{20}$ (PNCP), $Pd_{40}Ni_{40}P_{20}$ (PNP) and $La_{70}Ni_{15}Al_{15}$.[37] (b) Calculated loss modulus spectrum (solid line) using Eqn. (2.13) normalized by E''_p as a function of T/T_p assuming two distinct anelastic processes. Each process is represented by a loss modulus spectrum (dotted lines) with distinct activation energy and amplitude.

For example, assuming that two single-activation processes are involved in dynamic relaxation, the loss modulus is plotted using Eqn. (2.19) in Fig. 2.8 (b). It was assumed that a process with lower activation energy had a lower amplitude than that of the higher activation energy process. Although the plot does not show good agreement with the experimental data in Fig. 2.8 (a), it allows for quantitatively explaining the unexpected asymmetry with low-temperature tail by introducing additional processes in the low activation energy regime, i.e., an activation energy spectrum. The activation energy spectrum in a metallic glass has been viewed as resulting from a continuous distribution of atomic regions of different coordination (structure) or different free volume.[2]

At low external stress levels, isolated STZs form that are embedded in an elastic surrounding medium. While these isolated STZs experience strains in the direction of external shear, producing macroscopic anelastic relaxation strain, they are reversed by elastic back-stress stored in the surrounding matrix upon removal of an external stress, leading to anelastic recovery.[2] Based on calorimetric studies, isolated liquid-like sites in metallic glasses distributed in solid-like matrix at low temperature proposed by Chen[26,33] may have a physically analogous role to that of isolated STZs in anelasticity as suggested by Argon and Kuo.[2] Therefore, anelasticity is the best regime where behavior of isolated STZs can be studied. More recently, Dmowski and his coworkers[39] have performed anelastic measurements and concluded that ~ 25 % of the volume in metallic glasses is occupied by the anelastic sites, employing X-ray diffraction measurements.

In order to experimentally measure the spectrum of activation energies for shear transformations, Argon and Kuo[2] applied torsional shear stress to metallic glass specimens at high temperature for a sufficiently long time, followed by rapid quenching to freeze-in anelastic strain. After removing the external torque, these samples were allowed to relax to recover their original shape isothermally, using temperature steps of ~ 50 *K*.

It was assumed that the relaxation at each temperature was dominated by processes with a small range of activation energies, so that each step, *i*, corresponded approximately to the apparent activation energy: $\Delta E_{a,i}$. Processes corresponding to higher activation energies were assumed frozen at temperature, T_i. Anelastic relaxation at T_i, followed by stepping up the temperature, would allow an anelastic process with higher ΔE_a to dominate the macroscopic strain at higher temperature. Therefore, a series of measurements of anelastic strain at each temperature step was carried out to characterize the anelastic processes distributed on a range of $\Delta E_{a,i}$.[2]

The temperature-stepping method is based on the assumption[2] made by employing a step-function approximation: for a sample with a spectra of time constants for anelastic relaxation, $f(\tau)$, (See Chapter 4), undergoing anelastic relaxation for a duration of t_0, the degree of relaxation for a process with time constant τ changes sharply in a narrow range of time constants around $\tau = t_0$. For example, when anelastic relaxation of a standard linear solid model in a stress-free state, given in Eqn. (2.6), is plotted against $\ln(\tau)$ for a fixed time, t_0, as shown in Fig. 2.9 (a), the strain increases from zero to an equilibrium value, ε_{eq}, near $\tau = t_0$.[8] The temperature stepping method is based on the assumption that the increase in anelastic strain can be approximated by a step function, i.e., $\exp[-t_0/\tau] \cong \begin{cases} 0, & (\tau < t_0) \\ 1, & (\tau > t_0) \end{cases}$: an expression for anelastic strain with the relaxation-time spectrum (See Chapter 3) is given by:[8]

$$\varepsilon_{an}(t) = \int_{-\infty}^{\infty} f(\tau)\exp[-t/\tau]\,d\ln\tau \approx \int_{\ln(\tau=t_0)}^{\infty} f(\tau)\,d\ln\tau\,. \tag{2.23}$$

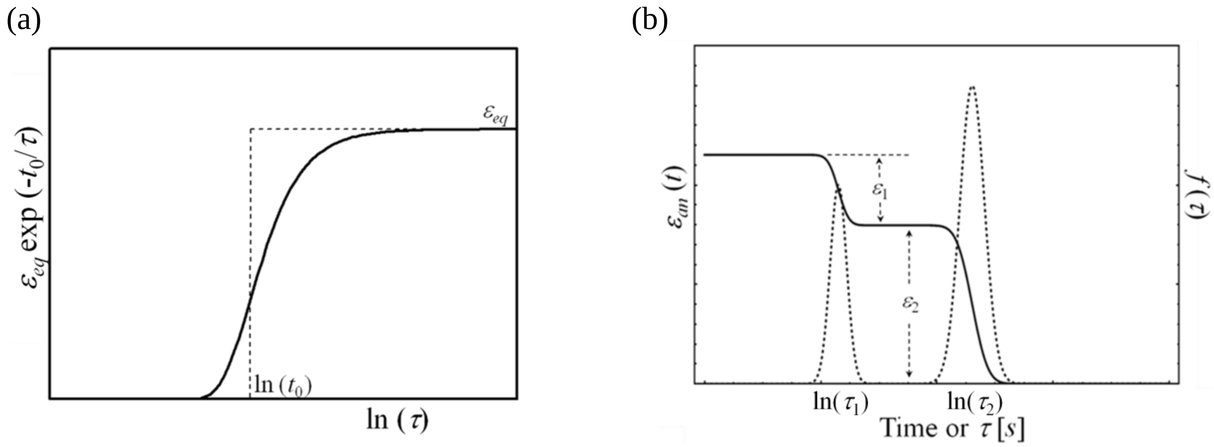

Figure 2.9 (a) Anelastic strain relaxation (solid line) given in Eqn. (2.6) against $\ln(\tau)$ at a fixed time, t_0, for a solid with a range of time constants, τ. A step-function at $t_0 = \tau$ is shown on logarithmic scale (dotted line). (b) Anelastic strain, $\varepsilon_{an}(t)$, (solid line) calculated using Eqn. (2.23) for $f(\tau)$ that includes two distinct processes (dotted line).

For the case of two distinct processes, represented by τ_i, where $i = 1$ and 2, the anelastic strain, $\varepsilon_{an}(t)$, calculated using Eqn. (2.23), is plotted on logarithmic scale in Fig. 2.9 (b). The corresponding $f(\tau)$ is shown with dotted line. In the step-function approximation to the anelastic strain, significant change in $\varepsilon_{an}(t)$ due to a particular process occurs only around the time, $t = \tau_i$, $i = 1, 2$.

By neglecting all but the dominant process, an approximate activation energy spectrum[2] may be obtained from experimental data. For an anelastic solid undergoing several distinct relaxation processes, $\varepsilon_{an}(t)$ is obtained at temperature T_i for duration of time, t, until its relative change is negligible, and can be attributed to a particular relaxation process, represented by $\Delta E_{a,i}$.

According to Argon and Kuo,[2] $\Delta E_{a,i}$ is written in terms of T_i and t: $\Delta E_{a,i} = kT_i \ln(2\tau_0^{-1}t)$. τ_0 is the pre-exponential factor in Eqn. (2.16) and $t \cong \tau_i / 2$, during which significant change in $\varepsilon_{an}(t)$ is experimentally observed. Once the change in $\varepsilon_{an}(t)$ is negligible at T_i, the temperature is increased to a higher value, T_{i+1}, to measure the change in $\varepsilon_{an}(t)$, presumably undergone due to a particular relaxation process with higher activation energy, $\Delta E_{a,i+1}$. Since τ_{i+1} is larger than the measurement time at T_i, the contribution of process $(i + 1)$ at T_i is neglected. The anelastic strain dominated by a process i, ε_i, is proportional to the area of respective peak in $f(\tau)$, therefore, a series of measurements of the changes in $\varepsilon_{an}(t)$ with stepping temperature, T_i, allows for experimentally estimating the volume fraction of potential STZs (See Chapter 4), c_i, for a corresponding $\Delta E_{a,i}$ interval.

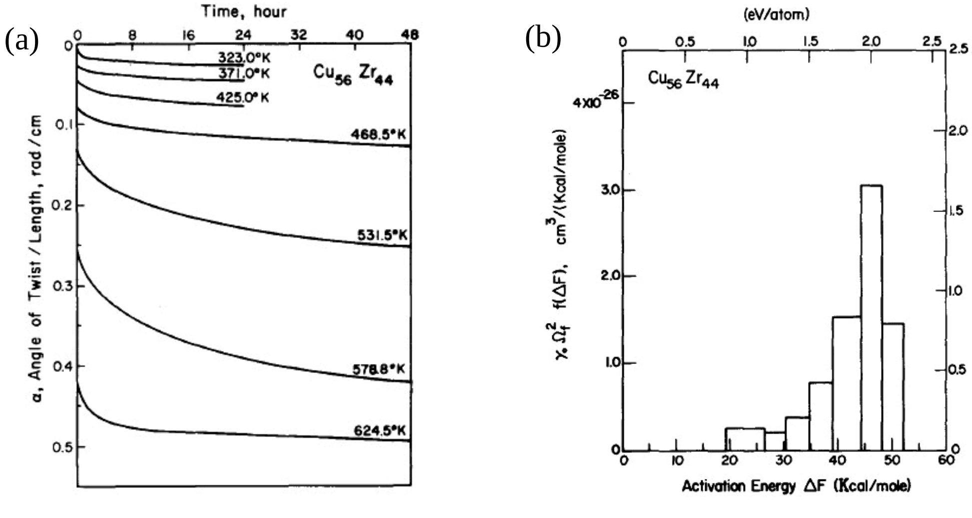

Figure 2.10 (a) Anelastic strain recovery of a crept $Cu_{56}Zr_{44}$ metallic glass specimen followed by quenching and subsequent temperature stepping and (b) histogram of activation energies obtained from the strain recovery, showing the activation energy spectrum.[2]

Based on the previously-described assumption, anelastic strain recovery at each temperature was recorded as a function of time,[2] providing the spectrum of activation energies. Figure 2.10 (a) and (b) shows the anelastic strain recovery recorded with increasing temperature, and the histograms of activation energy spectrum, respectively, in a Cu-rich metallic glass ($Cu_{56}Zr_{44}$).[2]

The height of the activation energy spectrum shown in Fig. 2.10 (b) was determined from the increments of strain recovery observed at each temperature step. The corresponding activation energy for the anelastic recovery process was measured by monitoring strain rate changes as a result of the temperature steps using an approximate Arrhenius relationship, $\Delta E_a = -k\frac{\partial \ln \dot{\gamma}}{\partial (1/T)}$, since the parameter ($\tau_0$) in $\Delta E_{a,i} = kT_i \ln(2\tau_0^{-1}t)$ was not known. Although relative variations in spectrum heights for the activation energies have been observed in five different metallic glasses, their distributions yielded similar shapes in this study.[2] Argon and his coworkers[2,5,13,21,40] argued that the activation energy spectrum reflects the distribution of free volume, with an inverse mapping relationship: local sites with large free volume have small activation energy, and therefore they undergo shear transformations more easily compared to those with smaller free volume.

The observations of distributed anelastic relaxation processes of Ref. 2 made pioneering contributions to the understanding of activation energy spectrum and distributed relaxation-time constants.[41] While the temperature-stepping method[2] has limitations, the results clearly show that anelastic relaxation involves several processes rather than a mono-energetic process. The limitations of the temperature stepping method[2] include resolution limit due to time required to stabilize the temperature for each step. In addition, the assumptions used may result in artifacts.

For example, a step-like relaxation behavior within a narrow activation energy interval is a reasonable estimation method to probe the equilibrium value for a single process. When several activation processes are involved, however, the processes that are assumed to make negligible contribution to the experimentally measured process do contribute to the overall strain, resulting in over- or underestimation of strain, depending on the duration of measurements (See Chapter 6).

2.3 REFERENCES

2.1 M. H. Cohen and D. Turnbull, *J. Chem. Phys*. **31**, 1164 (1959).
2.2 A. S. Argon and H. Y. Kuo, *J. Non-Crys. Sol.* **37**, 241 (1980).
2.3 W. Flügge, Viscoelasticity, *Springer-Verlag*, (1975).
2.4 W. N. Findley and F. A. Davis, *Creep and relaxation of nonlinear viscoelastic materials, with an introduction to linear viscoelasticity*, North-Holland Publishing Company, (1976).
2.5 A. S. Argon and H. Y. Kuo, *J. Non-Crys. Sol.* **37**, 241 (1980).
2.6 A. I Taub and F. Spaepen, *J. Mater. Sci.* **16**, 3087 (1981).
2.7 J. Haimovich and T. Egami, *Mater. Sci. Eng.* **61**, 89 (1983).
2.8 A. S. Nowick and B. S. Berry, *Anelastic relaxation in crystalline solids*, Academic Press, (1972).
2.9 C. Zener, *Elasticity and anelasticity of metals*, University of Chicago Press, Chicago (1948).
2.10 J. D. Ju, D. Jang, A. Nwankpa and M. Atzmon, *J. Appl. Phys.* **109**, 053522 (2011).
2.11 D-H. Choi, W. D. Nix, *Acta Mater*. **54**, 679 (2006).
2.12 F. Spaepen, *Acta Metall*. **25**, 407 (1977).
2.13 A. S. Argon, *Acta Metall*. **27**, 47 (1979).
2.14 P. S. Steif, F. Spaepen and J. W. Hutchinson, *Acta Metall*. **30**, 447 (1982).
2.15 F. Spaepen, *J. Non-Crys. Sol.* **31**, 207 (1978).
2.16 A. S. Argon and H. Y. Kuo, *Mater. Sci. Eng.* **39**, 101 (1979).
2.17 P. Schall, D. Weitz, F. Spaepen, *Science* **318**, 1895 (2007).
2.18 J. D. Eshelby, *Proc. R. Soc.* ***A*241**, 376 (1957).
2.19 A. S. Argon and L. T. Shi, *Acta Metall*. **4**, 499 (1983).
2.20 T. Mura, *Micromechanics of defects in solids*, Springer, (1987).
2.21 A. S. Argon, *J. Phys. Chem. Solids* **10**, 945 (1982).
2.22 S. S. Tsao and F. Spaepen, *Acta Metall*. **33**, 881 (1985).
2.23 H.S. Chen, *Rep. Prog. Phys*. **43**, 353 (1980).
2.24 A. L. Greer and F. Spaepen, *Annals NY Acad. Sci.* **371**, 218 (1981).
2.25 T. Egami, *Annals NY Acad. Sci.* **371**, 238 (1981).
2.26 F. E. Luborsky ed., *Amorphous metallic alloys*, Butterworths, (1983).
2.27 A. I. Taub and F. Spaepen, *Acta Metall*. **28**, 1781(1980).

[2.28] R. W. Cahn and P. Haasen ed., *Physical metallurgy, Ch. 19 by R.W. Cahn and A. L. Greer*, Elsevier (1996).

[2.29] F. Spaepen, *Defect in amorphous metals*, Les Houches Lectures XXXV Amsterdam, North Holland Press, (1981).

[2.30] T. G. Fox and P. J. Flory, *J. Phys. Chem.* **55**, 221 (1951).

[2.31] A. Van den Beukel and S. Radelaar, *Acta Metall*. **31**, 419 (1983).

[2.32] T. Egami, *Prog. Mater. Sci*. **56**, 637 (2011).

[2.33] H. S. Chen, *J. Non-Cryst. Sol*. **46**, 289 (1981).

[2.34] W. Primak, *Phy. Rev*. **100**, 1677 (1955).

[2.35] J. M. Pelletier, *J. Alloys Comp*. **393**, 223 (2005).

[2.36] J. C. Qiao and J. M. Pelletier, *J. Appl. Phys.* **112**, 033518 (2012).

[2.37] Z. Wang, H. B. Yu, P. Wen, H. Y. Bai and W. H. Wang, *J. Phys.*: *Condens. Matter* **23**, 142202 (2011).

[2.38] H. B. Yu, K. Samwer, Y. Wu and W. H. Wang, *Phy. Rev. Lett*. **109**, 095508 (2012).

[2.39] W. Dmowski, T. Iwashita, C.-P. Chuang, J. Almer and T. Egami, *Phys. Rev. Lett.* **105**, 205502 (2010).

[2.40] A. S. Argon and L. T. Shi, *Phil. Mag. A* **46**, 275 (1982).

[2.41] A. I Taub and F. Spaepen, *J. Mater. Sci.* **16**, 3087 (1981).

Chapter 3

EXPERIMENTAL AND COMPUTATIONAL METHODS

The experimental and computational procedures employed to characterize the anelastic properties of our samples is the main theme of this chapter. Beginning with a sample preparation method of an Al-based glass ribbon (composition in *at.* %: $Al_{86.8}Ni_{3.7}Y_{9.5}$) in Section 3.1, mechanical tests: bend-stress relaxation and cantilever bending measurements, employed to measure the anelastic strain of the sample are discussed in Section 3.2 and 3.3, respectively. In addition, the stress and strain states for the respective measurements are analyzed. The tests have been carried out with both as-quenched and relaxed samples.

Experimental details on annealing heat treatment to structurally relax the as-quenched samples are presented in Section 3.4, followed by the procedures for the atomic-scale characterization with a transmission electron microscopy to confirm their amorphous structure in Section 3.5. Finally, in Section 3.6, the computational method, direct spectrum analysis (DSA),[1] employed to obtain the relaxation-time spectra from the experimental data is presented. This methodology is validated by applying it to simulated data, including noise.

3.1 SAMPLE PREPARATION

An $Al_{86.8}Ni_{3.7}Y_{9.5}$ glass ribbon was provided by Dr. F. E. Pinkerton at General Motors R&D Center. The ribbon, 22 *mm* thick and 1 *mm* wide, was obtained by single-wheel melt spinning, using a Cr-coated Cu wheel at a tangential velocity of 40 *m*/*sec.* in vacuum. In this process, the side facing away from the wheel is smoother and shiny. Electron diffraction analyses confirmed the amorphous structure of the sample (See Section 3.5).

3.2 BEND-STRESS RELAXATION

In order to measure anelastic strain over minutes to years, we have employed the bend-stress relaxation experimental technique. The method allows for applying linearly varying strain across a thin ribbon sample in the small-stress regime. By using different radii of curvature, the applied strain is varied. While mechanical analysis of the stress-strain states in a sample for this experiment can be more complicated than that for uniaxial tests, it benefits from far greater long-time stability than instrumented measurements.

The observation of changes in sample curvature was critical in measuring the strain evolution, so caution was exercised when selecting samples prior to the experiment. Five as-quenched and six relaxed 1 *cm* long samples with uniform thickness, 22 μm, and width, 1 *mm*, were cut from a ribbon. They had uniform thickness and initial radius of curvature, without kinks or distortion.

A schematic illustration in Fig. 3.1 (a) shows the experimental setup for imaging a sample. The purpose of this setup is to observe the sample edge-on with a digital camera in a reproducible, consistent, way. It was assumed that the bending axis was parallel to *y*-axis, shown in Fig. 3.2 (a). In order to achieve the goal, it was important to align the sample stage and camera. A tripod-mounted camera was positioned to observe the sample stage first. Assuming that the optical axis of the camera was perpendicular to the camera back surface, both the sample stage and camera were leveled, thus aligning the optical axis of the camera to be perpendicular to the stage. The distance between the camera back surface and sample stage was fixed at ~ 25 *cm*. The approximate center of the sample stage was positioned at the center of the camera screen. Images of a rectangular piece of glass slide, 1 × 3 × 0.04″ (25.4 × 76.2 × 1 *mm*), vertically positioned at different spots on the stage were taken. The intersection of the optical axis with the stage could be determined by finding a spot, where the glass slide was seen edge-on. The sample stage was illuminated with a back light during imaging to observe the sample clearly by minimizing the effects of reflection, shadow and interference of light on the samples.

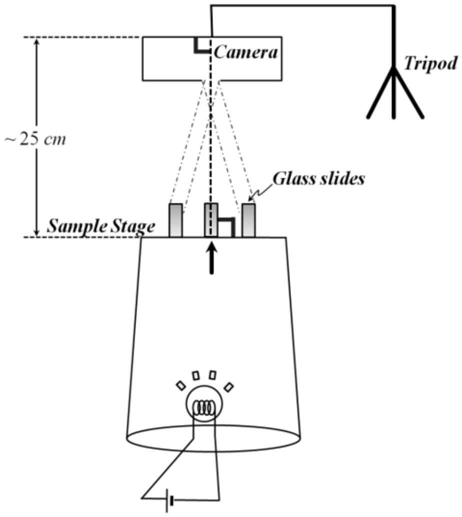

Figure 3.1 Schematic illustration of the experimental setup to image a sample for bend-stress relaxation measurements. The intersection of the optical axis of the camera with the sample stage was determined by finding the spot, where the glass slide was seen edge-on.

Along a line marked around a silicate glass mandrel, samples were constrained, tightly wrapping them with paraffin paper, to ensure plane strain (and stress). Two as-quenched samples were bent with the shiny side up, whereas the other three samples were bent in the opposite direction such that the shiny side is under compression. No effect of bending direction on deformation behavior was observed. Different mandrel radii, ranging from 0.35 to 0.49 *cm*, were used to vary the applied strain. After constraining five as-quenched and six relaxed samples at fixed radius, *R*, for t_c = ~ 2 × 10^6 *sec.*, they were allowed to relax upon removal of the constraint for up to ~ 8 × 10^7 *sec.* in a stress-free state. Two as-quenched samples were constrained for t_c = ~ 4.4 × 10^7 *sec.*, followed by measuring their time-dependent strain in a stress-free state for up to ~ 7 × 10^7 *sec.*

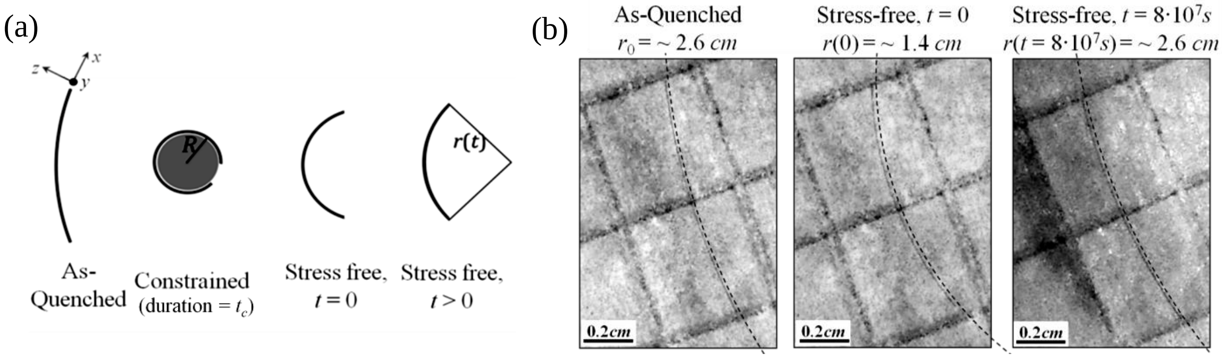

Figure 3.2 (a) Bend-stress relaxation measurement: samples constrained at fixed radius, *R*, were allowed to restore their original shape upon removal of the constraint. The radii of curvature, *r*(*t*), were monitored as a function of time, *t*. (b) Digital photographs of a sample including on-screen visual fitting (dotted line) taken in as-quenched, in a stress-free state at $t = 0$ after constraining the sample for t_c = ~ 2 × 10^6 *sec.*, and that at ~ 8 × 10^7 *sec*. The broken line represents the fit, slightly displaced to allow for sample visibility.

The radii of curvature of samples, *r*(*t*), were monitored as a function of time, *t*. These were determined using a digital camera, as described above, by on-screen visual fitting of the calibrated photographs with a circle. The stages of the bend-stress relaxation experiment are depicted in Fig. 3.2 (a), and digital photographs in Fig. 3.2 (b) show changes in $r(t)$ of a sample during relaxation.

For strain analysis, it is assumed that the cross section of the sample in Fig. 3.2 (a) remains plane and is perpendicular to the longitudinal axis of the sample (x-axis in Fig. 3.2 (a)). In addition, strains in the sample are assumed to be infinitesimal, which allows for the small-strain approximation, resulting in linear strain variation across the sample thickness.[2,3,4,5] It is noted that when a thin metallic sheet is bent to a constant radius of curvature, the plane-strain condition prevails, since the top and bottom surfaces prevent one another from contracting or expanding in the y direction in Fig. 3.2 (a) due to the small thickness.[4] Similarly, when a metallic thin plate is loaded by uniform forces applied at the boundary, it can be assumed that the out-of-plane stress components, σ_{zz}, σ_{xz} and σ_{yz}, are zero on both faces of the plate and within the plate, resulting in only plane-stress components in the stress tensor.[2]

In the following discussion, the expressions for the stress and strain are given for the near-surface region, where they attain their maximum values. The plane-strain components in Cartesian coordinates, illustrated in Fig. 3.1 (a), are obtained under plane-strain boundary conditions:[2,4,5]

$$\begin{aligned} \varepsilon_{xx} &= \kappa \frac{d}{2} \\ \varepsilon_{zz} &= -\frac{\nu}{1-\nu}\varepsilon_{xx} \end{aligned} , \tag{3.1}$$

where $\kappa = 1/r - 1/r(0)$ is the change in radius of curvature of a bent sample, r, relative to that in the initial, stress-free, state, $r(0)$. ε_{xx} is the total axial bending strain, ε_{zz} the out-of-plane strain, d the thickness of a sample and ν is Poisson's ratio of a material. In the small strain regime, linear elasticity theory yields the plane stress components:

$$\begin{aligned} \sigma_{xx} &= \frac{E}{1-\nu^2}\varepsilon_{xx} \\ \sigma_{yy} &= \frac{E\nu}{1-\nu^2}\varepsilon_{xx} \end{aligned}, \tag{3.2}$$

where E is Young's modulus.

Equations (3.1) and (3.2) allow for calculating stress-strain states at a given time in terms of the radius of curvature. For example, when a sample is under constraint at radius R, the total bending strain, ε^T, which consists of elastic and anelastic components, is $\varepsilon_{xx} = \varepsilon^T = \frac{d}{2}\left(\frac{1}{R} - \frac{1}{r_0}\right)$, where r_0 is the initial radius of curvature of the as-quenched sample. At the end of the constraining period, ε^T is expressible by a sum of the elastic strain at mechanical equilibrium, $\varepsilon_0^{el} = \frac{d}{2}\left(\frac{1}{R} - \frac{1}{r(0)}\right)$, and the anelastic strain, $\varepsilon_{an}^0 = \frac{d}{2}\left(\frac{1}{r(0)} - \frac{1}{r_0}\right)$, where $r(t)$ is the radius of curvature at time t after removal of the constraint, i.e., in a stress-free state. Mohr's construction[6,7] allows for the determination of the maximum shear stress, σ_S, and shear strain, γ, by calculating the radius of Mohr's circles from the principal stress and strain components. Mohr's circle is the two-dimensional graphical representation of the state of stress and strain on any oblique plane in a material.[7] Mohr's circles employed to calculate σ_S and γ are plotted in Fig. 3.3 (a) and (b), respectively, yielding the expressions for σ_S and γ: $\sigma_s = \frac{\sigma_{xx} - \sigma_{zz}}{2} = \frac{\sigma_{xx}}{2} = \frac{E}{2(1-\nu^2)}\varepsilon_{xx}$ and $\gamma = \varepsilon_{xx} - \varepsilon_{zz} = \frac{1}{1-\nu}\varepsilon_{xx}$, respectively. Since the shear modulus satisfies: $\mu = \frac{E}{2(1+\nu)}$, σ_S and γ satisfy the shear stress-strain relation, $\sigma_S = \mu\gamma$, of the linear theory.

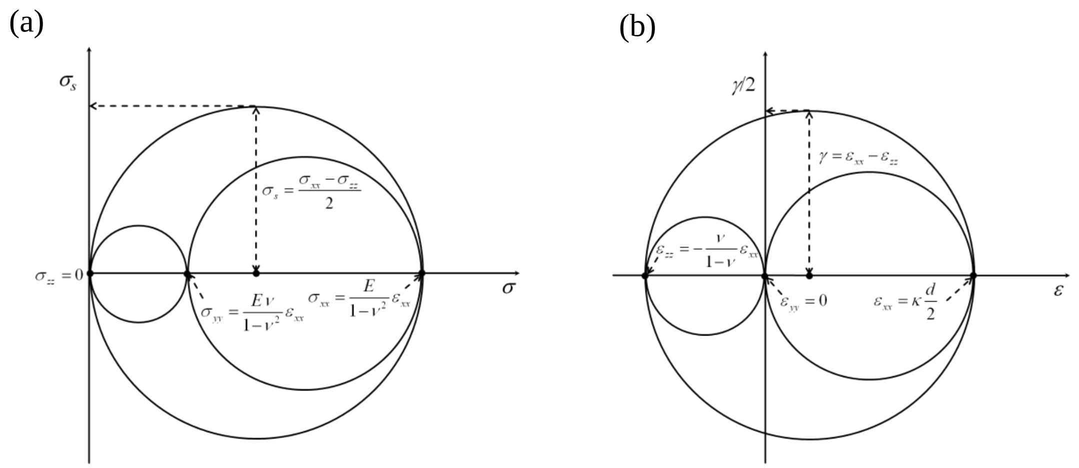

Figure 3.3 Mohr's circles plotted using Eqn. (3.1) and (3.2) to yield expressions for (a) σ_s and (b) γ in a bent thin-ribbon sample.[6,7]

When the stress and strain are linear in each other, both vary linearly across the sample's thickness. In addition, all the stress and strain components, including σ_s and γ explained above, are proportional to the change in curvature under constraint at any point in time. Hence, in a stress-free state, relative change in any strain component due to any linear process is the same, which allow us to evaluate the relation between the anelastic strain and previously applied strain using curvature data. While the bend-stress relaxation method suffers from limitation on strain measurement for short times, it is suitable for measuring the anelastic response for long periods of time due to its long-time stability, from minutes to years. Short-time measurements are discussed in the next section.

3.3 CANTILEVER BENDING

Cantilever bending with a nanoindenter was employed to measure the anelastic strain for short time scale, from sub-millisecond to 200 *sec*. The experiments were carried out by Dr. Dongchan Jang at the California Institute of Technology. An Aligent G200 nanoindenter with a DCM head was used for the experiment. Cantilever samples were mounted in epoxy to clamp one end of samples, and the distance between the clamp and indenter tip contact point, L, was 0.1 *cm*. The displacement, $h(x)$, where x was the distance from the clamp in longitudinal direction, was measured at $x = L$, $h(L) \equiv h_0$, as a function of time, t, at fixed load, P. A schematic illustration of the measurement is given in Fig. 3.4. In order to rule out possible instrumental artifacts, which may arise from deformation of the mounting compound, two different mounting compounds were used, yielding the same result. Thermal drift was subtracted. The stiffness measured from the instantaneous, elastic, displacement agreed with the calculated value,[8] discussed below, based on a Young's modulus value of E_0 = 48.2 *GPa* reported for a similar alloy.[9]

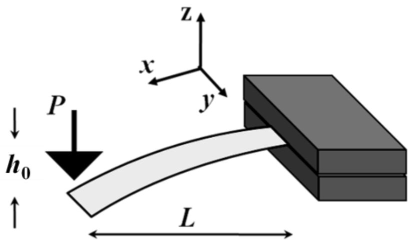

Figure 3.4 A schematic illustration of the cantilever bending measurement: the displacement, $h(x)$, at $x=L$, $h(L) \equiv h_0$, was measured as a function of time, t, at fixed load, P.

In each run, the following cycle was repeated 20 times: a constant load was applied, P = 0.2, 0.02 and 0.002 *mN*, consecutively each for 200 *sec*. Displacement versus time data obtained during each full-load stage were used in the analysis, each consisting of 5000 points at time intervals of 0.04 *sec*. Reversibility of anelastic strain was confirmed during the low-load parts of each cycle. 95 and 70 measurement cycles were obtained with four as-quenched and three relaxed samples, respectively.

The expressions for the stress and strain, given below, are all for the near-surface region, where they attain their maximum values. For a cantilever sample with width and thickness w and d, respectively, an expression for the approximate sample curvature, $\kappa = d^2h/dx^2$, is obtained from the balance between the internal forces and bending moment, $M_y(x)$:[3,4,10]

$$\frac{d^2h}{dx^2} = \frac{M_y(x)}{E_p\, I_{yy}}, \tag{3.3}$$

where I_{yy} is the second area moment of inertia about y axis, and $E_p = \frac{E}{(1-\nu^2)}$. The product of I_{yy} and E_p is often called bending rigidity.[4] An expression for the second area moment of inertia, $I_{yy} = \int_A y^2\, dA$, where A is the cross-sectional area, yields $I_{yy} = \frac{w d^3}{12}$ for a given geometry of a sample, where w and d are the sample width and thickness, respectively. Eqn. (3.3) can be rewritten in terms of the applied load, P:[10]

$$\frac{d^2h}{dx^2} = \frac{P(L-x)}{E_p\, I_{yy}}. \tag{3.4}$$

An expression for h_0, the deflection at $x = L$, when P is applied at L, is obtained by integrating Eqn. (3.4), yielding:

$$h_0 = \frac{P L^3}{3 E_p I_{yy}} = \frac{4 P L^3 (1-\nu^2)}{E w d^3}. \tag{3.5}$$

Young's modulus, as determined from Eqn. (3.5), for the average measured stiffness value, P/h_0 = 146.55 *N*/*m*, agreed with that reported in literature:[8,9] $E = \frac{4 L^3 (1-\nu^2)}{w t^3} \frac{P}{h_0}$ $= \frac{4 \times (10^{-3} m)^3 \times (1-0.35^2)}{10^{-3} m \times (22 \times 10^{-6} m)^3} \times (146.55\, N/m) = 48.3 \times 10^9\, N/m^2 \cdot$

Since the relation between h_0 and P is known, the stress and strain components in a cantilever bending sample are obtained. For example, the total axial bending stress given in Eqn. (3.2) is rewritten in terms of the approximate sample curvature, d^2h/dx^2:

$$\sigma_{xx} = \frac{E}{1-\nu^2} \frac{d}{2} \frac{d^2 h}{dx^2}. \tag{3.6}$$

Substituting Eqn. (3.3) for d^2h/dx^2, one obtains:

$$\sigma_{xx} = \frac{d}{2} \frac{M_y(x)}{I_{yy}} = \frac{6 L P}{w d^2}. \tag{3.7}$$

The load, *P*, in Eqn. (3.7) is replaced by Eqn. (3.5) to obtain expressions for axial bending stress and strain near the clamp ($x = 0$) in terms of the sample thickness, length and deflection, yielding:

$$\sigma_{xx} = \frac{3}{2} \frac{d \cdot h_0}{L^2} \frac{E}{(1-\nu^2)} \text{ and } \varepsilon_{xx} = \frac{3}{2} \frac{d \cdot h_0}{L^2}, \tag{3.8}$$

respectively, which are proportional to h_0. For the load values used, the elastic strain, ε_0^{el}, was kept constant at less than 10^{-4} for all measurements, as determined from the instantaneous deflection in response to a jump in load using Eqn. (3.8).

As for bend-stress relaxation measurements, all the stress and strain components in the cantilever bending sample are linear in the axial bending strain component. The linearity allows for analyzing the data obtained in cantilever bending measurements in terms of h_0, since its relative changes due to any linear process are the same as that for the uniaxial test: below the yield point, all the shear stress/strain components are proportional to the principal stress/strain components, which are proportional to the deflection and uniaxial strain for cantilever bending and uniaxial tests, respectively. Therefore, the time-dependent anelastic strain, normalized by ε_0^{el}, is equal to the ratio of the corresponding displacements, $h_0(t)/h_{0,el}$, where $h_0(t)$ and $h_{0,el}$ are the time-dependent displacement and elastic displacement, respectively. These relationships are not dependent on knowledge of the sample dimensions, and thus do not suffer from uncertainties in them.

3.4 ANNEALING HEAT TREATMENT

In order to measure the effect of structural relaxation on the anelastic properties of the samples, annealing heat treatment was carried out with six as-quenched samples prior to the mechanical tests. Caution was exercised to eliminate the potential artifacts due to heat treatment, such as crystallization, oxidation or temperature drop/overshoot. We used a Ti-gettered, flowing Ar, furnace to structurally relax samples at $110^{o}C$ for 1 *hr.*, a condition that does not lead to crystallization.[11] Before annealing, the atmosphere in the furnace was purged with gettered Ar for one day to minimize oxidation. Samples were placed in the room temperature zone in the furnace for 30 *min.* to stabilize the temperature, followed by placing them in the high temperature zone using a magnetic feed-through. The maximum temperature fluctuation was $110 \pm 2.5\ ^{o}C$ within the duration of 3 *min.* at the early stage of annealing. After the heat treatment for 1 *hr.*, samples were cooled at room temperature, $295 \pm 1\ K$.

3.5 STRUCTURAL CHARACTERIZATION

The microstructure of both as-quenched and relaxed samples was observed using a JEOL 2011 high-resolution transmission electron microscope to verify their amorphous structure. Samples, 1 *mm* × 1 *mm*, were prepared using a single-side jet thinning electro-polisher at 243 *K*, until a perforation formed. The jet thinning electrolyte consisted of 25 % nitric acid and 75 % methanol, and the applied voltage and current density were 15 *V* and 7 $m\text{A}/mm^2$, respectively. Mechanical polishing and ion milling were not employed to avoid potential damage to samples. Figure 3.5 is a representative high resolution image of a relaxed $Al_{86.8}Ni_{3.7}Y_{9.5}$ with diffuse electron diffraction pattern included in the inset, showing the amorphous structure.

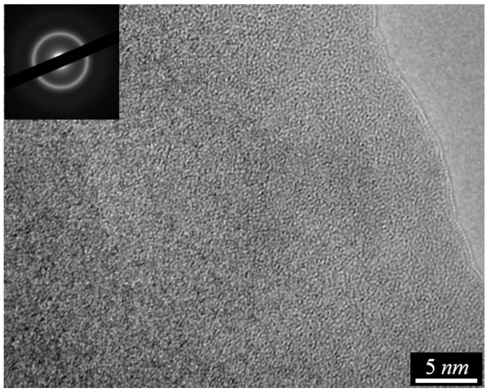

Figure 3.5 High-resolution transmission electron micrograph of a relaxed metallic glass (110°*C* for 60 *min.*) with selected area electron diffraction pattern included in the inset, showing the amorphous structure.

3.6 DIRECT SPECTRUM ANALYSIS (DSA)[1]

One important challenge in analysis of experiments is to obtain a relaxation-time spectrum from time-dependent relaxation in quasi-static data or in dynamic data obtained under cyclic constraints. In particular, the task is difficult due to experimental noise. While experimental studies on anelasticity, using strain recovery measurements with temperature stepping,[12] have allowed for obtaining the approximate activation energy spectra in metallic glasses, challenges in quantitative spectrum determination from strain/time data remain. Experimental results are typically fitted with a linear combination of a few exponents, assuming a certain number of relaxation processes,[13] or, with a single stretched exponent ($\varepsilon(t) = \exp(-t/\tau)^{\beta}$)), thereby making an implicit assumption about the shape of the spectrum.[14] Instead, we employed a direct spectrum analysis method,[15] which allowed us to resolve an unprecedented number of distinct processes. Details on the results are discussed in Chapter 4.

3.6.1 STATIC CASE

For a relaxation-time spectrum, $f(\tau)$, the anelastic strain, $\varepsilon(t)$, is given as a function of time, t, by:

$$\varepsilon(t) = \int_{-\infty}^{\infty} f(\tau)\, g_{\tau}(t)\, d\ln\tau\,, \tag{3.9}$$

where $g_{\tau}(t)$ is equal to (1-exp[$-t/\tau$]) under a constant stress and exp[$-t/\tau$] in a stress-free state, respectively, τ being the respective time constants for relaxation, discussed in Section 2.2. Assuming that the rate-limiting step of the relaxation process is thermally activated, with an energy barrier, ΔE_a, and therefore, τ is expressible by an Arrhenius relation, given in Eqn. (2.16): $\tau = \tau_0 \exp[\Delta E_a/(kT)]$, where τ_0 is the pre-exponential factor and k is the Boltzmann constant, Eqn. (3.9) can be rewritten as:

$$\varepsilon(t) = \int_{-\infty}^{\infty} a(\Delta E_a)\, b(kT\ln(t\,\tau_0^{-1}) - \Delta E_a)\, d\Delta E_a\,. \tag{3.10}$$

Where $a(\Delta E_a)$ is the activation energy spectrum and $b(x)$ is equal to 1-exp[-exp[$x/(kT)$]]: $b(kT\ln(t\tau_0^{-1})-\Delta E_a)$ in Eqn (3.10) under constant stress is equal to (1-exp[$-t$ exp[$-\Delta E_a/(kT)$]/τ_0]) = $g_\tau(t)$ = (1-exp[$-t/\tau$]). Equation (3.10) allows for employing the convolution theorem by Fourier or Laplace transformation to obtain the activation energy spectrum, which has yielded consistent results without prior assumptions (See, e.g., Ref. 16).

The DSA method involves a least-squares fit to the data. Eqn. (3.9), substituting summation for integration, was employed, taking the boundary conditions into account. For example, we used the following expressions for quasi-static measurements to approximate Eqn. (3.9):

$$\varepsilon(t)/\varepsilon_{el}^0 = A + Bt + \sum_{i=1}^{N_1} \varepsilon_i\,(1-\exp[t/\tau_i]), \tag{3.11.a}$$

$$\varepsilon(t)/\varepsilon_{el}^0 = A + \sum_{i=1}^{N_2} \varepsilon_i \exp[t/\tau_i], \tag{3.11.b}$$

for the cantilever and bend-stress relaxation measurements, respectively. The τ_i are fixed and spaced logarithmically:

$$\tau_i = \tau_{\min} \exp[(i-1)\Delta \ln \tau],\ i = 1,\ldots,N, \tag{3.12}$$

where N is the number of variables in Eqn. (3.11), $\Delta \ln \tau = \ln[\tau_{\max}/\tau_{\min}]/(N-1)$, τ_{min} and τ_{max} are the minimum and maximum τ_i values, respectively. The linear term ($B\ t$) in Eqn. (3.11.a) describes plastic flow or approximates anelastic processes with time constants greater than the measurement duration. A in Eqn. (3.11) is typically very small and possibly includes processes with time constants longer than the duration of the experiment: anelastic strain stored in a material recovers on a longer time scale than that of the experiment (See Chapter 4). The amplitudes of the exponents, ε_i, *A* and *B* are fitting parameters, which are allowed to vary. Initial guesses for all fitting parameters were set as 10^{-2}. Other choices yielded the same results.

The higher the number of τ_i values that can be used, the higher the fit quality. However, this number cannot exceed the number of data points, since the problem would then be overdetermined. The range of τ_i was chosen to extend beyond the experimental time range, with its upper limit, τ_{max}, being twice that of the maximum measurement duration in the data. This range was arrived at after tests with simulated data, detailed below. τ_{min}, however, was consistently set as 0.3*sec.*/0.3*hr.* for cantilever/bend-stress relaxation data, respectively, due to the limited resolution of the experimental data below τ_{min}, i.e., small number of data points. Finally, the amplitudes of relaxation-time spectrum corresponding to τ_i, $f(\tau_i)$, are given by:

$$f(\tau_i) = \varepsilon_i / \Delta \ln \tau \, . \tag{3.13}$$

In order to assess the reliability of the DSA method, we performed tests with simulated data for anelastic properties in quasi-static and dynamic measurements. First, a spectrum consisting of a superposition of several Dirac delta functions was used, representing a series of three Voigt units with arbitrarily chosen discrete time constants, τ_i, and the amplitudes, ε_i (i = 1, 2 and 3), the corresponding anelastic strain under constant stress following mechanical constraint was calculated as, $\varepsilon_{an}(t) = 0.008\,(1-\exp[-t/2]) + 0.01(1-\exp[-t/12]) + 0.015\,(1-\exp[-t/80])$, from 0 to 200 *sec*. at 0.04 *sec*. intervals. Normally-distributed random noise with standard deviation, $\sigma_{stdev} = 3 \times 10^{-4}$, was added. The assumed spectrum and resulting simulated anelastic strain as a function of time are shown in Fig. 3.6 with a histogram and black dots, respectively. The simulated data set was then fitted using Mathematica© with six fitting parameters, τ_i and ε_i (i = 1, 2 and 3), using the following expression of $\varepsilon_{an}(t)$ for a series of three Voigt units:

$$\varepsilon_{an}(t) = \sum_{i=1}^{3} \varepsilon_i \,(1 - \exp[-t/\tau_i]) \,. \tag{3.14}$$

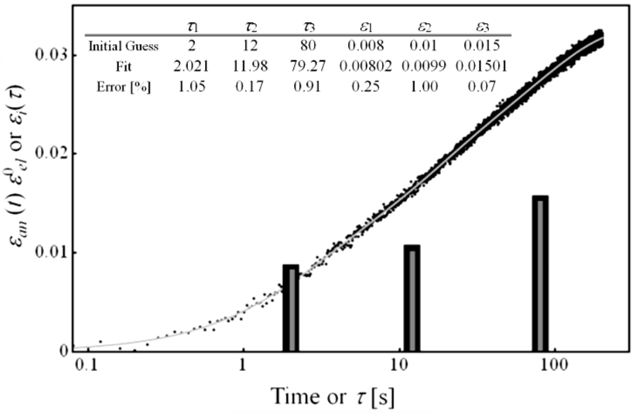

	τ_1	τ_2	τ_3	ε_1	ε_2	ε_3
Initial Guess	2	12	80	0.008	0.01	0.015
Fit	2.021	11.98	79.27	0.00802	0.0099	0.01501
Error [%]	1.05	0.17	0.91	0.25	1.00	0.07

Figure 3.6 Simulated data (black dots) created using Eqn. (3.9), for a series of three Voigt units experiencing anelastic strain under constant stress from 0 to 200 *sec*. at 0.04 *sec*. intervals. Assumed τ_i and ε_i (i = 1, 2 and 3) used to simulate the data are shown in the black histogram. Normally distributed random noise with standard deviation, σ_{stdev} = 3 × 10^{-4}, was added to the simulated data. Six fitting parameters (ε_i and τ_i) obtained using Mathematica© are shown (gray histogram), and the fit (gray line) is superimposed on the simulated data. τ_i and ε_i values are summarized in the inset.

As shown in Fig. 3.6 with gray histogram and summarized in the table in the figure, the fitting parameters were obtained within ± ~ 1.1 % error, yielding a fit (gray line in Fig. 3.6) with good agreement. When a larger number of ε_i, on a range of τ, contribute to the spectrum in the presence of scatter, however, resolving the original spectrum was challenging. Examples of such cases are discussed below.

For assumed spectra that included broader distribution, conventional fitting programs, such as Mathematica© and Origin©, allowed for obtaining the relaxation-time spectrum for simulated data that did not contain noise, but fitting simulated data that included noise, reflecting experimental error, was not successful using these programs. Examples of the test results obtained using Mathematica© are plotted in Fig. 3.7. For these tests, a relaxation-time spectrum, $f(\tau)$, consisting of two log-normal peaks was assumed. From the assumed spectrum, two simulated data sets were created using Eqn. (3.9) from 0 to 200 *sec*. at 0.04 *sec*. intervals, without and with adding small random noise ($\sigma_{stdev} = 10^{-5}$). The noise level was extremely small compared to that introduced below in the simulated data for DSA performed with a nonlinear solver IPOPT.[17,18] The simulated data sets were fitted with a linear combination of 30 exponential functions ($N_1 = 30$) given in Eqn. (3.11.a). τ_{min} and τ_{min} were set as 0.3 and 400 *sec*., respectively, as explained above. Unlike the previous case with a spectrum consisting of delta functions, the τ_i values were fixed here and for all DSA cases. Finally, the relaxation-time spectrum was obtained by DSA using Eqn. (3.13).

The spectrum obtained, using Mathematica©, with $N_1 = 30$ for simulated data without noise, plotted in Fig. 3.7 (a), shows excellent agreement with the originally assumed spectrum. In the presence of small noise in the simulated data, however, the DSA-computed spectrum deviated significantly from the assumed spectrum, in Fig. 3.7 (b). Although several peaks in the spectrum were observed near the original peak positions, finding their positions quantitatively was a challenge due to the limited resolution and number of parameters.

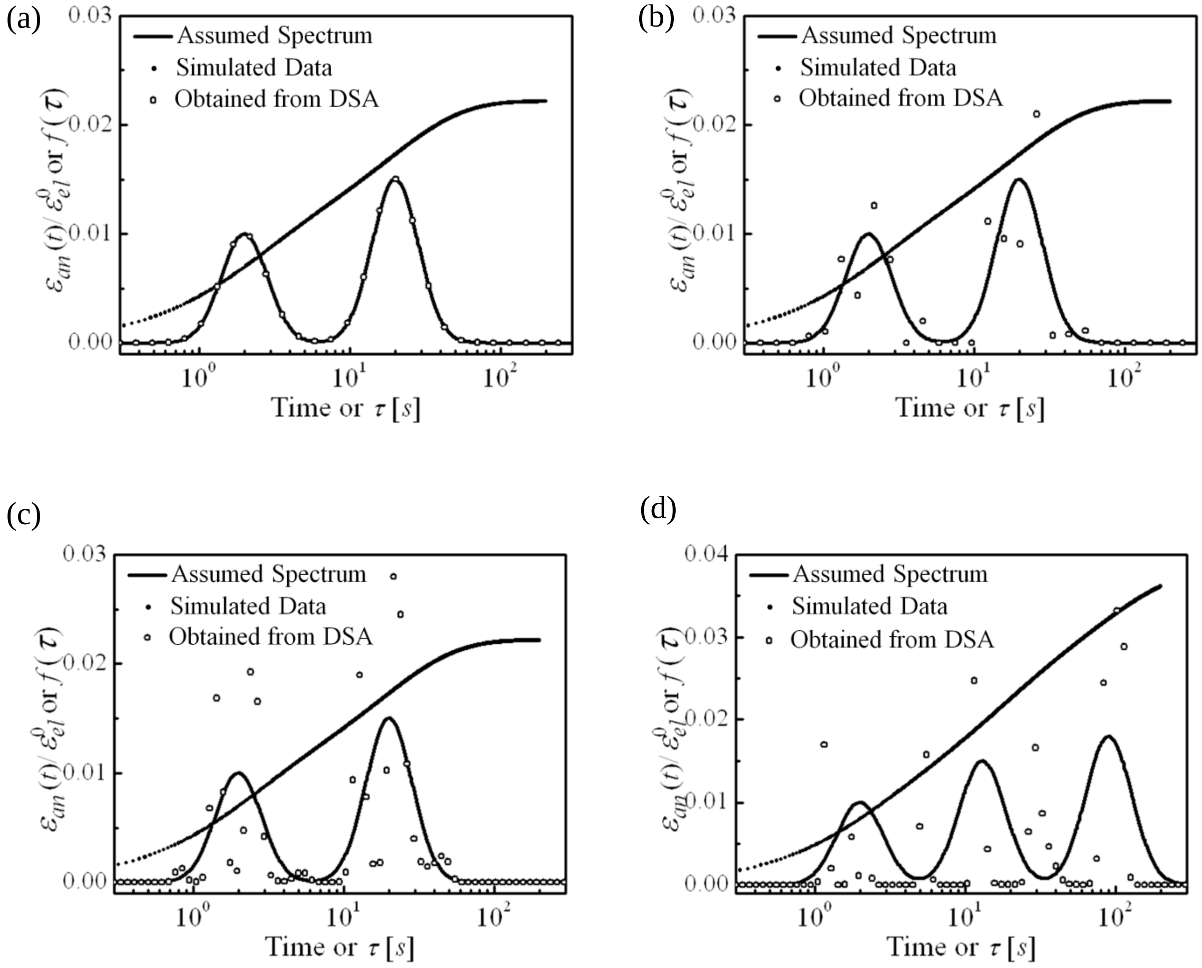

Figure 3.7 DSA tests using Mathematica©. (a) Assumed relaxation-time spectrum with two distinct peaks (solid line). Using the spectrum, a simulated data set (black dots) is created using Eqn. (3.9). The relaxation time-spectrum is recovered from the simulated data by DSA (open circles), using $N_1 = 30$ in Eqn. (3.11) and (3.13). (b) Same as (a), but small random noise ($\sigma_{stdev} = 10^{-5}$) is added. The noise, while too small to be visible in the figure, results in significant deviation of the spectrum obtained by DSA from the original spectrum. (c) Same as (b), with DSA performed with a larger number of parameters ($N_1 = 70$). (d) Same as (c), but with three peaks in the assumed spectrum.

DSA performed with N_1 = 70, also using Mathematica©, employing the same simulated data as in Fig. 3.7 (c), yielded a slightly higher-quality fit, but the results were still insufficient to provide quantitative information on the spectrum. In addition, although many parameters (N_1 = 70) were used, resolving the original spectrum for a larger number of peaks (Fig. 3.7 (d)) was even more challenging, yielding a poorer quality fit, compared to Fig. 3.7 (b) or (c).

In conclusion, in order to obtain the relaxation-time spectrum by DSA, it was crucial to fit the data with many parameters, since spectrum may span a wide range of τ, thereby allowing for higher quality of the fit, and to resolve the noise problems that were observed when using Mathematica©. This required more-powerful software.

DSA was subsequently performed by fitting the experimental data using the Primal-Dual Interior Point Filter Line Search Algorithm, which allows for handling problems with large numbers of inequality constraints.[17] This method has proven to provide superior fits, as compared with Mathematica©, in the presence of noise, as discussed below. The software package AMPL[18] was used with a nonlinear solver IPOPT.[17] In order to assess its reliability, detailed tests using simulated data were also performed.

First, we assume a relaxation-time spectrum consisting of three log-normal peaks, as shown in Fig. 3.8 (a) and (b). This spectrum was selected to resemble DSA results for one of our experiments involving cantilever bending measurements, discussed in Chapter 4. A simulated data set was created for quasi-static measurements under a constant stress using Eqn. (3.9). This data set contained 5000 data points spaced linearly in time, from 0 to 200 *sec*. at 0.04 *sec*. intervals. Normally distributed random noise with standard deviation, $\sigma_{stdev} = 3 \times 10^{-4}$ was added, a value close to that of the experimental data (See Fig. 3 in Chapter 4).

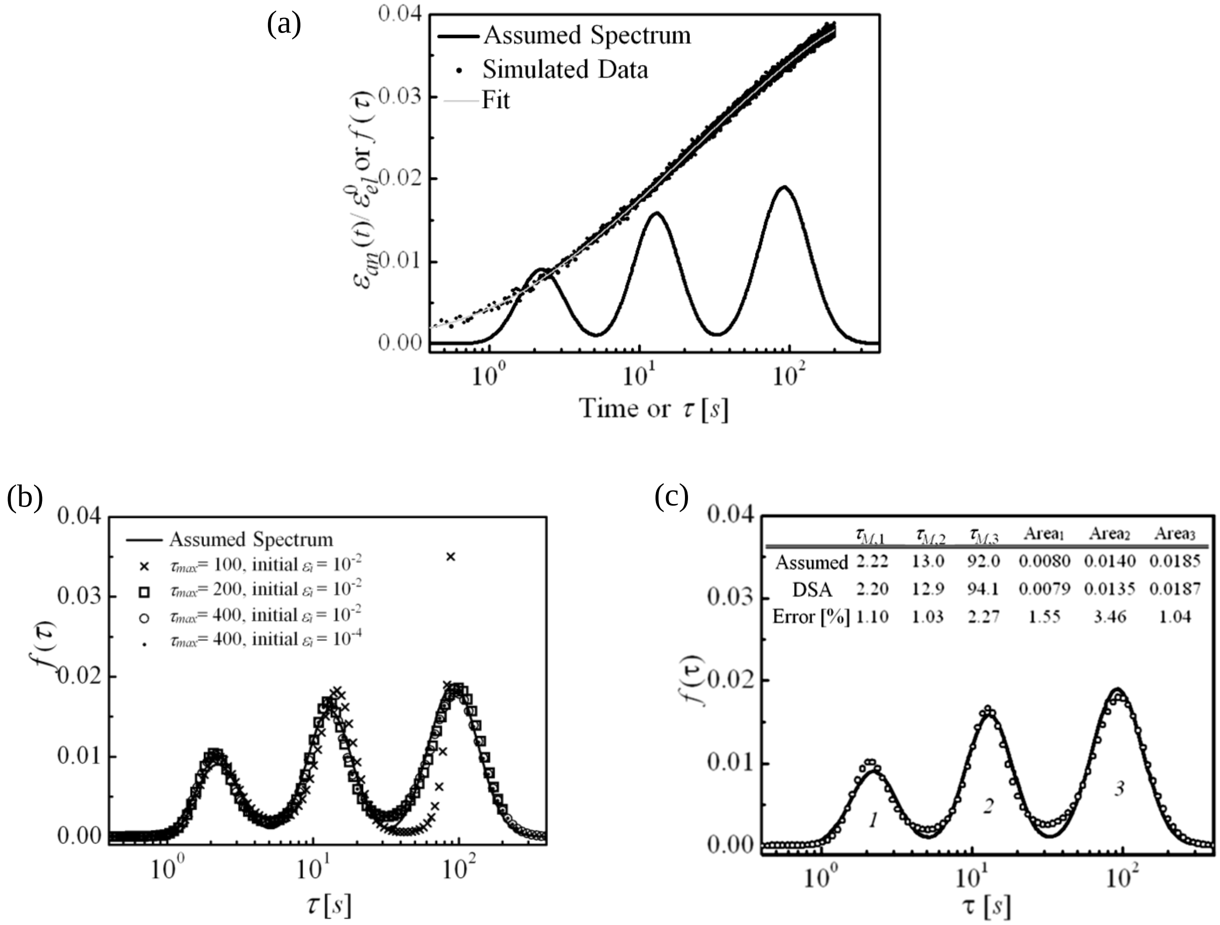

	$\tau_{M,1}$	$\tau_{M,2}$	$\tau_{M,3}$	Area$_1$	Area$_2$	Area$_3$
Assumed	2.22	13.0	92.0	0.0080	0.0140	0.0185
DSA	2.20	12.9	94.1	0.0079	0.0135	0.0187
Error [%]	1.10	1.03	2.27	1.55	3.46	1.04

Figure 3.8 DSA with AMPL. (a) Simulated static data (dots) created based on an assumed relaxation-time spectrum (solid line in (a), (b) and (c)) using Eqn. (3.9), consisting of three log-normal distribution profiles: $0.009\exp\left[-\left(\frac{\ln(\tau/2.22)}{0.5}\right)^2\right] + 0.016\exp\left[-\left(\frac{\ln(\tau/13)}{0.5}\right)^2\right] + 0.019\exp\left[-\left(\frac{\ln(\tau/92)}{0.55}\right)^2\right]$. The data consist of 5000 points spaced linearly in time from 0 to 200 *sec*. at 0.04 *sec*. intervals. A fit to the simulated data, yielding R^2 = 0.99775, is superimposed on the plot. (b) The assumed spectrum (solid line) and the spectrum recovered by DSA with different τ_{max} = 100 (cross symbols, ×), 200 (open squares) and 400 *sec*. with initial $\varepsilon_i = 10^{-2}$ (open circles) and that with initial $\varepsilon_i = 10^{-4}$ (dots). (c) Best fit: The median and area, determined by integration between minima, of the respective peaks, *i*, denoted as $\tau_{M,i}$ and Area$_i$, are summarized in the inset.

Next, the simulated data set was fitted by DSA with a linear combination of 100 exponential functions (N_1 = 100) given in Eqn. (3.11.a). Two different initial ε_i values were tested: 10^{-2} and 10^{-4}. τ_{min} was set as 0.3 *sec.* and different τ_{max} values were tested: 100, 200 and 400 *sec*. Finally, the relaxation-time spectrum was obtained using Eqn. (3.13).

Relaxation-time spectra obtained by DSA with different τ_{max} values are shown in Fig. 3.8 (b). When τ_{max} was smaller than the highest τ value in the simulated data, the peak i = 3 was not fully observed, yielding overly high ε_i in the high τ regime. However, the fit to the spectrum was improved significantly for τ_{max} = 200 *sec.* and 400 *sec.*, recovering all three peaks. Two different initial guesses for all ε_i and A yielded the same DSA results. Although the results were not perfect in the presence of noise in the simulated data, the relaxation-time spectrum obtained reproduced the original spectrum fairly closely. R^2 ≡ 1 - (sum of the squares of the residuals/the total sum of squares) is given by:

$$R^2 \equiv 1 - \left(\sum_{j=1}^{n} (y_j - h(t_j))^2 / \sum_{j=1}^{n} (y_j - \bar{y})^2 \right), \tag{3.15}$$

where y_j is the j^{th} value of the simulated data that consist of n number of data points, $h(t_j)$ is the fit value at the j^{th} t, and $\bar{y}$ is the mean of the data. The best fit showed good agreement with the simulated data, with R^2 = 0.99775 (Fig. 3.8 (a)). The area of each peak in the spectrum obtained by DSA, determined by integration between minima, fell within 3.5 % of the value for the assumed spectrum. The median of the each peak i, $\tau_{M,i}$, the value of which for DSA result was determined by fitting with a sum of log-normal distribution functions, was within < 2.3 % of the assumed value. The results are summarized in the table in Fig. 3.8 (c).

For the results shown in Fig. 3.8, the assumed $\tau_{M,3}$ value, 92 *sec.*, was well below τ_{max}, which may allow for resolving $\tau_{M,3}$ using τ_{max} = 200 *sec.* When τ_{max} is too close to $\tau_{M,3}$, however, DSA is expected to yield the overly high ε_i at high τ to make up for not including the entire peak, as observed for the fit obtained with τ_{max} = 100 *sec*. Therefore, due to the uncertainty of $\tau_{M,i}$ in the experimental data, τ_{max} was set to be twice that of the maximum measurement duration in the data.

The DSA method employed in our analyses of the experimental data yielded detailed relaxation-time spectra, which allowed for probing the distribution of relaxation times. Use of the nonlinear solver IPOPT[17,18] has allowed us to largely overcome the effect of experimental noise on relaxation-time spectrum, obtained by DSA. For the quasi-static experimental data, in order to rule out potential artifacts due to the fitting method, we performed fits with several vales of N_1 and N_2; we also fitted the bend-stress relaxation data with 4-8 exponents, allowing both ε_i and τ_i to vary as well. This yielded results consistent with DSA.

3.6.2 DYNAMIC CASE

In dynamic experiments, with cyclic stress and strain, obtaining relaxation-time spectra is even more challenging. Even a single time constant leads to a broad loss modulus, $E''(\omega)$, given by a Cauchy function. Similar to the expressions for the quasi-static anelastic strain given in Eqn. (3.11), storage and loss moduli for the relaxation-time spectrum given in Eqn. (2.18) and (2.19) can be rewritten as, as approximations of integrals:[1]

$$E'(\omega) = E_0 + \sum_{i=1}^{N_1} E_i \frac{\omega^2 \tau_i^{\,2}}{1+\omega^2 \tau_i^{\,2}}, \tag{3.16.a}$$

$$E''(\omega) = \sum_{i=1}^{N_2} E_i \frac{\omega \tau_i}{1 + \omega^2 \tau_i^2}, \tag{3.16.b}$$

respectively, where the τ_i are fixed, and E_i and E_0 are the fitting parameters for the storage and loss moduli, respectively. N_1 and N_2 need to be sufficiently large to approximate integral expressions. In order to examine whether relaxation-time spectra can be recovered from dynamic data, DSA was performed with simulated loss modulus curves that included noise. The relative noise level used in the simulated data was similar to or exceeded that in the dynamic experimental data, to be employed in our analysis (See Fig. 5.1 in Chapter 5).

DSA performed with simulated loss modulus curves created from an assumed relaxation-time spectrum, consisting of several distinct peaks, resolved the assumed spectrum with good agreement. An example of our tests is shown in Fig. 3.9. The relaxation-time spectrum, $f(\tau)$, was assumed to consist of four distinct peaks in τ (Fig. 3.9 (a)), which was given by:

$$f(\tau) = \sum_{k=1}^{I} A_k \exp\left[-\left(\frac{\ln(\tau/\tau_{M,k})}{C_k}\right)\right], \tag{3.17}$$

where $I = 4$, and A_k, $\tau_{M,k}$ and C_k are given in Table 3.1:

	$k = 1$	$k = 2$	$k = 3$	$k = 4$
A_k	0.01	0.011	0.0115	0.012
$\tau_{M,k}$	2	12	80	450
C_k	0.5	0.5	0.5	0.5

Table 3.1 Assumed values of A_k, $\tau_{M,k}$ and C_k for $f(\tau)$ in Eqn. (3.17) and Fig. 3.9.

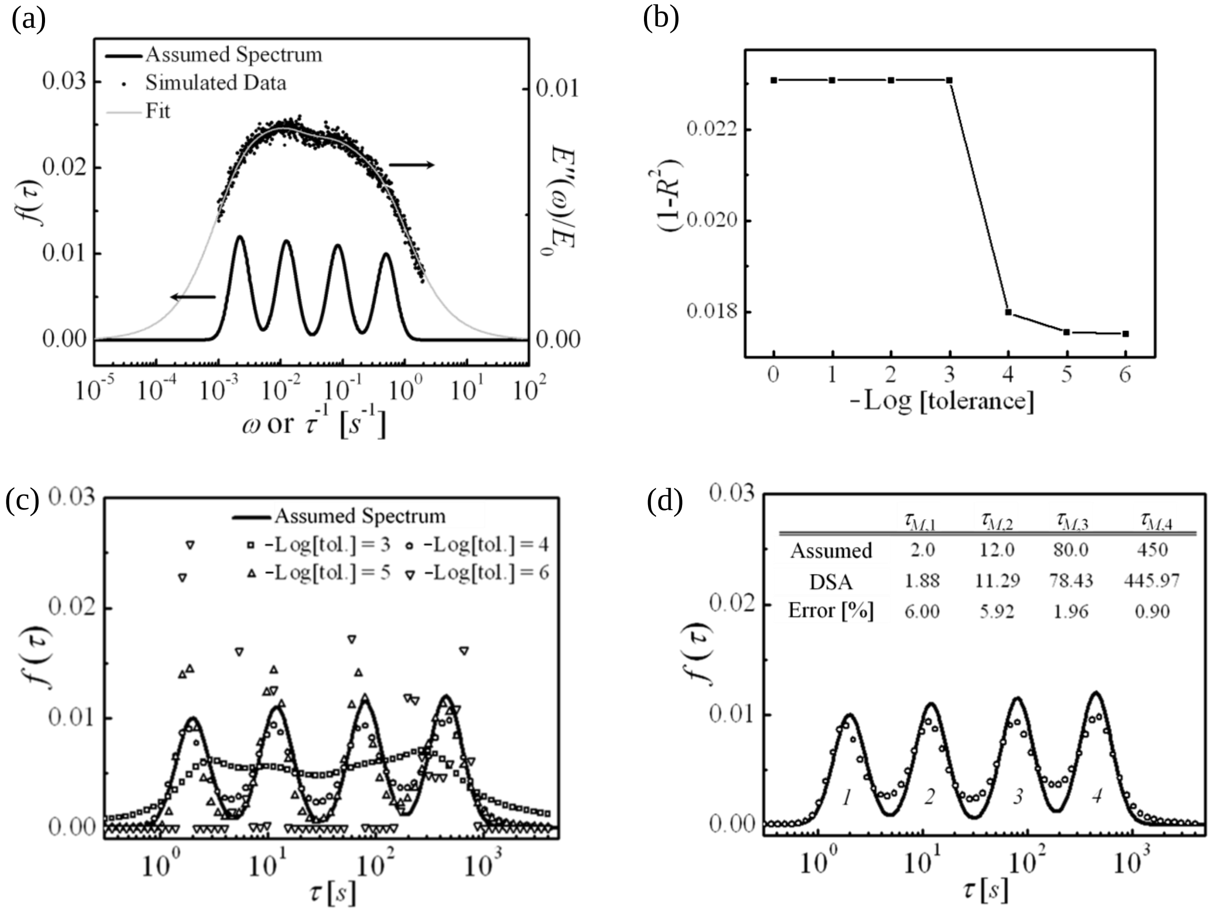

	$\tau_{M,1}$	$\tau_{M,2}$	$\tau_{M,3}$	$\tau_{M,4}$
Assumed	2.0	12.0	80.0	450
DSA	1.88	11.29	78.43	445.97
Error [%]	6.00	5.92	1.96	0.90

Figure 3.9 (a) Assumed relaxation-time spectrum with four distinct peaks on τ (solid line), given in Eqn. (3.17) and Table 3.1. Using the spectrum, a simulated data set (black dots) is created using Eqn. (3.9), replacing $g_\tau(t)$ with $\frac{\omega\tau}{1+\omega^2\tau^2}$, from ω_{min} = 10^{-3} to ω_{max} = 2 $sec.^{-1}$, adding normally distributed random noise with $\sigma_{stdev} = 2 \times 10^{-4}$. (b) $(1\text{-}R^2)$ as a function of prescribed -Log(tolerance) calculated by DSA from the simulated data in (a). (c) Relaxation-time spectra obtained by DSA from the simulated data in (a) at four different tolerance values (10^{-3} to 10^{-6}). (d) Best fit: Relaxation-time spectrum (open circles) obtained at the tolerance value of 10^{-4}, where $(1\text{-} R^2)$ precipitously drops, is plotted along with the assumed spectrum (solid line). The medians of the respective peaks, *i*, denoted as $\tau_{M,i}$, are summarized in the inset.

A simulated loss modulus data set, normalized by the high frequency Young's modulus (E_0), was created using Eqn. (3.9) and (3.17), replacing $g_\tau(t)$ with $\frac{\omega\tau}{1+\omega^2\tau^2}$, from $\omega_{min} = 10^{-3}$ to $\omega_{max} = 2\ sec.^{-1}$, including normally distributed random noise with $\sigma_{stdev} = 2 \times 10^{-4}$. DSA of the simulated data was performed with $N_2 = 70$ in Eqn. (3.16.b) from $\tau_{min} = (\omega_{max})^{-1}/4$ and $\tau_{max} = 4(\omega_{min})^{-1}$. A choice of a wide range of τ allowed for resolving possible spectrum peaks that contributed to the data, as discussed below. The spectrum obtained by DSA, $f(\tau_i)$, is given by:

$$f(\tau_i) = E_i / \Delta \ln \tau \,. \tag{3.18}$$

The IPOPT solver[17,18] employed for DSA allowed for fitting data at different prescribed tolerance values. While DSA performed with simulated quasi-static data with different tolerance values yielded consistent results, that for loss modulus needed to be examined at different tolerance values to find the optimum condition, yielding the assumed spectrum with best accuracy. The iterative fitting procedure is terminated when the following condition is satisfied:

$$tolerance > \left| \sum_{j=1}^{n} (y_j - (h(\omega_j))_k)^2 - \sum_{j=1}^{n} (y_j - (h(\omega_j))_{k+1})^2 \right| \Big/ \left(1 + \left| \sum_{j=1}^{n} (y_j - (h(\omega_j))_k)^2 \right| \right), \tag{3.19}$$

where y_j is the j^{th} value of the experimental (simulated) data, which comprise n data points, $(h(\omega_j))_k$ is the fit value at the j^{th} ω for k^{th} iteration, respectively. DSA was performed for several prescribed tolerance values from 10^0 to 10^{-6}. ($1-R^2$) as a function of -Log(tolerance) is shown in Fig. 3.9 (b), and the corresponding relaxation-time spectra are shown in Fig. 3.9 (c). Spectra obtained by DSA with decreasing tolerance values clearly showed better agreement with the original spectrum down to a tolerance value of 10^{-4}, at which ($1-R^2$) precipitously dropped. However, further decreases in tolerance led to worse fits. While the decrease in ($1-R^2$) with decreasing tolerance values was expected, the reason for this behavior is not clear. A number of tests with simulated data, however, consistently revealed that the highest quality of the fit to the assumed spectrum was obtained with decreasing tolerance at the first point at which R^2 closely approached 1. This best fit is plotted separately again, along with the assumed spectrum in Fig. 3.9 (d). For spectra with four peaks, the maximum error of $\tau_{M,i}$ was ~ 6 %, as summarized in the inset.

Experimental constraints typically limit the range of ω for dynamic loss modulus measurements. Since it is difficult to experimentally access the dynamic mechanical properties of a solid over a wide range of frequency due to the problems associated with the stability of instrumentation,[19] measured properties are often limited within a narrow range of ω. For example, the overall peak in $E''(\omega)$ (Fig. 3.9), may not be seen in the experiments, and only part of the loss modulus peak may be accessible, depending on temperature. In order to assess the reliability of DSA for extremely limited data range, we applied it to purposely-truncated simulated data.

The truncated curve in Fig. 3.10 (a) is the simulated loss modulus created using the assumed relaxation-time spectrum, using Eqn. (3.17) with $I = 8$. A_k, $\tau_{M,k}$ and C_k are given in Table 3.2:

	$k = 1$	$k = 2$	$k = 3$	$k = 4$	$k = 5$	$k = 6$	$k = 7$	$k = 8$
A_k	0.045	0.055	0.09	0.1	0.12	0.2	0.3	0.4
$\tau_{M,k}$	0.3	1	3.3	10	40	170	1100	20000
C_k	0.25	0.25	0.25	0.25	0.25	0.3	0.5	0.7

Table 3.2 Assumed values of A_k, $\tau_{M,k}$ and C_k for $f(\tau)$ in Eqn. (3.17) and Fig. 3.10.

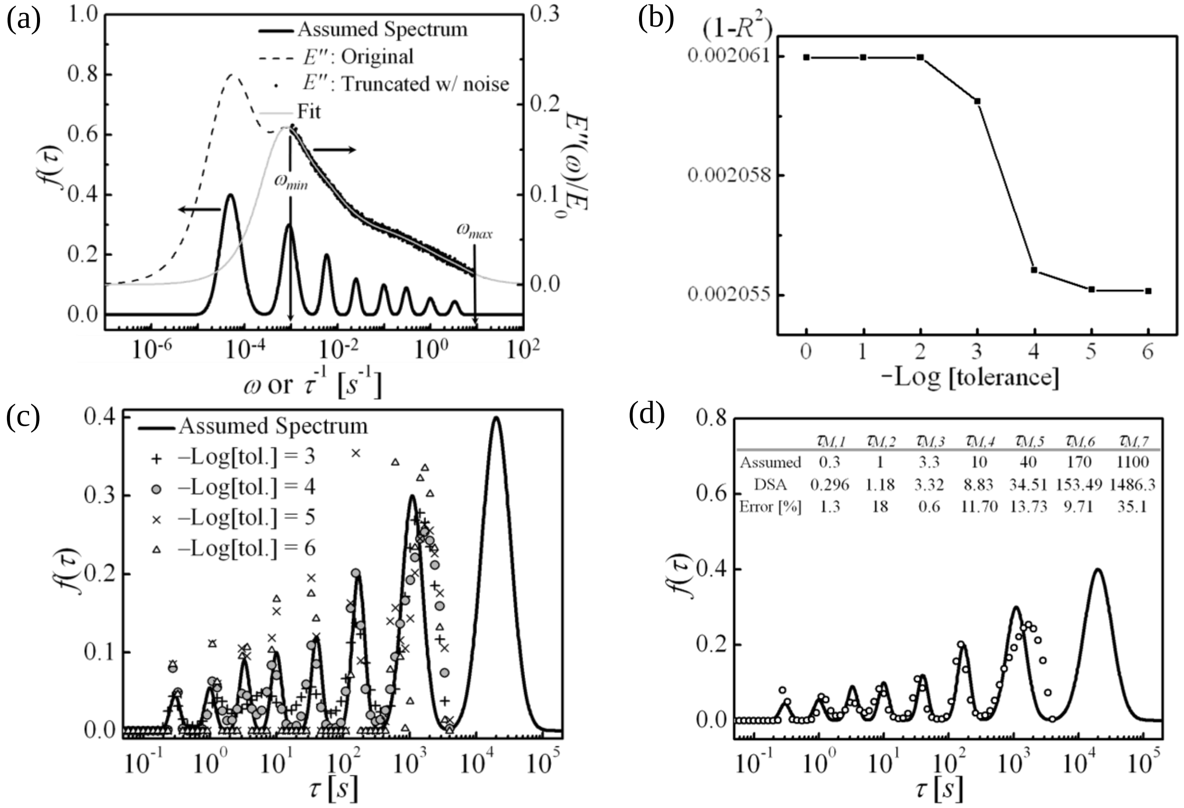

	$\tau_{M,1}$	$\tau_{M,2}$	$\tau_{M,3}$	$\tau_{M,4}$	$\tau_{M,5}$	$\tau_{M,6}$	$\tau_{M,7}$
Assumed	0.3	1	3.3	10	40	170	1100
DSA	0.296	1.18	3.32	8.83	34.51	153.49	1486.3
Error [%]	1.3	18	0.6	11.70	13.73	9.71	35.1

Figure 3.10 Assumed relaxation-time spectrum with eight distinct peaks on τ (solid line), given in Eqn. (3.17) with $I = 8$ and Table 3.2. Using the spectrum, a simulated data set (black dots) is created using Eqn. (3.9) and (3.17), replacing $g_\tau(t)$ with $\frac{\omega\tau}{1+\omega^2\tau^2}$, from $\omega_{min} = 10^{-3}$ to $\omega_{max} = 9$ *sec.*$^{-1}$, adding normally distributed random noise with $\sigma_{stdev} = 2 \times 10^{-3}$. The truncated data are limited to $\omega_{min} = 10^{-3}$ and $\omega_{max} = 9$ *sec.*$^{-1}$. (b) $(1-R^2)$ as a function of -Log(tolerance) calculated for DSA results at six different tolerance values. (c) Relaxation-time spectra obtained by DSA with $\tau_{min} = (\omega_{max})^{-1}/4$ and $\tau_{max} = 4(\omega_{min})^{-1}$ from the truncated simulated data in (a) that include noise at four different tolerance values (10^{-3} to 10^{-6}). (d) Best fit: Relaxation-time spectrum (open circles) obtained at the tolerance value of 10^{-4}, where $(1-R^2)$ precipitously drops, together with the assumed spectrum (solid line). The median values of the respective peaks, *i*, denoted as $\tau_{M,i}$, are summarized in the inset.

$\tau_{M,k}$ values are chosen with a variable spacing in $\ln\tau$ in order to assess the reliability of DSA under challenging condition. The spectrum is shown with a solid line in the figure. The assumed spectrum contained eight distinct peaks spanning over six decades of time with different intensities, therefore, the loss modulus is significant over a wide range of frequencies, with noticeable asymmetry. After adding normally distributed random noise with $\sigma_{stdev} = 2 \times 10^{-3}$, we applied DSA to the data, truncated to $\omega_{min} = 10^{-3} < \omega < 9 = \omega_{max}$ $sec.^{-1}$ and including ~ 900 data points. Using $N_2 = 70$ in Eqn. (3.16.b) with τ_i ranging from $\tau_{min} = (\omega_{max})^{-1}/4$ and $\tau_{max} = 4(\omega_{min})^{-1}$, DSA was performed at different prescribed tolerance values.

$(1-R^2)$ as a function of tolerance for DSA is plotted in Fig. 3.10 (b), and the corresponding relaxation-time spectra are plotted in Fig. 3.10 (c). As observed in Fig. 3.9, the relaxation-time spectrum obtained at the tolerance value associated with the drastic decrease in $(1-R^2)$, showed the best fit to the assumed spectrum. More importantly, although the best-fit spectrum obtained from DSA in Fig. 3.10 (d) showed slight over/underestimation of the respective peak widths/heights, DSA yielded seven distinct peaks, $\tau_{M,i}$, showing reasonably good agreement with the assumed values, as summarized in Fig. 3.10 (d). Because of the intrinsic width of the Debye peak corresponding to each τ value (Eqn. 3.16.b), peaks with medians outside the measured range still contribute to the DSA results. This significant result shows that DSA allowed us to analyze the dynamic properties, despite the great overlap of several processes in loss modulus, and the limited ω range of the data.

It is noted that the wide range of τ ($\tau_{min} = (\omega_{max})^{-1}/4$ and $\tau_{max} = 4(\omega_{min})^{-1}$) in Fig. 3.10 allowed for estimating $\tau_{M,i=7}$, where $\tau_{M,i=7} > (\omega_{min})^{-1}$. Relaxation-time spectra, obtained by DSA using the same simulated data as in Fig. 3.9 (a) and 3.10 (a) following the same procedures, but with a narrower τ range ($\tau_{min} = (\omega_{max})^{-1}/2$ and $\tau_{max} = 2(\omega_{min})^{-1}$), are shown in Fig. 3.11 (a) and (b), respectively. For any peak *i*, such that $(\omega_{max})^{-1} < \tau_{M,i} < (\omega_{min})^{-1}$, the choice of a narrower τ range did not affect the fitting results for that peak, as shown in Fig. 3.11 (a). However, when truncated simulated data were used, so that $\tau_{M,i=7} > (\omega_{min})^{-1}$, DSA performed with the narrower τ range did not reproduce the peak ($i = 7$), as shown in Fig. 3.11 (b), resulting in a larger error in $\tau_{M,i=7}$.

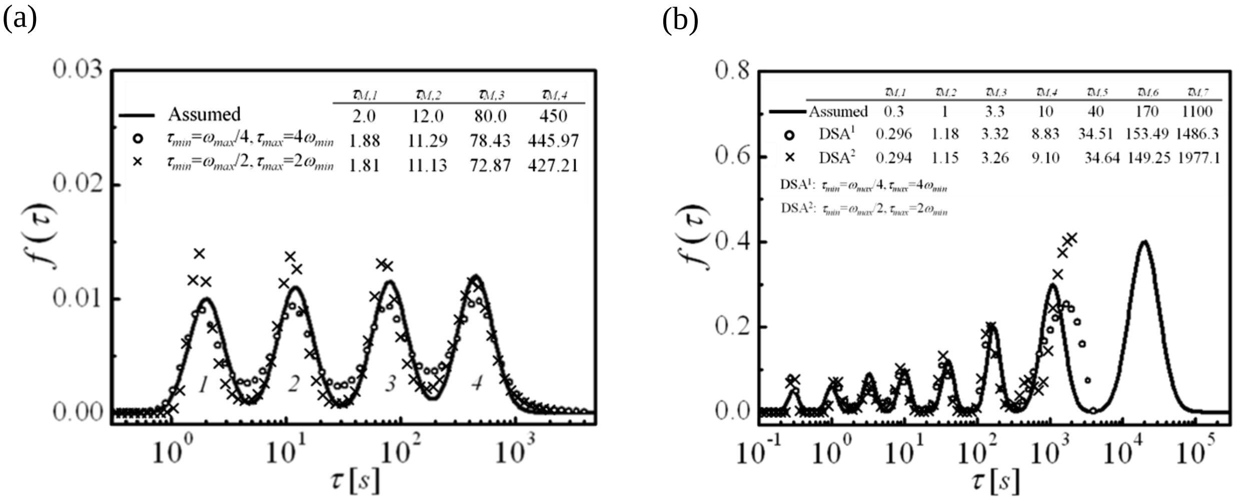

Figure 3.11 (a) Relaxation-time spectrum (cross symbols: ×) obtained by DSA from the original simulated data in Fig. 3.9 (a) using two τ ranges ($\tau_{min} = (\omega_{max})^{-1}/2$ and $\tau_{max} = 2(\omega_{min})^{-1}$) and ($\tau_{min} = (\omega_{max})^{-1}/4$ and $\tau_{max} = 4(\omega_{min})^{-1}$). (b) Same as (a), but for the truncated simulated data set in Fig. 3.10 (a). $\tau_{M,i}$ values are summarized in the inset.

It should be noted that, in the analysis of simulated data, we know the part of peak, $i = 7$, of the DSA results corresponds to $\tau_{M,i=7}$ of the assumed relaxation-time spectrum. When the part of peak is observed in the experimental data, however, the peak needs to be verified by performing DSA with a wider τ range. Therefore, DSA was performed for loss modulus data sets from Ref.

20 in order to determine the best fit with two different τ ranges, $(\omega_{max})^{-1}/2$ and $\tau_{max} = 2(\omega_{min})^{-1}$, and $\tau_{min} = (\omega_{max})^{-1}/2$ and $\tau_{max} = 4(\omega_{min})^{-1}$, to rule out potential artifacts (See Chapter 5). Codes written to perform DSA are detailed and explained in Appendix B.

3.7 SUMMARY

A combination of cantilever bending and bend-stress relaxation measurements was employed to measure the anelastic strain spanning over greater than ~ nine decades of time. The strain was proportional to the displacement, h_0, and inversely proportional to the radii of curvature of a sample, r, for cantilever bending and bend-stress relaxation measurements, respectively. Therefore, these were monitored as a function of time, t, from sub-millisecond to 200 *sec.* for cantilever bending measurements, and from minutes to ~ 8×10^7 *sec.* for bend-stress relaxation measurements. Both as-quenched and structurally relaxed samples were used. The relaxed samples were obtained by annealing as-quenched samples at 110 ^oC for 1 *hr.*, a condition that did not lead to crystallization. Their amorphous structure was confirmed by the high-resolution transmission electron micrographs.

Computational methods employed to obtain the relaxation-time spectra by DSA are evaluated. The challenge was to probe the distribution of time constants in a quasi-continuous fashion, which allowed for a higher-quality fit, in the presence of scatter in the data. It was essential to assess the reliability of DSA, and therefore, tests, employing simulated data, were performed for both static and dynamic cases. While DSA performed using Mathematica© with the simulated data that did not contain noise, yielded the assumed spectrum with good accuracy, it was not successful even when the small noise was added to the data. DSA performed with the non-linear solver IPOPT,[17,18] however, allowed for resolving this noise problem, reproducing the assumed spectrum with fairly good accuracy for both static and dynamic data. The noise level added to simulated data was similar or greater than that of the experimental data (See Chapter 4 and 5). Effects of the initial guesses, range of τ_i, and tolerance values on the DSA results were examined. While a choice of different initial guesses did not affect the results, a wide range of τ allowed for resolving possible spectrum peaks near the maximum measurements duration. For dynamic data, the tolerance value at which $(1\text{-}R^2)$ drastically decrease showed the best fit to the assumed spectrum. Based on these results, obtained from the simulated data, the same procedures were applied to the experimental data. The results of experimental data for quasi-static and dynamic cases are discussed in Chapter 4 and 5, respectively.

3.8 REFERENCES

[3.1] J. R. Cost, *J. Appl. Phys.* **54**, 2137 (1983).
[3.2] S. Timoshenko and J. N. Goodier, *Theory of elasticity*, McGraw-Hill (1969).
[3.3] S. Timoshenko and S. Woinowsky-Krieger, *Theory of plates and shells*, McGraw-Hill (1959).
[3.4] M. Vable, *Mechanics of materials*, Oxford University Press (2002).
[3.5] W. F. Hosford, *Mechanical behavior of materials*, Cambridge University Press (2005).
[3.6] M. A. Meyers and K. K. Chawla, *Mechanical Metallurgy: Principles and Application*, Prentice-Hall, Inc. (1983).
[3.7] G. E. Dieter, *Mechanical metallurgy*, McGraw-Hill (1986).
[3.8] T. P. Weihs, S. Hong, J. C. Bravman and W. D. Nix, *J. Mater. Res*. **3**, 931 (1988).
[3.9] J. M. Freitag, R. G. Koknaev, R. Sabet-Sarghi, M. Koknaeva and Z. Altounian, *J. Appl. Phys.* **79**, 3967 (1996).
[3.10] S. Timoshenko and J. M. Lessells, *Applied elasticity*, Westinghouse Technical Night School Press (1925).
[3.11] W. H. Jiang, F. E. Pinkerton and M. Atzmon, *Acta Mater*. **53**, 3469 (2005).
[3.12] A. S. Argon and H. Y. Kuo, *J. Non-Crys. Sol*. **37**, 241 (1980).
[3.13] A. I Taub and F. Spaepen, *J. Mater. Sci*. **16**, 3087 (1981).
[3.14] R. Kohlrausch, *Ann. Phys. Leipzig* **91**, 56 (1854).
[3.15] J. R. Cost, *J. Appl. Phys.* **54**, 2137 (1983).
[3.16] V. Ocelík, K. Csach, A. Kasardová and V. Z. Bengus, *Mater. Sci. Eng.* ***A*226-228**, 851 (1997).
[3.17] A. Wächter and L. T. Biegler, *Mathematical Programming* **106** (1), 25 (2006).

[3.18] R. Fourer, D. M. Gay and B. W. Kernighan, *AMPL: A Modeling Language for Mathematical Programming*, Scientific Press, South San Francisco, CA (1993).
[3.19] W. Flügge, *Viscoelasticity*, Springer-Verlag, (1975).
[3.20] J. M. Pelletier, *J. Alloys Comp*. **393**, 223 (2005).

Chapter 4

QUASI-STATIC PROPERTIES

Results of a combination of cantilever bending and bend-stress relaxation measurements are presented and discussed in this chapter. In Section 4.1, relaxation-time spectra for quasi-static anelastic strain relaxation in amorphous $Al_{86.8}Ni_{3.7}Y_{9.5}$ (*at.*%), showing several distinct peaks, are obtained by DSA. The spectra, in conjunction with a model employing Voigt units in series, have allowed us to characterize STZ properties in detail. These results are compared in Section 4.2 with those obtained over longer period of time ~ 8×10^7 *sec.* in a stress-free state, until the remaining anelastic strain essentially vanished. In addition, extrapolation used to estimate the volume fraction of potential STZs for large time constants is discussed. In Section 4.3, the effect of structural relaxation on STZ properties, obtained using the same methods, is discussed. In Section 4.4, a criterion for an atomic cluster being a potential STZ is developed to account for its size and free volume dependence.

4.1 AN ATOMICALLY QUANTIZED HIERARCHY OF STZS

This section is a verbatim copy of Ref. 1 (© 2011 American Institute of Physics. [doi:10.1063/1.3552300]).

AN ATOMICALLY QUANTIZED HIERARCHY OF SHEAR TRANSFORMATION ZONES IN A METALLIC GLASS

J. D. Ju,[1] D. Jang,[2] A. Nwankpa[3] and M. Atzmon [1,4]

[1]Department of Materials Science and Engineering, University of Michigan, Ann Arbor, MI 48109, USA.
[2]Department of Materials Science and Engineering, California Institute of Technology, Pasadena, CA 91125, USA.
[3]Computer Aided Engineering Network, University of Michigan, Ann Arbor, MI 48109, USA.
[4]Department of Nuclear Engineering and Radiological Sciences, University of Michigan, Ann Arbor, MI 48109, USA.

Quasi-static measurements of room-temperature anelastic relaxation were used to characterize the properties of shear transformation zones (STZs) in amorphous $Al_{86.8}Ni_{3.7}Y_{9.5}$ in the dilute limit. Using a combination of nanoindenter cantilever bending and mandrel bend relaxation techniques, anelastic relaxation was measured over times ranging from 1 s to 3×10^{7} s. Direct spectrum analysis yields relaxation-time spectra, which display seven distinct peaks. The results were analyzed using a linear dashpot-and-spring model, combined with transition-state theory, to yield several STZ properties. These reveal a quantized hierarchy of STZs that differ from each other by one atomic volume. Potential STZs occupy a large volume fraction of the solid. They access their ergodic space, with the ratio of forward-to backward jump rates ranging from 1.03 to 4.3 for the range of stress values used. [doi:10.1063/1.3552300]

INTRODUCTION AND BACKGROUND

Metallic glasses exhibit high strength and elastic limit, properties that are attractive for a variety of structural applications.[2] However, they also exhibit flow localization, which results in macroscopically brittle behavior. While significant progress has been made in understanding their mechanical behavior since the pioneering work by Spaepen,[3] a detailed microscopic description of viscoelastic flow of metallic glasses remains a challenging task. Plastic deformation of crystalline materials has long been well-understood, and described in terms of well-defined lattice defects. However, glasses pose significant challenges in defining flow defects, as even the baseline structure is poorly known. Recent reviews of deformation of metallic glasses have been given by Schuh *et al*.[4] and Trexler and Thadhani.[5]

Spaepen's model[3] has been successful in describing a range of observations on flow and flow localization. Argon[6,7] added microscopic details, based on insight gained from two-dimensional bubble rafts.[8,9] He identified low-stress flow defects as microscopic, equiaxed, regions, termed shear transformation zones (STZs). The shear transformations are thermally activated and assisted by external stress, and the transformation shear strain , γ_0^T, is of the order of 0.1. Both authors expressed the shear rate in terms of transition-state theory, with a barrier height biased by an applied stress. Argon and Shi argued[7] that isolated STZs can be reversed by back-stress in the elastic matrix, leading to macroscopic anelasticity. In fact, simulations[10] and experiments[11,12] show an anelastic contribution to apparent elastic behavior in metallic glasses, with the simulations showing a bond-breaking mechanism. Egami *et al*.[13] correlated anelastic deformation with bond-orientational order. Argon and Kuo[14] used temperature-stepping experiments to determine activation energy spectra for anelastic relaxation for several metallic glasses. Increased attention has recently been given to the behavior of shear transformation zones, using three-dimensional colloids[15] and molecular dynamics (MD) simulations.[16,17] Despite the progress made, the lack of matrix periodicity and the small size of STZs have made their direct experimental characterization elusive.

In order to investigate the properties of STZs, we have conducted quasi-static anelastic relaxation measurements in amorphous $Al_{86.8}Ni_{3.7}Y_{9.5}$, an alloy previously studied by one of the authors.[18,19] Unlike some Al-rich metallic glasses, this alloy does not crystallize upon room-temperature plastic deformation. It exhibits significant anelastic deformation at room temperature, enabling us to conduct stable, high resolution, measurements for durations of 1*s* – 3×10^7 *s*. Our simple experiments provide valuable information on STZ properties. Most importantly, we obtain evidence of a quantized hierarchy of STZs with single-atom increments.

EXPERIMENTAL PROCEDURE

An amorphous $Al_{86.8}Ni_{3.7}Y_{9.5}$ (*at*.%) ribbon. 22 *µm* thick and 1 *mm* wide, was obtained by the single-wheel melt-spinning technique using a Cr-coated Cu wheel at a tangential velocity of 40 *m*/*s* in vacuum. Electron diffraction analyses were employed to confirm the amorphous structure of the as-spun alloy ribbon.

All relaxation measurements were performed at 295 ± 1 *K*. An Agilent G200 nanoindenter with a DCM head was used for the cantilever measurements (Fig. 4.1 (a)). Cantilever samples were mounted in epoxy for nanoindenter experiments, and the distance between the clamp and indenter tip contact point was 0.1 *cm*. Two different mounting compounds were used in order to rule out their effect on the measurement. Thermal drift was subtracted. In each run, the following cycle, consisting of three stages, was repeated 20 times: 0.2, 0.02 and 0.002 *mN*, each for 200 *s*. The stiffness measured from the instantaneous, elastic, displacement agreed with the calculated value,[20] based on a Young's modulus value of E_0=48.2 GPa[21] for a similar alloy. Displacement versus time data obtained during each full-load stage were used in the analysis, each consisting of 5000 points. Reversibility was confirmed during the low-load parts of each cycle. Throughout this paper, ε refers to the maximum bending (x direction in Fig. 4.1 (a)) strain, attained at the surface. For the cantilever, this maximum strain is attained at the fixed end of the sample, and is given by $\varepsilon = \frac{3}{2}\frac{d \cdot h}{L^2}$,[20] where d is the sample thickness, h its displacement, and L its effective length. The elastic strain, ε_{el}^{0}, is constant under fixed nanoindenter load, and is determined from the instant deflection in response to a jump in load. Its value is less than 10^{-4} for all measurements. The time-dependent strain value, normalized by ε_{el}^{0}, is equal to the ratio of the corresponding displacements. A total of 95 measurement cycles were obtained from four different samples.

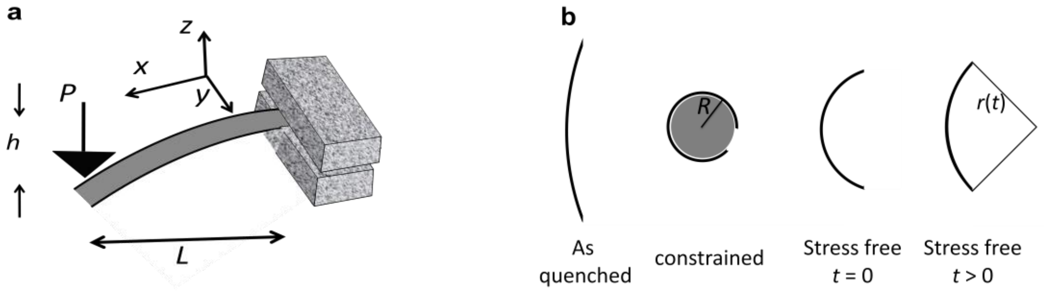

Figure 4.1 Measurement techniques. (a) Cantilever method. The displacement h is monitored as a function of time at a fixed load, P. The instantaneous displacement is the elastic component; (b) Mandrel method. The sample was constrained for 2×10^{6} s at varying radii, after which the radius of curvature was monitored as a function of time in a stress-free condition.

For the bend stress relaxation ("mandrel") experiment,[22,23] Fig. 4.1 (b), five 1 *cm* long samples were used. Samples were first constrained around mandrels of radius ranging from 0.35-0.49 *cm* for 2×10^6 *s*, then allowed to relax stress-free for 3×10^7 *s*. The radius of curvature was monitored during relaxation as a function of time using a digital camera, taking care to insure that its optical axis was perpendicular to the sample stage, which was illuminated with a backlight. The curvature was determined by on-screen visual fitting of the calibrated photo with a circle. Under constraint, the total bending strain at the surface is $\varepsilon^T = d/2(1/R - 1/r_0)$, where R is the mandrel radius and r_0 is the initial sample radius of curvature. ε^T consists of an elastic and anelastic contribution, the values of which at the end of the constraining period are $\varepsilon_{el}^0 = d/2\times[1/R - 1/r(0)]$ and $\varepsilon_{an}^0 = d/2\times[1/r(0) - 1/r_0]$, respectively, where $r(t)$ is the radius of curvature at time t after removal of the constraint. Note that ε_{el}^0, which is defined differently for the cantilever and mandrel experiment, is the elastic strain at mechanical equilibrium in both cases. The maximum bending strain at time t after removal of the constraint is given by $\varepsilon(t) = d/2\times\left(1/r(t) - 1/r_0\right)$. These expressions assume a neutral plane equidistant from the surfaces. Since we find the processes under consideration to be linear functions of the stress, the strain varies linearly across the sample thickness, justifying the assumption. For the different mandrel radii used, ε_{el}^0 ranged from 0.153 to 0.303 %. The maximum shear stress is given by $\sigma_s = \frac{\sigma_x - \sigma_z}{2} = \frac{\sigma_x}{2} = \frac{E_0}{2(1-\nu^2)}\varepsilon_x$ since the out-of-plane stress, σ_z, is zero. The maximum shear strain is given by $\gamma = \varepsilon_x - \varepsilon_z = \varepsilon_x/(1-\nu)$, where ε_z is the out-of-plane strain. It is important to note that because the in-plane perpendicular stress, σ_y, is proportional to σ_x, relative changes in σ_x and ε_x due to any linear process are the same as they would be for uniaxial geometry.

Direct spectrum analysis[24] was performed by fitting the relaxation curves, using the Primal-Dual Interior Point Filter Line Search Algorithm. The software package AMPL[25] was used with nonlinear solver IPOPT.[26] In the fits, the relaxation-time values, τ_i, were fixed and spaced logarithmically in the ranges 0.3 to 400 s and 1080 to 5.4×10^7 s for the cantilever and mandrel experiments, respectively. Each experimental curve was fitted to obtain a relaxation-time spectrum, $f(\tau)$. To obtain the integral over peak m, $\int_m f(\tau) d \ln \tau$, for overlapping peaks in the spectra, $f(\tau)/\tau$ was fitted with sums of log-normal functions, yielding excellent agreement. STZ properties were calculated for each peak in each spectrum, and then averaged over the spectra. The error indicated in the plots is the standard deviation of the mean.

RESULTS AND DISCUSSION

The maximum anelastic bending strain of mandrel samples, equilibrated under constraint for 2×10^6 s and subsequently allowed to recover, is shown, normalized by ε_{el}^0, as a function of time in Fig. 4.2. As with any static measurement, ε_{el}^0 may include anelastic contributions[11,12] with time scales shorter than the experimental resolution. The curves in Fig. 4.2 indicate absence of significant permanent strain and are independent of ε_{el}^0. The implied linearity in stress leads to important conclusions: a) the anelasticity is unlikely to originate from macroscopically heterogeneous behavior, but rather has microscopic origin, b) the anelastic sites are not exhausted for the strain values used, c) the viscosity in the linear solid model, used below, is Newtonian, i.e., their strain rate of the dashpots is proportional to their stress and d) consequently, unlike for the case of yield, the strain profile is linear across the sample thickness at any time. In Fig. 4.2, for the highest value of applied strain, the maximum anelastic bending strain at the end of the constraining period, t = 0, is about 0.055%. Assuming the shear strain of an STZ (Ref. 6) when constrained by the surrounding matrix is γ_0^c=0.09 (see below), and converting bending to shear strain, the corresponding total volume fraction occupied by activated STZs is about 0.94%.

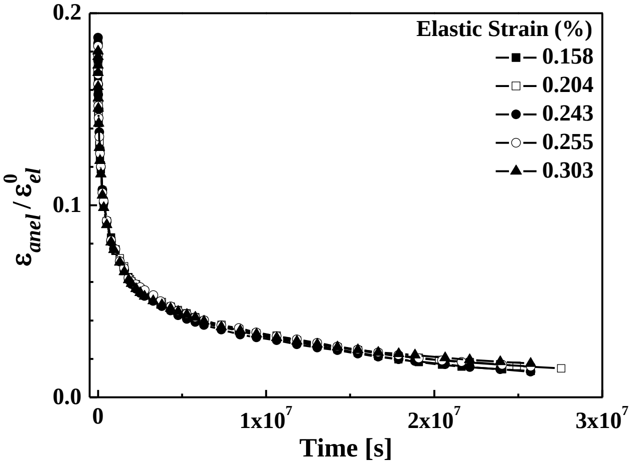

Figure 4.2 Anelastic strain evolution following equilibration at different mandrel radii. The strain is normalized by the elastic strain at equilibrium, prior to removal of the constraint.

In order to observe anelastic relaxation with time scales of 1 s – 200 *s*, the displacement of cantilever samples at constant load, P = 0.2 *mN*, Fig. 4.1 (a), was monitored as a function of time. Its division by the instantaneous displacement upon loading yielded the ratio of anelastic to elastic bending strain, $\varepsilon_{an}(t)/\varepsilon_{el}^0$. Sample curves for both measurements are shown in Figs. 4.3 (a) and (b).

Because anelastic relaxation in a metallic glass involves several processes, the temporal evolution of the strain is typically fitted with a linear combination of exponentially decaying terms, exp(-t/τ), with different time constants, τ. Alternatively, a single stretched exponent has been used, $\exp(-(t/\tau)^{\beta})$,[27] implicitly making an assumption about the shape of the relaxation spectrum. Instead, we employ a direct spectrum analysis method[24] by fitting the following functions to the anelastic strain as a function of time:

$$\varepsilon = A + Bt + \sum_{i=1}^{N_1} \varepsilon_i \exp(-t/\tau_i) \tag{4.1.a}$$

$$\varepsilon = A + \sum_{i=1}^{N_2} \varepsilon_i \exp(-t/\tau_i) \tag{4.1.b}$$

for the cantilever and mandrel measurement, respectively, with N_1 and N_2 less than the number of data points. The ε_i are fitting parameters, and the τ_i are fixed and spaced logarithmically. The linear term in Eqn. (4.1.a) *a priori* describes plastic flow or approximates anelastic processes with time constants greater than the measurement duration. A in Eqn. (4.1.b) is very small and likely corresponds to processes with time constants longer than the duration of the experiment.

It should be noted that even in a simulated relaxation curve consisting of a sum of a small number of pure exponential terms that differ from each other by a factor of ten, it is difficult to discern the different time constants. This is especially true when the amplitude of the exponents with the longest time constants is the greatest, since these introduce a curvature in a $\log(\varepsilon)$ versus time plot at short times. Experimental noise, and the fact that the spectrum peaks have an intrinsic width, further obscure any distinct processes. Because of the consequent need to rely on fits, we undertook several steps to rule out artifacts due to the fitting method. We have: a) performed fits with several values of N_1, N_2; and b) fitted the mandrel data with 4-8 exponents, allowing both the ε_i and τ_i to vary. The results of the different methods were consistent with each other. Regardless of the number of exponents used, the same dominant time constants were obtained. In addition, simulated data, containing noise, were fitted in order to assess the method's reliability. While the peak widths varied with initial guesses, their areas did not.

The spectra resulting from the fits, *f(τ)*, are included in Figs. 4.3 (a) and (b). These are normalized such that $\varepsilon_{el}^{0} \times \int_{\tau_1}^{\tau_2} f(\tau)\, d\ln\tau$ is the equilibrium anelastic bending strain due to processes with time constants in any interval (τ_1, τ_2). $f(\tau)/\tau$ exhibits a distinct set of peaks, each described well with a log-normal distribution.

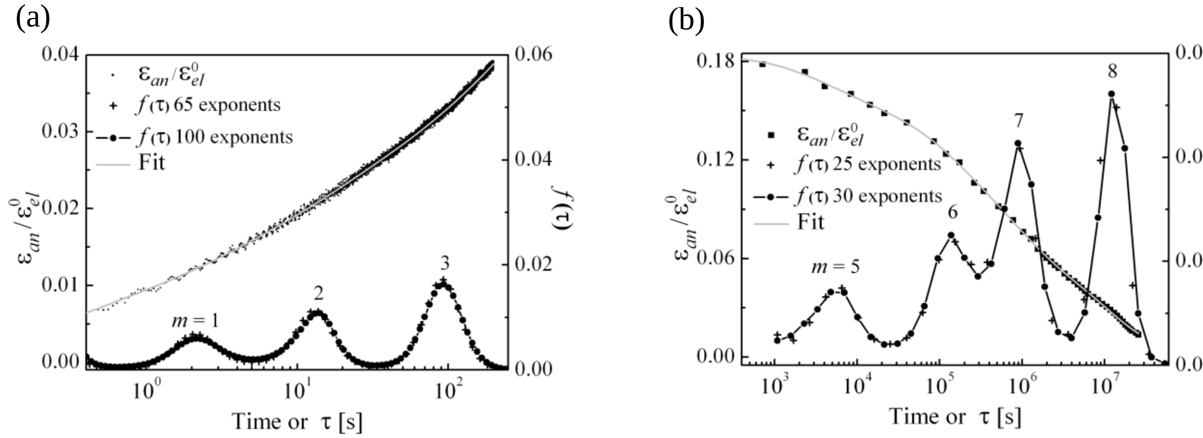

Figure 4.3 Sample relaxation curves and corresponding relaxation-time spectra**.** (a), Cantilever measurement, performed at fixed load, $P = 0.2\ mN$, i.e., fixed stress. (b), Mandrel measurement, performed in a stress-free condition after equilibration under constraint. For each case, two spectra, *f(τ)*, are shown, obtained from fits with different numbers of fitting parameters.

We associate peak in the spectra with one STZ type, *m*. To analyze the relaxation behavior, the standard linear solid model[28,29] is used, as illustrated in Fig. 4.4 (a) Voigt unit *m*, consisting of a spring and linear dashpot in parallel, represents all anelastic sites of type *m*, corresponding to one peak in the spectrum (Fig. 4.3 (a) and (b)). Since the strain contribution of each STZ type is additive, the units are connected in series. The additivity implies that both the effective Young's modulus and shear viscosity, E'_m and η'_m, respectively, are inversely proportional to the density of *m*-type STZs. In the limit of vanishing concentration of *m*-type STZs, $E'_m,\ \eta'_m \to \infty$, i.e., the corresponding Voigt unit is rigid and makes a negligible contribution to the strain. It is important to recognize the limitations of this simple model: Argon and Shi[7] note that once an STZ has other STZs as neighbors, its transformation is likely to become irreversible. This is equivalent to destruction of the spring that is parallel to a dashpot. In the present work, conducted at low strains and showing full reversibility, such a process is not encountered.

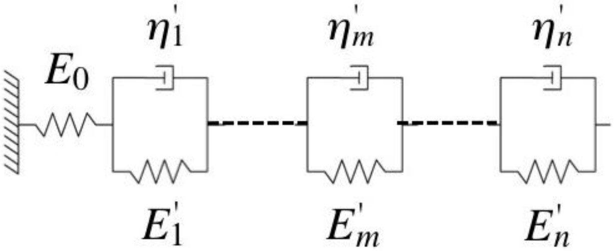

Figure 4.4 Linear solid model: *n* anelastic processes act in series, where *m*–type sites are associated with Young's modulus of E'_m and viscosity η'_m, both effective quantities that are inversely proportional to the volume fraction of these sites.

Using appropriate boundary conditions, exponential relaxation of stress and strain is obtained. Under fixed or zero stress, the different units evolve independently with time constants,

$$\tau_m = \frac{3\eta_m'}{E_m'} , \tag{4.2}$$

where the factor of 3 accounts for the conversion of uniaxial to shear viscosity. τ_m will be taken as the median of the respective (log-normal) peak, since it will yield the peak-averaged activation energy, ΔF_m, below.

Mechanical equilibrium between unit m and the spring in Fig. 4.4 yields the effective Young's modulus associated with the unit:

$$E_m' = \frac{\varepsilon_{el}^0}{\varepsilon_m^0} E_0 , \tag{4.3}$$

where E_0 is Young's modulus, and $\varepsilon_m^0 = \varepsilon_{el}^0 \times \int_m f(\tau) d\tau$, with integration over peak m, is the anelastic bending strain due to m-type sites at mechanical equilibrium. Eqn. (4.3) would remain the same if the ratio of shear strains were used, since these are linear in the tangential strain for the present geometry. The assumption of mechanical equilibrium between each STZ type and the matrix is valid for all but m=8, since τ_8=1.25×10^7 s, as compared with a constraint duration of 2×10^6 s. A corresponding correction is implemented in the analysis below.

Once E_m' and τ_m are determined from the spectra, Eqn. (4.2) is used to calculate η_m'. Below, we will relate it to the additive contribution of m-type STZs to the macroscopic anelastic shear strain rate,

$$\dot{\gamma}_m = \frac{\sigma_s}{\eta_m} , \tag{4.4}$$

where σ_S is the net shear stress on the dashpot in Voigt unit *m*, equal to the applied stress minus that of the corresponding spring. Since our samples exhibit linear deformation behavior, η'_m is constant, and σ_s and $\dot{\gamma}_m$ vary linearly, across the thickness. Therefore, Eqn. (4.4) is valid for the entire sample. Following our convention for ε, maximum values of σ_s and $\dot{\gamma}_m$, attained at the surface, are used in the analysis below.

The volume fraction occupied by *potential*, (also known as *fertile*), *m*-type anelastic sites, can be expressed as

$$c_m = \frac{\varepsilon_m^0}{\varepsilon_{el}^0} = \frac{E_0}{E'_m} \quad , \tag{4.5}$$

as derived in the Appendix. The full physical meaning of c_m is discussed below. Equation (4.5) is obtained by modeling an anelastic unit *m* as a large number of potential STZs in series, all of which are reversible due to the same elastic constant as the solid.[3,6] The main step in modeling STZs , which have on/off states, with Voigt units that have a continuum of strain states is based on the ergodicity of STZs: since equilibrated STZs undergo thermal fluctuations that are only biased by the stress (see below and Ref. 15), the *ensemble average*, the activated fraction, x_m, of c_m at mechanical equilibrium, can be interpreted as the average fraction of time each potential STZ is transformed. Thus, an STZ has a continuum of time-averaged strain values. While kinetic measurements can involve significant uncertainty in pre-exponential factors, Eqn. (4.5) allows for a reliable measurement of c_m. It does not depend on γ_0^T and applies to any STZ type that has equilibrated.

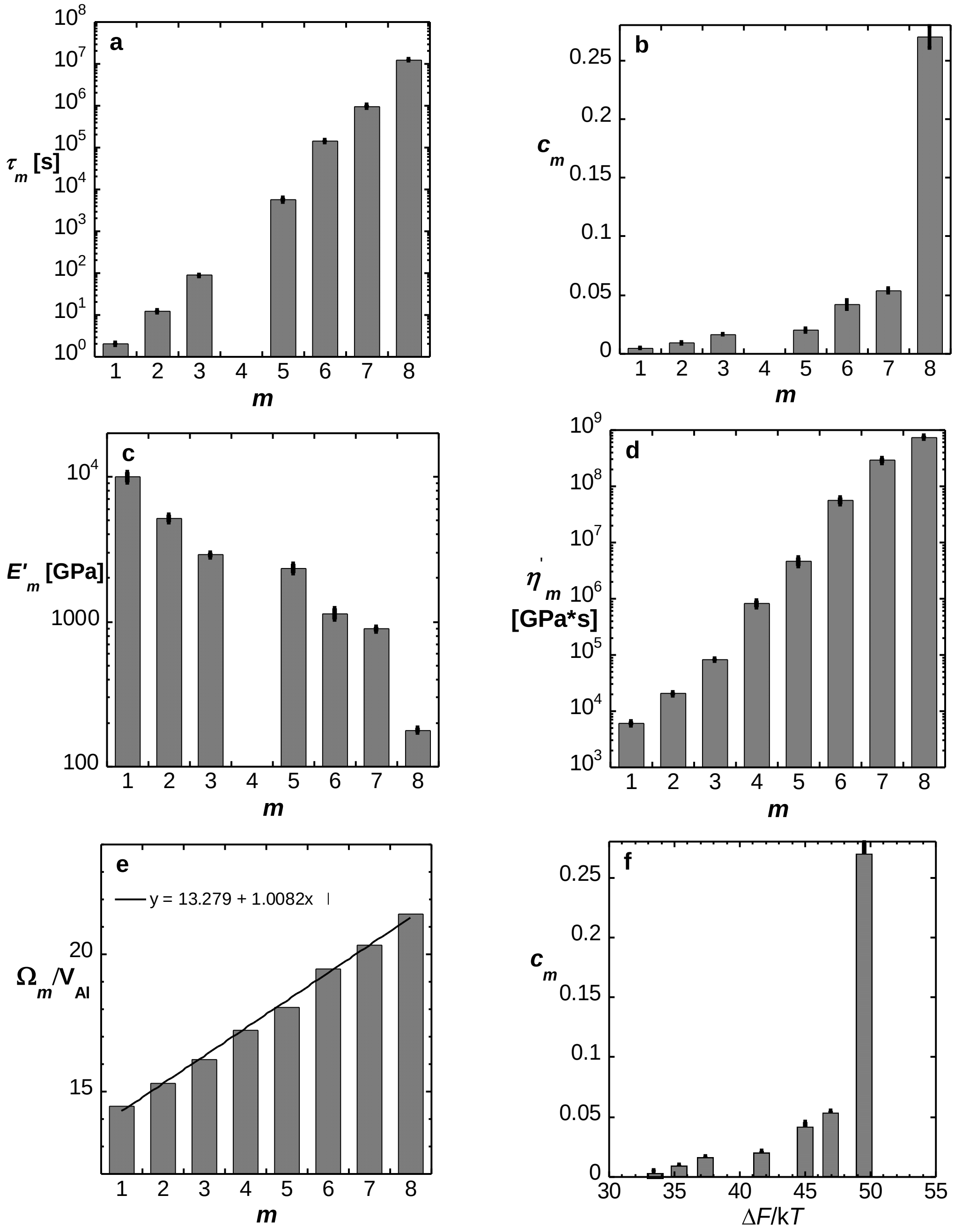

Figure 4.5 Calculated properties of the respective anelastic processes *m* = 1-8. (a), Time constants. (b), Volume fraction of *potential* STZs; (c), Effective macroscopic Young's modulus. (d), effective macroscopic viscosity. (e), STZ volume in units of atomic volume of Al, $V_{Al}=16.6\text{x}10^{-30}$ m^3. The value for *m*=4 was obtained from Fig. 4.4 (d) and interpolation in Fig. 4.4 (b). (f), Volume fraction of *potential* STZ and transformation strain as a function of Δ*F/*k*T*. The error bars are the standard deviation of the mean, obtained by averaging over multiple measurements.

Using the literature value, E_0=48.2 *GPa* for a similar alloy,[21] τ_m, c_m, E'_m and η'_m were calculated for each *m* by averaging over values obtained from the individual spectra, Fig. 4.5 (a) – (d). For *m*=4, only η is given, as determined from the linear part of the nanoindenter curve. It likely corresponds to an anelastic process with τ values that fall between the ranges covered by the two measurement methods. We observe c_m to range from <1% for the fastest sites to ~27% for the slowest: the total volume fraction occupied by *potential* STZs is a significant fraction of unity. In this context, we point out that we view c_m as the total volume of *potential* type-*m* STZs per unit volume, where overlapping volumes are counted multiple times. While our analysis is restricted to x_m<<1, i.e., a small volume fraction of the potential STZs are activated, c_m values greater than 1 are meaningful: the contribution of two *potential* STZs that have a finite spatial intersection to the probability of STZ formation is proportional to the sum of their volumes as long as their activation is rare. c_m >1 merely implies that the anelastic strain is greater than the elastic strain [Eqn. (4.5)]. For the present experimental conditions, at any point in time, the majority of potential STZs are not activated and are part of the elastic matrix. Thus, a high c_m value does not affect E_0 in Fig. 4.4 if x_m << 1. It should be noted that while c_m may continue to increase with increasing *m*, STZs with high *m* will be kinetically frozen below the glass transition temperature [Eqn. (4.7)].

After an anelastic site type with time constant τ is activated at fixed stress for a duration $t_0 << \tau$, the stress-free strain relaxation rate is smaller than that under stress by a factor of t_0/τ. Therefore, anelastic strains may last significantly longer than the duration of the prior stress that caused them, a fact that is often missed. This is the case for *m* = 8 in the present work. The reader is reminded that the present value of c_8 is determined by extrapolation to account for the fact that equilibrium is not reached for *m*=8 during the constraining period. The extrapolation introduces added error, which will be reduced in our ongoing work.

We proceed to determine the STZ volume values. Previous derivations of the shear strain rate were based on one dominant STZ type.[3,6,7] Since our experiments resolve different STZ types, we follow those derivations to express the contribution to the total shear strain rate due to STZs of type *m*:

$$\dot{\gamma}_m = 2c_m \gamma_0^c \nu_G \exp\left(-\frac{\Delta F_m}{kT}\right)\sinh\left(\frac{\sigma_s \gamma_0^T \Omega_m}{2k}\right), \tag{4.6}$$

where Ω_m is the STZ volume and $\gamma_0^c = \frac{2(4-5\nu)}{15(1-\nu)}\gamma_0^T$ is the transformation strain of an STZ that is constrained by the elastic matrix. ν is Poisson's ratio, ν_G, the attempt frequency, and k*T* has its usual meaning. The free energy of transformation of an *m*-type STZ is:

$$\Delta F_m = \left[\left(\frac{(7-5\nu)}{30(1-\nu)} + \frac{2(1+\nu)}{9(1-\nu)}\bar{\beta}^2\right)\gamma_0^T + \frac{1}{2}\frac{\bar{\sigma}_{STZ}}{\mu}\right]\mu\gamma_0^T\Omega_m, \tag{4.7}$$

where $\bar{\beta}^2$ ~1 the dilatancy factor, $\mu = E_0/[2(1+\nu)]$, the shear modulus and $\bar{\sigma}_{STZ}$ the shear resistance of the STZ. The division of the mechanical work term in Eqn. (4.6) by two reflects the assumption that the mechanical energy is a linear function of strain between the two STZ configurations[3] – there are other models that also satisfy detailed balance. The other factor of two, absent in Refs. 6 and 7, originates from the subtraction of forward- and backward flux and the definition of the sinh function. The following values were assumed for all STZ sizes: $\nu_G = 10^{13}$ s^{-1}, ν=0.35, $\bar{\sigma}_S/\mu$ = 0.025 (Ref. 30) and $\gamma_0^T = 0.2$. In Ref. 7, γ_0^T values range from 0.1 to 0.135, with a different mechanical work term. Colloid experiments yield ~0.3.[15, 31] It is noted that the empirical definition of the activation volume, $V^{*} = kTd\ln\dot{\gamma}/d\sigma$, equals $\frac{\gamma_0^T\Omega}{2}$ only if $\frac{\sigma_s\gamma_0^T\Omega}{2kT} >> 1$. Caution should be exercised when assigning a physical meaning to V* in other regimes. Using Eqn. (4.6), linearized for small σ_S, and Eqns. (4.4) and (4.7), Ω_m is obtained. Its value, normalized by the atomic volume of Al, is displayed in Fig. 4.5 (e). A hierarchy of Ω_m values is observed, ranging from ~ 14 to ~ 21, in *single-atomic increments*.

Ω_m is insensitive to error in η_m' since it appears in the exponent. It is, obviously, dependent on the assumed value of γ_0^T. Despite the uncertainty in the latter, the magnitude of the Ω spacings strongly suggests that the peaks in the relaxation spectrum correspond to a quantized hierarchy of STZs with *single-atomic increments*. Since the local chemistry and structure in an amorphous solid are expected to have a wide distribution, the clear separation of the processes may be surprising. Based on detailed studies of two dimensional bubble-rafts, Argon[6,9] argued that the spectrum of activation energies reflects the expected free-volume distribution: a large volume fraction occupied by sites with small free volume, and therefore a high activation barrier, and vice versa. In light of our present experiments, it appears that the spectrum of activation energies, calculated from Eqn. (4.7) and displayed in Fig. 4.5 (f), reflects the discrete STZ sizes and not the free-volume distribution. Spatial fluctuations in the composition, density and elastic constants are averaged over a volume that includes the surrounding matrix, and are apparently insufficient to obscure the effect of discrete STZ volumes. This argument is consistent with the fact that the third term in Eqn. (4.7), the work required to shear the atomic planes in an STZ, is insignificant,[7] and with MD simulations[16] that show a well-defined composition, and narrow distribution of the volume per atom, in activated STZs. We suggest that the local state of structural relaxation, i.e., the distribution of free volume or stress fluctuations, affects the flow behavior as an on/off switch via c_m. Our ongoing work is expected to lead to further analysis of this issue.

Our analysis implies that STZs that are larger or smaller than those detected should be active for the appropriate temperature and time scale. While extrapolation suggests that smaller STZs make up a small volume fraction, it also suggests steeply increasing volume fractions occupied by STZs with increasing m. Previous publications have all reported single, average, STZ sizes. Because of the steep increase of c_m with m (Fig. 4.5 (b)), it is expected that the contribution of the largest active STZs will dominate the macroscopic strain. Based on Eqn. (4.6), it follows that the observed average STZ size will increase with increasing temperature. In the present work, the volumes of the different STZs that contribute to the observed relaxation range from 14 to 21 atomic volumes of Al, in single-atom increments, as compared with 53 atomic volumes for the slowest, and therefore largest, active STZs determined for $Pd_{80}Si_{20}$ at elevated temperature.[7] Considering our uncertainty in γ_0^T, these results are not inconsistent with the present work. Pan *et al.*,[32,33] using strain–rate sensitivity measurements by nanoindentation, reported STZ sizes as high as >680 atoms. However, such measurements involve strain localization and shear band formation. The deforming volume fraction increases with increasing strain rate,[34,35] which leads to an underestimate of the microscopic strain rate sensitivity. In addition, the state of relaxation affects pileup[19] and therefore the indenter contact area. Therefore, we do not consider the high Ω values in Refs. 32 and 33 to be realistic. MD results show STZs consisting of 2 to 10 atoms[16] and tens to hundreds of atoms, increasing with strain.[17] Such simulations are conducted at higher stress and strain than the present experiment, and caution should be exercised when using them for comparison, as they are likely to be affected by interaction among STZs. It should also be noted that thermally activated shear of STZs well below the glass transition temperature is a rare event, which cannot be modeled realistically by MD.

Dmowski *et al.*[12] have recently concluded from measured anisotropic atomic pair distribution functions that 1/4 of the volume of a Zr-based metallic glass deforms anelastically with short time constants, contributing to the apparent elastic behavior on typical experimental time scales. If we extrapolate our c_m values to smaller m, and therefore shorter τ, we obtain very small volume fractions. This discrepancy is even greater than it appears, because the alloy of Ref. 12 has a higher glass transition temperature than the present alloy and its STZs should be more sluggish at room temperature at a comparable size. We suggest that the anelastic sites reported to occupy 1/4 of the volume are of a different nature than the STZs that are active at high temperature, even though their effect on the pair distribution function is similar. Activity of these sites is possibly described by a bond-exhange[10] mechanism. Recent dynamic measurements in several metallic glasses are consistent with this picture, showing a nonzero loss modulus at cryogenic temperatures, which is separate from the broad high-temperature peak.[36]

Our Ω values are consistent with the assumption of Newtonian viscosity – for the highest stress values used, linearization of the sinh term in Eqn. (4.6) results in an error of 6.5 to 9% for Ω_5 to Ω_8, and orders of magnitude less for the cantilever experiment. As in Ref. 15, STZ activation is thermal, with the stress bias resulting in an initial ratio of forward-to-backward jump rates of ~1.03 for the cantilever and 3.4-4.3 for the mandrel experiment. As seen in Fig. 4.5 (f), $\Delta F_m / kT$ ranges from about 33 to 50. $0.85 < \Delta F_m < 1.26$ eV/atom, compared with a vacancy migration energy in crystalline Al, $\Delta H = 0.62\ eV$.[37] The present experiment is conceptually related to the measurement of the activation-energy distribution by temperature stepping,[14] but it does not suffer from resolution limitations due to thermal equilibration times. Reference 14 yields $0.87 < \Delta F < 2.18$ *eV*/atom for alloys with shear moduli in a range above twice that of the present alloy, which represents good agreement. It is important to note that our Ω values are dependent on the assumed value of γ_0^T – using 0.3 would reduce Ω by a factor greater than two, whereas $\gamma_0^T = 0.1$ would increase it by a factor of approximately four. Our assumption of size-independent γ_0^T is unlikely to significantly affect our conclusions.

Anelastic relaxation spectra with distinct peaks have been observed for other metallic glass alloys,[38–41] indicating that our results are far from unique to the present alloy. In addition to the quantitative information we obtain, a novel aspect of the present work is the wide range of accessible time constants, which has allowed us to observe an unprecedented number of distinct processes. Few experiments, and no MD simulation, can access such a wide dynamic range. It may be surprising that no distinct anelastic processes were observed in any of the large number of dynamic internal-friction studies[42-46] performed in metallic glasses over the years, since these are capable of exploring a wide dynamic range of time constants. Two factors obscure spectrum details in dynamic measurements, and are the likely cause: a) The resonance curve in dynamic internal friction measurements has a Cauchy frequency dependence, which leads to significant overlap among different processes even if they have low intrinsic width and differ from each other by a factor of 10. In contrast, and unlike most instrumented methods, the curvature measurements we conduct provide high resolution and stability over long time periods. Furthermore, b) dynamic measurements require high frequencies and therefore elevated temperatures. Since the time constant for a relaxation process is proportional to exp($\Delta F/\mathrm{k}T$), a higher temperature will reduce the dynamic range of time constants and thus the resolution. We conclude that while our experimental approach is time consuming, it has been crucial to our discovery of the quantized hierarchy of STZs. Finally, we point out the difference between our regime of low strain and that of a highly driven flow state, for which simulations[47] yield a broad and continuous distribution of activation energies.

In summary, quasi-static measurements of anelastic relaxation in $Al_{86.8}Ni_{3.7}Y_{9.5}$ have yielded a range of STZ properties. A quantized hierarchy of STZs is revealed, with increments of a single atomic volume. The volume fraction occupied by *potential* STZs is obtained directly, and shown to be a large fraction of unity. While only a small fraction of the STZs is activated at any time for the low strains used, thermal fluctuations cause all potential STZs to probe their ergodic space and therefore have the same time-averaged strain. Future work will address activation of slower processes, dynamic measurements of possible anelastic processes that appear as elastic at our time resolution, the temperature dependence of anelastic relaxation and the effect of structural relaxation.

ACKNOWLEDGEMENTS

This work was funded by the US National Science Foundation (NSF), Grant DMR-0605911. The authors are grateful to Prof. F. Spaepen for useful discussions and reading of this manuscript, and T. Egami for useful discussions. They also thank Dr. F. Pinkerton of General Motors R&D Center for preparing the sample used in this work, and Prof. J. Greer for the use of the nanoindenter in her laboratory.

APPENDIX: DERIVATION OF THE VOLUME FRACTION OCCUPIED BY POTENTIAL STZS

The connection between the linear solid model (Fig. 4.4), with a continuum strain states, and STZs, which are modeled as having discrete strain states, is developed here. As illustrated in Fig. 4.6, Voigt unit *m* in Fig. 4.4 is modeled as a large number of Voigt units in series, each representing the additive contribution of one *m*-type STZ to the strain. The macroscopic shear strain due to *m*-type STZs is proportional to the fraction, x_m, of *potential* *m*-type STZs that are activated, and is therefore given by $\gamma_m = c_m x_m \gamma_0^c$. γ_0^c is the transformation strain of an STZ that is constrained by the elastic matrix. The macroscopic bending strain corresponding to γ_m is

$$\varepsilon_m^0 = (1-\nu) c_m x_m^0 \gamma_0^c, \tag{4.8}$$

where ν is Poisson's ratio.

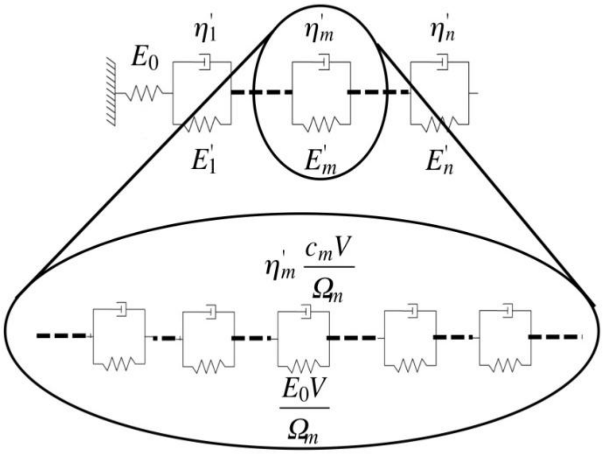

Figure 4.6 The linear model used for individual *m*-type STZs**.** Voigt unit *m* in Fig. 4.4 consists of many Voigt units, each representing a single STZ, in series. The effective viscosity and effective Young's modulus of each STZ is inversely proportional to the volume fraction it occupies. *V* is the volume of the solid.

$x_m\gamma_0^c$ is the *ensemble*-averaged shear strain of *all potential* STZs. Since the STZs are ergodic (see text and Ref. 15), $x_m\gamma_0^c$ is also equal to the *time*-averaged shear strain of each *potential* STZ. In this interpretation, all STZs participate in the deformation process and have a continuum of possible time-averaged strain values that evolve under a macroscopic applied stress. When an STZ is not in an activated state, it is part of the elastic matrix. Since the elastic constant that governs STZ reversal is the same as that of the matrix, the time-averaged equilibrium strain of each STZ in the bending direction, $(1-\nu)x_m^0\gamma_0^c$, is equal to ε_{el}^0, where x_m^0 is the value of x_m at mechanical equilibrium. Applying Eqn. (4.8) at mechanical equilibrium, $\varepsilon_m^0 = (1-\nu)\,c_m\,x_m^0\,\gamma_0^c$, in combination with Eqn. (4.3), the condition for mechanical equilibrium, one obtains

$$c_m = \frac{\varepsilon_m^0}{\varepsilon_{el}^0} = \frac{E_0}{E_m^{'}}\,. \tag{4.9}$$

As discussed in the text, c_m can be understood as the total STZ volume per unit volume, with STZ intersections counted multiple times.

4.2 ADDITIONAL DETAILS AND FURTHER MEASUREMENTS

The STZ properties presented in Section 4.1 were characterized by anelastic strain relaxation experiments measured in a stress-free state up to a duration (t_{sf}) of ~ 3 × 10^7 *sec.* The strain normalized by the equilibrium elastic strain ($\varepsilon_{anel}/\varepsilon_{el}^0$) at t_{sf} was ~ 0.015, which corresponded to ~7 – 8 % of the initial value at t = 0, $(\varepsilon_{anel}/\varepsilon_{el}^0)_{t=0}$ = ~ 0.18. The measurements were continued for longer time to re-evaluate the previous results, presented in Section 4.1, with improved data. The improved data also allowed us to better determine the reversible portion of the time-dependent strain. In this section, the results obtained for t_{sf} = ~ 8 × 10^7 *sec.* are compared with earlier results for t_{sf} = ~ 3 × 10^7 *sec.*

The time-dependent strain in as-quenched samples constrained for t_c = ~ 2 × 10^6 *sec.* was recovered within 1% after t_{sf} = ~ 8 × 10^7 *sec.* in a stress-free state. These results confirm our assumption that the time-dependent strain is indeed anelastic. The experimental data were analyzed following the procedure of Section 4.1 to yield STZ volumes (Ω_n) and volume fraction of potential STZs (c_n).

When calculating $c_{n=21}$ in Section 4.1 and here, an extrapolation method was used to account for the fact that STZs consisting of 21 atoms do not equilibrate with the elastic strain within t_c. For example, for a standard linear solid (See Fig. 2.2), during stress-relaxation, i.e., under constant applied strain, ε_{appl}, a solution for anelastic strain, $\varepsilon_{anel}(t_c)$, to Eqn. (2.4) is given by:

$$\varepsilon_{anel}(t_c) = \varepsilon_{appl} \frac{E_0}{E_0 + E_1} \left(1 - \exp\left[-\frac{t_c}{\tau_c} \right] \right), \tag{4.10}$$

where E_0, E_1 and η_1 corresponds to the Young's modulus, effective modulus ($E_n^{'}$) and effective viscosity ($\eta_n^{'}$) of an n-type Voigt unit, respectively, and τ_c, the time constant for anelastic strain relaxation under fixed-strain constraint, is given by:

$$\tau_c = \frac{3\eta_1}{E_0 + E_1} \,. \tag{4.11}$$

At longer constraining times, the anelastic strain approaches its equilibrium value, $\varepsilon_{eq,an} = \varepsilon_{appl} \times E_1/(E_0+E_1)$.

$\tau_{n=21}$ obtained in a stress-free state is greater than the other $\tau_{n<21}$ by at least an order of magnitude, and therefore, it is reasonable to assume that the processes corresponding to $\tau_{n<21}$ equilibrate under constraint. According to this assumption, the Voigt units for these processes, employed in Section 4.1, can be approximated by the equilibrated spring units in series, as shown in Fig. 4.7.

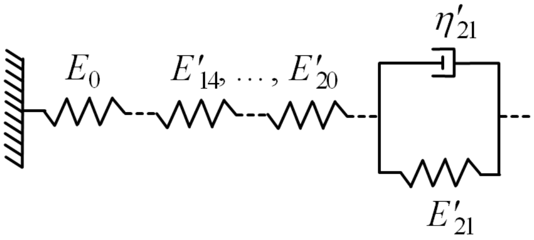

Figure 4.7 Modified Voigt units in series, employed in Section 4.1, assuming that the processes corresponding to $\tau_{n<21}$ are equilibrated under constraint.

In the calculation of the evolution of Voigt unit for n = 21 under constraint, this is accomplished by replacing E_0 in Eqn. (4.10) and (4.11) by:

$$E_0^{'} = \left((E_0)^{-1} + \sum_{n=14}^{20} (E_n^{'})^{-1} \right)^{-1}, \tag{4.12}$$

with E_1 and η_1 in Eqn. (4.10) replaced by $E_{21}^{'}$ and $\eta_{21}^{'}$, respectively. (1-exp[-$t_c/\tau_{c,n=21}$]) is a fractional equilibration factor needed to correct $E_{21}^{'}$ and $\eta_{21}^{'}$ for incomplete equilibration under constraint for t_c. The incomplete equilibration leads to a reduction of $\varepsilon_{n=21}^{0}$ by this factor, since $t_c < \tau_{c,n=21}$: $E_0\, \varepsilon_{el}^{0} = E_n^{'}\, (1 - \exp[-t_c / \tau_{c,n=21}]\varepsilon_n^{0}$. Therefore, $E_{21}^{'}$ and $\eta_{21}^{'}$ values obtained from the relaxation-time spectra are multiplied by (1-exp[-$t_c/\tau_{c,n=21}$]) for the correction. These newly determined E'_{21} and η'_{21}, however, result in a change in $\tau_{c,n=21}$. Therefore, the calculations are iterated until $\tau_{c,n=21}$, E'_{21} and η'_{21} converge, with further change being less 0.01 % in E'_{21} and η'_{21}, and consequently $c_{n=21}$.

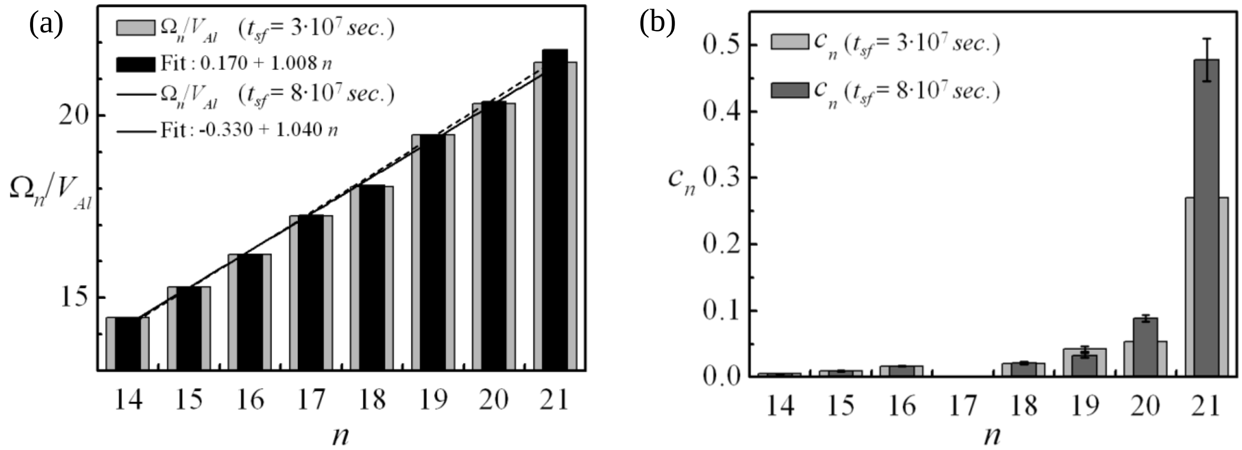

Figure 4.8 (a) Ω_n normalized by Al atomic volume, V_{Al}, obtained in anelastic strain measured up to t_{sf} = ~ 3 × 10^7 (light gray box) and ~ 8 × 10^7 *sec.* (dark gray box) after t_c = ~ 2 × 10^6 *sec.* (n = 18 – 21). The cantilever results (n = 14 – 16) and an interpolation (n = 17) are reproduced from Section 4.1. Linear fits of Ω_n obtained in each measurement show negligible difference. (b) c_n as a function of n, obtained in different t_{sf}, showing relatively large difference in their magnitudes, especially for high n.

Ω_n normalized by Al atomic volume, V_{Al}, obtained for anelastic strain measured up to t_{sf} = ~ 8 × 10^7 *sec.* are plotted in Fig. 4.8 (a). Previous values obtained for t_{sf} = ~ 3 × 10^7 *sec.* in Section 4.1 are shown for comparison. The main difference is a slightly larger value (~ 1.6 %) of

($\Omega_{n=21}/V_{Al}$) than that in the previous results. The resulting increase in the slope in the linear fit, however, is only ~ 3 %, confirming our previous conclusion on the atomically quantized hierarchy of STZs, ranging from 14 to 21.

c_n obtained in the current measurements are plotted as a function of n in Fig. 4.8 (b). While Ω_n show little difference compared to those obtained in shorter t_{sf}, c_n show relatively large difference in their magnitudes, especially for high n, i.e., for large τ_n. $\tau_{n=21}$ currently obtained for t_{sf} = ~ 8 × 10^7 *sec.* is greater than that obtained for t_{sf} = ~ 3 × 10^7 *sec.* by about factor of two. As a result, η'_{21} is also ~ twice that of the previously obtained η'_{21}, leading to a high $\tau_{c,n=21}$. Since t_c is the same (t_c = ~ 2 × 10^6 *sec.*) for both data, ($1-\exp[-t_c/\tau_{c,n=21}]$) is smaller than that for the previous results, leading to decrease in E'_{21}, and consequently, increase in $c_{n=21}$, shown in Fig. 4.8 (b).

In summary, improved bend-stress relaxation data continued for longer time (t_{sf} = ~ 3 × 10^7 *sec.*) have revealed that the time-dependent strain developed for t_c = ~ 2 × 10^6 *sec.* for different ε_{el}^0 values, ranging from 0.16 – 0.30 %, is anelastic. DSA, performed using these anelastic strains, yield relaxation-time spectra, which allow us to obtain c_n and Ω_n. Current Ω_n values are consistent with those obtained in Section 4.1. Correction made for $c_{n=21}$ due to its large $\tau_{n=21}$ compared to t_c, however, leads to the increase in them. While $c_{n=21}$ show a large increase compared to the previous results presented in Section 4.1, its trend, increasing as a function of n, is unchanged. This trend is discussed with a microscopic model in Section 4.4 in detail. Our ongoing works performed with increased t_c may allow for elucidating c_n corresponding to large τ_n due to the uncertainty of the extrapolation method.

4.3 STRUCTURAL RELAXATION

Anelastic properties of an as-quenched metallic glass measured in the quasi-static relaxation experiments are analyzed in terms of STZs in Section 4.1. An important parameter involved in understanding the mechanical properties is the state variable that describes a metallic glass system and accounts for changes in properties, e.g., shear viscosity[48] or diffusivity,[49] upon annealing due to the structural relaxation. While the STZ model[6,7,8] is useful in quantitatively understanding the macroscopic strain resulting from STZs, the model per se does not account for these property changes.

The free volume model, developed by Cohen and Turnbull,[50] has been widely used to analyze the structural relaxation (See Section 2.2.2). Especially, Spaepen and his coworkers' analyses[48,3,51] of the shear viscosity rise during structural relaxation, on the basis of an extension of the free volume model, have been successful in terms of correlating the free volume decrease (density increase) to the viscosity increase. The total probability of the local free volume exceeding a critical value, v^*, given in Eqn. (1.1): $\int_{v^*}^{\infty} \frac{\gamma}{v_f} \exp\left(-\frac{\gamma v}{v_f} \right) dv = \exp\left(-\frac{\gamma v^*}{v_f} \right)$, decreases with decreasing average free volume, which explains the viscosity increase.[48,3,51] It should be noted, however, that these analyses are based on the assumption that the basic process accommodating deformation consists of single atomic jumps.

While prior experimental studies[52,53] of dynamic properties of metallic glasses have suggested that structural relaxation leads to the annihilation of the sites that may undergo shear transformations, a quantitative description of what causes the annihilation and how it affects STZs has not been given. In order to rationalize the effect of structural relaxation on mechanical properties of metallic glasses in terms of STZs, therefore, it is crucial to address these questions. Specifically, the size-dependent activation energy barrier and volume fraction of potential STZs

(c_n) need to be examined, where n is the number of atoms comprising an n-size STZ. For c_n, it is critical to define what allows for an atomic cluster to be a potential STZ in order to account for the relation between STZs and free volume. [3,48,50,51]

Our analysis of anelastic properties of an as-quenched metallic glass has allowed for directly obtaining Ω_n and c_n from the anelastic relaxation experimental data. In order to compare these properties with those in structurally relaxed metallic glasses, the same measurement techniques were employed to characterize the anelastic strain of samples annealed for 1 *hr*. at 110 ^oC. Their amorphous structure was confirmed using a high resolution transmission electron microscopy after the heat treatment (See Chapter 3). While the results in Section 4.2 show that for $t_c = \sim 2 \times 10^6$ *sec*. there is an uncertainty in $c_{n=21}$, we include this value in the analysis because it was obtained for both as-quenched and relaxed samples under the same conditions.

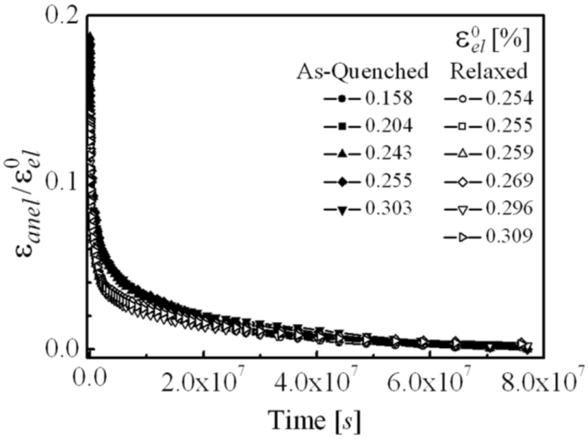

Figure 4.9 Anelastic strain (ε_{anel}) of as-quenched (solid symbols) and relaxed (open symbols) samples for $t_c = \sim 2 \times 10^6$ *sec*., normalized by the elastic bending strain at mechanical equilibrium, ε_{el}^0, characterized in bend-stress relaxation measurements up to $t_{sf} = \sim 8 \times 10^7$ *sec*. ε_{el}^0 is varied using different mandrel radii.

The anelastic strain of as-quenched and relaxed samples, normalized by the equilibrium elastic strain, ε_{el}^{0}, for bend-stress relaxation measurements is plotted as a function of time, t, measured up to t_{sf} = ~ 8 × 10^7 *sec*. (~ 2.4 *yr*.) after t_c = ~ 2 × 10^6 *sec*. in Fig. 4.9. The normalized anelastic strain of relaxed samples at t_{sf} is of the order of ~ 2 × 10^{-3}, which corresponds to ~ 1 – 2 % of the value at t = 0, indicating that most of the STZs formed under constraint are fully reversed during this period of time. For both sample types, linearity of anelastic strain in ε_{el}^{0} is observed from the overlap of the normalized curves in Fig. 4.9.

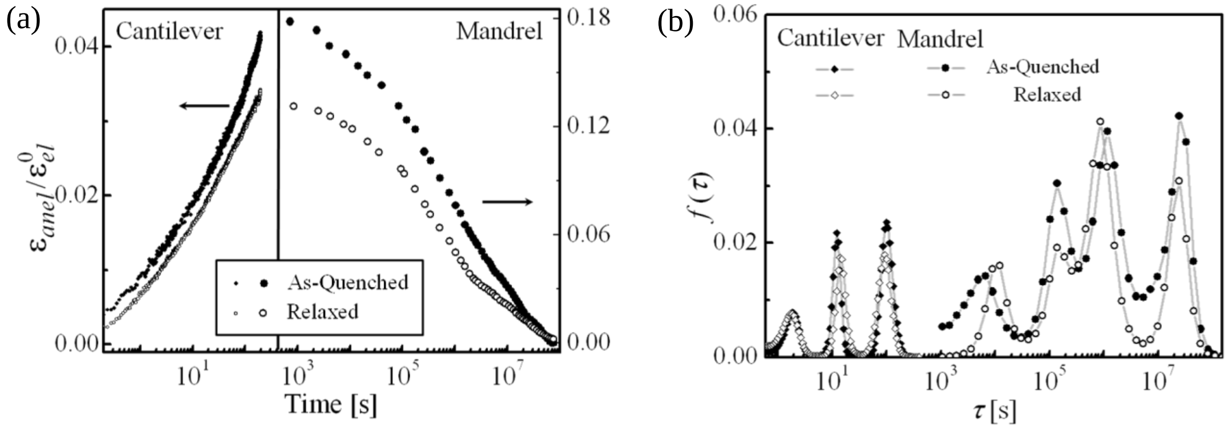

Figure 4.10 (a) Representative anelastic strain curves of as-quenched (solid symbols) and relaxed (open symbols) samples measured as a function of time in cantilever bending and bend-stress relaxation experiments for t_c = ~ 2 × 10^6 *sec*. and t_{sf} = ~ 8 × 10^7 *sec*. (b) Corresponding relaxation-time spectra determined from each data set shown in (a), employing DSA.[24]

The relaxation-time spectra, $f(\tau)$, were determined from the anelastic strain data, employing DSA. As an example, sample data sets for as-quenched and relaxed samples obtained in cantilever bending and bend-stress relaxation measurements are shown in Fig. 4.10 (a). Each data set was fitted with Eqn. (3.11), ensuring that the number of variables did not exceed that of experimental data, and $f(\tau)$ was obtained using Eqn. (3.13) (See Chapter 3 for details). $f(\tau)$ obtained from the experimental data in Fig. 4.10 (a) is shown in Fig. 4.10 (b). Distinct peaks in $f(\tau)$ are not unique to the as-quenched samples, but also observed for the relaxed samples, confirming that distinct processes are involved in the anelastic relaxation.

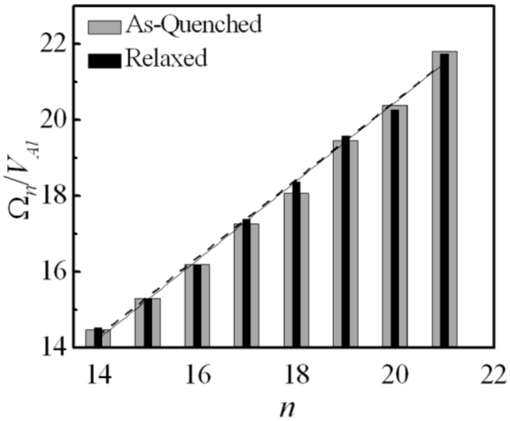

Figure 4.11 Volume of STZs, Ω_n, normalized by Al atomic volume, V_{Al}, as a function of n. t_c = ~ 2 × 10^6 *sec*. and t_{sf} = ~ 8 × 10^7 *sec* in both as-quenched and relaxed samples. for the bend-stress relaxation measurements (n = 18 – 21). The cantilever results (n = 14 – 16) and an interpolation (n = 17) are reproduced from Section 4.1. The lowest index, n = 14, was selected to correspond to the ordinate value, thus designating the number of atoms. Error propagation yields less than 0.3 % random error in all Ω_n values. Linear fits of the plots yield a slope of 1.040 and 1.030 for as-quenched and relaxed samples, respectively.

The distinct peaks in $f(\tau)$ enable us to compute Ω_n for each anelastic process, by following the same procedures as for as-quenched samples in Section 4.1. Ω_n in both as-quenched and relaxed samples, normalized by V_{Al}, as a function of n is shown in Fig. 4.11. Linear fits of the plots yield a slope of 1.0397 and 1.0301 for as-quenched and relaxed samples, respectively, indicating agreement within less than 1%. These nearly identical fits shown in Fig. 4.11 suggest that the change in Ω_n due to the structural relaxation is insignificant, providing strong confirmation of our earlier conclusion on the atomically quantized hierarchy of STZs.

Argon and Kuo[6,8] argued that the activation energy spectra that they obtained by the temperature stepping method resemble mirror images of the free volume distribution: a local site with large free volume has small activation energy for shear transformations, and the activation energy increases with decreasing free volume in the site.[6,8] According to their analysis, a decrease in free volume due to structural relaxation results in an increase in activation energy. Iso-configurational viscosities in creep experiments measured as a function of reciprocal temperature for different prior annealing temperatures, reported in Ref. 48, however, exhibit Arrhenius behavior with nearly the same slopes in a wide range of temperatures. Each slope represents the activation energy in the transition-state theory,[3,6] suggesting that the activation energy does not change when structural states of a metallic glass are changed by annealing. It is noted that according to Eqn. (2.21), the activation energy is proportional to the volume of STZs, i.e., Ω. Therefore, our observation on the same STZ volumes in as-quenched and structurally relaxed metallic glasses indicates that the activation energy remains unchanged upon structural relaxation, representing a size-resolved extension of prior experimental results.[48]

Our analyses of STZs in both as-quenched and structurally relaxed samples consistently yield the same sizes of $n = 14 – 21$, and we suggest that these are part of a wider hierarchy. The window of n values that we observe can be readily explained when one considers the values of τ_n and c_n. For example, $\tau_{n=14}$ = ~ 2 *sec.* and $c_{n=14}$ = ~ 5 × 10^{-3} for as-quenched samples. An extrapolation of τ_n and c_n based on Ω_n and Eqn. (4.13), respectively, yields $\tau_{n=13}$ = ~ 0.1 *sec.* and $c_{n=13}$ = ~ 10^{-4}. These values suggest that STZs smaller than n = 14 may not be characterized under the given experimental conditions: For example, in order to characterize the STZ size of n = 13, at least of the order of sub-10^{-2} seconds in time and sub-10^{-3} values of $\varepsilon_n^0 / \varepsilon_{el}^0$ should be accessible experimentally. In a similar fashion, the upper limit, n = 21, can be explained. For $n \geq$ 21, $\tau_n \geq$ ~ 10^8 *sec.*. Since both t_c and t_{sf} are significantly shorter, these large STZ sizes are not easily accessible. It is noted that the effect of STZs with n = 22 was observed (See Section 4.4).

Improving the experimental resolution, therefore, may allow for expanding the current window, exploring a wider range of Ω_n. This window may be varied by changing the temperature. For example, assuming Arrhenius behavior of $\tau(T)$, given in Eqn. (2.16): $\tau(T) = \tau_0 \, e^{\Delta E_a / kT}$, increasing the temperature substantially decreases the respective τ_n. Thus, measurements at elevated temperature may allow for characterizing large STZs that correspond to $\tau_{n>21}$, but small STZs may not be observed due to the substantial decrease in corresponding τ_n. On the other hand, lowering the temperature is suitable for characterizing STZs corresponding to $\tau_{n<14}$ but not large STZs. Performing experiments at higher and lower temperatures, therefore, will vary the window of the hierarchy to larger and smaller STZs, respectively.

c_n is calculated from $f(\tau)$ in Fig. 4.10 (b). As detailed in Section 4.1, it is determined by the mechanical equilibrium between the spring exhibiting instantaneous strain, represented by Young's modulus E_0 = 48.2 GPa[21] and elastic strain at mechanical equilibrium ε_{el}^0, and that in an n-type Voigt unit with effective modulus $E_n^{'}$ and the equilibrium anelastic strain ε_n^0. The mechanical equilibration between these two components allows us to obtain $c_n = \varepsilon_n^0 / \varepsilon_{el}^0 = E_0 / E_n^{'}$ from $f(\tau)$, where ε_n^0 is calculated by integrating the respective peak in $f(\tau)$ over τ: $\varepsilon_n^0 = \int_n f(\tau)\, d\ln\tau$.

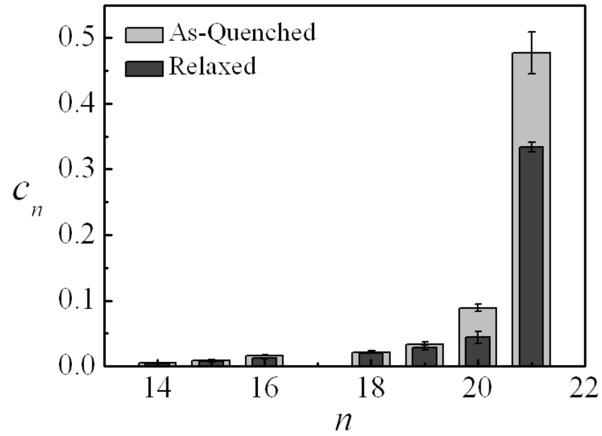

Figure 4.12 The volume fraction of potential STZs, c_n, as a function of the number of atoms in them, n, obtained in as-quenched (light gray box) and relaxed (dark gray box) samples. t_c = ~ 2 × 10^6 *sec*. and t_{sf} = ~ 8 × 10^7 *sec*. for bend-stress relaxation measurements.

c_n of both as-quenched and relaxed samples are shown as a function of n in Fig. 4.12. The error bars show the standard deviation of the mean, which is calculated from 95 and 70 cantilever, and 5 and 6 bend-stress relaxation measurements, for as-quenched and relaxed samples, respectively. It is observed that c_n is smaller for structurally relaxed samples for all n, and the fractional difference increases with increasing n.

Our current observation indicates that change in mechanical properties due to structural relaxation, e.g., viscosity rise upon annealing, results from the decrease in c_n, not from a change in volume of STZs, Ω, i.e., in activation energy (Eqn. 2.21). While structural relaxation does not change the activation energy for STZs, as Ω remains unchanged, the decrease in free volume anneals out potential STZs. A remaining challenge is to rationalize the size dependent distribution of c_n that accounts for their free volume dependence.

4.4 A MICROSCOPIC MODEL

4.4.1 A CRITERION FOR A POTENTIAL STZ

In order to determine c_n, a condition for an atomic cluster to be a potential STZ is postulated: if the total free volume shared by individual atoms in an atomic cluster of size n exceeds a critical set value, v^*, which is approximately independent of n, the cluster is capable of undergoing shear transformation, i.e., a potential STZ. According to this criterion, the total probability per atom of finding such clusters ($N_n(v^*)$) is given by:

$$N_n(v^*) = g(n) \int_{v_1+\ldots+v_n>v^*} dv_1 \ldots dv_n (\gamma / v_f)^n \exp\left[-(\gamma / v_f)(v_1 + \ldots + v_n)\right] = g(n)\left(\sum_{i=0}^{n-1} \frac{1}{i!}(\gamma v^* / v_f)^i\right)\exp\left(-\frac{\gamma v^*}{v_f}\right), \tag{4.13}$$

where $g(n)$ is the number of near-equiaxed clusters of n atoms. ($n \times N_n(v^*)$) is equal to the predicted c_n, which approaches ($n \times g(n)$) for large n.

Equation (4.13) was fitted to c_n in Fig. 4.12. It was assumed during the fitting that $g(n) = 5$ for all n, with $\gamma v^*/v_f$ being the only fitting parameter. Resulting fits for as-quenched and relaxed samples are plotted in Fig. 4.13. They yield the fitting parameter $\gamma v^*/v_f$ of 36.6 and 37.4 for as-quenched and relaxed samples, respectively, indicating a decrease in v_f upon structural relaxation of ~ 2 %. While the values of $\gamma v^*/v_f$ reported in Ref. 48 is about half the current value, the results cannot be directly compared, since the analysis of Ref. 48 is based on an assumption that a series of single atomic jumps accommodate deformation.

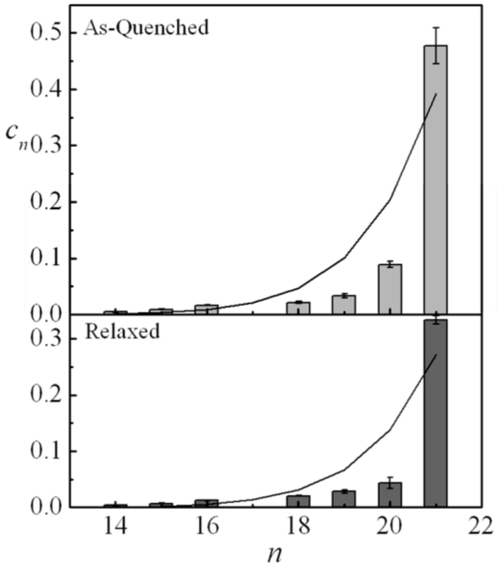

Figure 4.13 Fits (solid line) obtained using Eqn. (4.13), employing c_n data in Fig. 4.12. t_c = ~ 2 × 10^6 *sec*. and t_{sf} = ~ 8 × 10^7 *sec*. for bend-stress relaxation measurements.

Although the fits in Fig. 4.13 show deviation from the experimental data for large *n*, especially for $c_{n=21}$, these fits follow the trends of c_n in terms of Poisson statistics, increasing as a function of *n*. $c_{n=21}$ for as-quenched samples is ~ 0.48 but the predicted value using Eqn. (4.13) is ~ 0.21, and the discrepancy may originate from the uncertainty of extrapolation made to account for shorter constraining time (t_c = ~ 2 × 10^6*sec*.) compared to τ_{21} (~ 2.7 × 10^7*sec*.). It is interesting to note that when the same analysis was performed with as-quenched samples that were constrained for t_c = ~ 4.4 × 10^8 *sec*., the obtained $c_{n=21}$ was 0.13, indicating an error in extrapolation for $c_{n=21}$ for the shorter t_c.

4.4.2 EXPERIMENTAL OBSERVATIONS AND SUMMARY

While the atomically quantized hierarchy of STZs, and a model of its free volume dependence have not been reported before, experimental studies of dynamic properties of metallic glasses[52,54,55] can be compared with the present results. Especially, it will now be shown that loss moduli for different alloys measured as a function of T at fixed ω, or as a function of ω at fixed T, showing noticeable asymmetry in their spectrum (See Section 2.2.3) are consistent with our results. Analyses of the loss moduli in terms of relaxation-time spectra are discussed in detail in Chapter 5.

Since the activation energy for n-size STZs can be calculated using Eqn. (2.21), and therefore, also the respective time constants, τ_n, the loss modulus can be calculated, employing these values, using Eqn. (3.16). For example, for an arbitrarily chosen fixed frequency value of 1 *Hz*, the loss modulus spectrum as a function of T is shown in Fig. 4.14, based on our c_n values with interpolated $c_{n=17}$ for an as-quenched sample. The calculated loss modulus clearly shows a low-temperature tail, which has been observed in many other metallic glasses.[45,54,55] The tail is due to the c_n spectrum, with significant overlap among individual Cauchy peaks. It is expected that height of the loss modulus spectrum will decrease upon relaxation, as seen in tan(δ) in Ref. 52 and 56. The present author, however, was unable to find corresponding experimental results on the loss modulus in the literature, for comparison. In Ref. 57, it was reported for loss moduli, normalized by their apparent peak value, that the temperature ranges, in which the loss moduli of as-quenched and relaxed samples were observed, were the same. The temperature range is a function of activation energy: with increasing the activation energy, the loss modulus peak is observed in the higher temperature regime. Therefore, Ref. 57 provides another confirmation of our conclusion, along with the prior experimental results in Ref. 48, that the activation energies are not changed by structural relaxation.

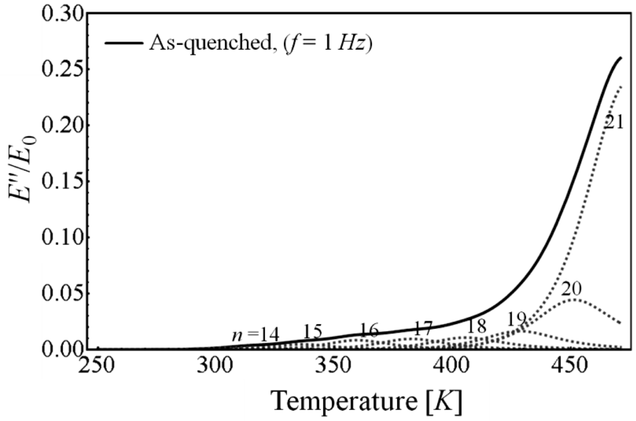

Figure 4.14 Calculated loss modulus (E'') as a function of temperature (T) at fixed frequency value of 1 *Hz*, normalized by Young's modulus (E_0) using Eqn. (2.19), based on the present quasi-static c_n data for an as-quenched sample (Section 4.1 and Fig. 4.12) with $c_{n=17}$ obtained by interpolation. The loss modulus peak resulting from each c_n is shown with a dotted line. The graph is only computed up to 470 *K* because the model used is not expected to be valid above T_g.

In summary, our results suggest that while the volume of STZs and their quantized hierarchy show less than one percent change upon structural relaxation, c_n decreases substantially. Fits to the size dependent c_n using Eqn. (4.13) yield a ~ 2 % change in average free volume, v_f, due to the structural relaxation compared to the as-quenched state. In addition, Eqn. (4.13) accounts for the increase in c_n with n in terms of the Poisson statistics, which is consistent with the observed shape of the dynamic loss modulus spectra.[45,52,54,55,57] Note that the activation energy barriers for STZs are proportional to n, as given in Eqn. (2.21). Therefore, although high-*n* potential STZs may occupy a high volume fraction, they may be kinetically frozen at temperatures below T_g due to the large activation barrier.

4.5 REFERENCES

4.1 J. D. Ju, D. Jang, A. Nwangkpa and M. Atzmon, *J. Appl. Phys.* **109**, 053522 (2011).

4.2 A. Inoue, B. Shen, and A. Takeuchi, *Mater. Sci. Forum* **539-543**, 92 (2007).

4.3 F. Spaepen, *Acta Metall*. **25**, 407 (1977).

4.4 C. A. Schuh, T. Hufnagel and U. Ramamurty, *Acta Mater.* **55**, 4067 (2007).

4.5 M. M. Trexler and N. N. Thadhani, *Prog. Mater. Sci.* **55**, 759 (2010).

4.6 A. S. Argon, *Acta Metall*. **27**, 47 (1979).

4.7 A. S. Argon and L. T. Shi, *Acta Metall*. **31**, 499 (1983).

4.8 A. S. Argon and H. Y. Kuo, *Mater. Sci. Eng.* **39**, 101 (1979).

4.9 A. S. Argon and L. T. Shi, *Phil. Mag. A* **46**, 275 (1982).

4.10 Y. Suzuki and T. Egami, *J. Non-Cryst. Sol*. **75**, 361 (1985).

4.11 J. C. Ye, J. Lu, C. T. Liu, Q. Wang and Y. Yang, *Nature Mater*. **9**, 619 (2010).

4.12 W. Dmowski, T. Iwashita, C. P. Chuang, J. Almer and T. Egami, *Phys. Rev. Lett.* **105**, 205502 (2010).

4.13 T. Egami, W. Dmowski, P. Kosmetatos, M. Boord, T. Tomida, E. Oikawa and A. Inoue, *J. Non-Cryst. Sol*. **192-193**, 591 (1995).

4.14 A. S. Argon and H. Y. Kuo, *J. Non-Cryst. Sol*. **37**, 241 (1980).

4.15 P. Schall, D. A. Weitz, D. A. and F. Spaepen, *Science* **318**, 1895 (2007).

4.16 F. Delogu, *Phys. Rev. Lett*. **100**, 255901 (2008).

4.17 M. Neudecker and S. G. Mayr, *Acta Mater*. **57**, 1437 (2009).

4.18 W. H. Jiang and M. Atzmon, *J. Mater. Res.* **20**, 696 (2005).

4.19 W. H. Jiang, F. E. Pinkerton and M. Atzmon, *Acta Mater.* **53**, 3469 (2005).

4.20 T. P. Weihs, S. Hong, J. C. Bravman and W. D. Nix, *J. Mater. Res.* **3**, 931 (1988).

4.21 J. M. Freitag, R. G. Koknaev, R. Sabet-Sarghi, M. Koknaeva and Z. Altounian, *J. Appl. Phys*. **79**, 3967 (1996).

4.22 J. Haimovich and T. Egami, *Mater. Sci. Eng.* **61**, 89 (1983).

4.23 C. Bernard, G. Delaizir, J.-C. Sangleboeuf, V. Keryvin, P. Lucas, B. Bureau, X.-H. Zhang and T. Rouxel, *J. Europ. Cer. Soc*. **27**, 3253 (2007).

4.24 J. R. Cost, *J. Appl. Phys*. **54**, 2137 (1983).

4.25 R. Fourer, D. M. Gay and B. W. Kernighan, *AMPL: A Modeling Language for Mathematical Programming*, Scientific Press, South San Francisco, CA (1993).

4.26 A. Wächter and L. T. Biegler, *Mathematical Programming* **106(1)**, 25 (2006).

4.27 R. Kohlrausch, *Ann. Phys. Leipzig* **91**, 56 (1854).

4.28 A. S. Nowick and B. S. Berry, *Anelastic Relaxation in Crystalline solids*, Academic, New York, (1972).

4.29 R. S. Lakes, *Viscoelastic Solids*, CRC Press, Boca Baton, FL (1999).

4.30 H. Kato, H. Igarashi and A. Inoue, *Mater. Lett*. **62**, 1592 (2008).

4.31 F. Spaepen, private communication.

[4.32] D. Pan, A. Inoue, T. Sakurai and M. W. Chen, *Proc. Nat. Acad. Sci.* **105,** 14769 (2008).
[4.33] D. Pan, Y. Yokoyama, T. Fujita, Y. H. Liu, S. Kohara, A. Inoue and M. W. Chen, *J. Appl. Phys.* **95**, 141909 (2009).
[4.34] C.A. Schuh, T.G. Nieh, and Y. Kawamura, *J. Mater. Res.* **17,** 1651 (2002).
[4.35] W. H. Jiang and M. Atzmon, *J. Mater. Res.* **18**, 755 (2003).
[4.36] A. Concustell, M. A. Carpenter, and A. L. Greer, private communication.
[4.37] H. Ullmaier and W. Schilling, in *Radiation Damage in metallic Reactor Materials,* IAEA, Vienna (1980).
[4.38] P.M. Bronsveld, J. Groote Schaarsberg, J. Nauta and J.Th.M. De Hosson, *Mater. Sci. Eng.* **97**, 541 (1988).
[4.39] A. Kursumovic and B. Cantor, *Scr. Mater.* **34**, 1655 (1996).
[4.40] K. Csach, V. Ocelik, J. Miskuf , V. Bengus and P. Duhaj, *Trans. IEEE* **30**, 496 (1994) and references therein.
[4.41] A. Kursumovic and B. Cantor, *Scr. Mater.* **34**, 1655 (1996).
[4.42] K. Schröter, G. Wilde, R. Willnecker, M. Weiss, K. Samwer and E. Donth, *Eur. Phys. J. B* **45**, 1 (1998).
[4.43] Y. Hiki, *Mater. Sci. Eng.* **A370**, 253 (2004).
[4.44] H. T. Jeong, E. Fleury, W. T. Kim, D. H. Kim and K. Hono, *J. Phys. Soc. Jap.* **73**, 3192 (2004).
[4.45] J. M. Pelletier, *J. Alloys Comp.* **393**, 223 (2005).
[4.46] L. M. Wang, R. Liu and W. H. Wang, *J. Chem. Phys.* **128**, 164503 (2008).
[4.47] D. Rodney and C. A. Schuh, *Phys. Rev. Lett.* **102**, 235503 (2009).
[4.48] A. I. Taub and F. Spaepen, *Acta Metall.* **28**, 1781(1980).
[4.49] A. L. Greer and F. Spaepen, *Annals NY Acad. Sci.* **371**, 218 (1981).
[4.50] M. H. Cohen and D. Turnbull, *J. Chem. Phys.* **31**, 1164 (1959).
[4.51] S. S. Tsao and F. Spaepen, *Acta Metall.* **33**, 881 (1985).
[4.52] D. Deng and A. S. Argon, *Acta Metall.* **10**, 2011 (1986).
[4.53] D. Deng and A. S. Argon, *Acta Metall.* **10**, 2025 (1986).
[4.54] Z. Wang, H. B. Yu, P. Wen, H. Y. Bai and W. H. Wang, *J. Phys.*: *Condens. Matter* **23**, 142202 (2011).
[4.55] H. B. Yu, K. Samwer, Y. Wu and W. H. Wang, *Phy. Rev. Lett.* **109**, 095508 (2012).
[4.56] J. M. Pelletier, Y. Yokoyama and A. Inoue, *Mater. Trans.* **48**, 1359 (2007).
[4.57] Z. F. Zhao, P. Wen, W. H. Wang and C. H. Shek, *Appl. Phys. Lett.* **89**, 071920 (2006).

Chapter 5

DYNAMIC PROPERTIES – ANALYSIS OF LITERATURE DATA

Relaxation-time spectra obtained by DSA[1] from the anelastic strain measured by a combination of quasi-static techniques have allowed us to analyze the STZ properties in an Al-based metallic glass in detail (See Chapter 4). In Section 5.1, the master-curve method,[2–4] which has been used to argue that anelastic relaxation has a single activation energy, is analyzed. In Section 5.2, published dynamic properties of a metallic glass under cyclic constraint[5] are analyzed using a method similar to that in Chapter 4. A review of the anelastic response in dynamic experiments is presented in Section 2.1.2, and a review of prior experimental work on metallic glasses is given in Section 2.2.3.

5.1 EVALUATION OF THE MASTER-CURVE METHOD[2–4]

One of the dynamic properties of metallic glasses that have been widely investigated is the loss modulus. When the loss modulus shows an apparent peak measured at fixed temperature (T) as a function of angular frequency (ω), one can obtain an apparent activation energy barrier by measuring the peak shift with temperature. When only part of the loss modulus spectrum without the peak as a function of ω is observed, due to the limited experimental time scale, however, a master curve, in which the loss modulus spectra overlap, is constructed to obtain the activation energy.[2] The master curve is obtained by shifting each experimental curve of loss modulus, $E''(\omega,$

T), as explained below.

The master-curve method is based on an assumption of a single process with an activation energy ΔE_a. The corresponding time constant, $\tau(T)$, is given in Eqn. (2.16): $\tau(T) = \tau_0\, e^{\Delta E_a / kT}$, where τ_0 is the pre-exponential factor and k is the Boltzmann constant. According to this assumption, the loss modulus is a Cauchy function, given in Eqn. (2.19): $E''(\omega,T) = E_{1,M}\,\frac{\omega\,\tau(T)}{1+\omega^2\,\tau(T)^2}$, where $E_{1,M}$ is the elastic modulus of the spring element attached in the Maxwell unit in Fig. 2.5. $E_{1,M}$ is assumed to be temperature-independent.

In order to obtain a master curve, one of the loss modulus curves, measured at one of the temperatures, T_{ref}, is chosen first. Then, for any given T_i, an arbitrary $\omega_x(T_i)$ value, for which $E''(\omega_x(T_i),\ T_i)$ has been measured, is chosen. $\omega_{ref}(T_i)$ is defined such that $E''(\omega_{ref}(T_i),\ T_{ref}) = E''(\omega_x(T_i),\ T_i)$. $E''(\omega,\ T_i)$ as a function of $\ln(\omega)$ can be shifted by plotting $E''(\omega_i,\ T_i)$ on a logarithmic scale in ω, where $\omega_i = \frac{\omega_{ref}(T_i)}{\omega_x(T_i)}\,\omega$. Based on Eqn. (2.19) for $E''(\omega,\ T)$, the curve overlaps the reference curve, measured at T_{ref}. It should be noted that in the presence of noise, the shift should be optimized for all data points.

Assuming a single activated process with time constant $\tau(T)$, given by Eqn. (2.16), it follows from Eqn. (2.19) that:

$$\omega_{ref}(T_i) = \frac{\omega_x(T_i)\times\tau(T_i)}{\tau(T_{ref})}. \tag{5.1}$$

Substituting Eqn. (2.16) for $\tau(T_i)$ and $\tau(T_{ref})$, one obtains an expression for the shift:

$$\Delta\ln(\omega_i) = \ln(\omega_{ref}(T_i)) - \ln(\omega_x(T_i)) = \ln(\tau(T_i)/\tau(T_{ref})) = \frac{\Delta E_a}{k}\left(\frac{1}{T_i} - \frac{1}{T_{ref}}\right). \qquad (5.2)$$

In this case, when a series of $\Delta\ln(\omega_i)$ values for each $E''(\omega, T_i)$ curve used to obtain the master curve is plotted as a function of $1/T_i$, the activation energy may be obtained from its slope using Eqn. (5.2). Overlap of shifted curves has been used to argue that flow is a single activation energy process.[2–4]

In order to evaluate the master-curve method, τ_n (T = 295 K) and c_n values obtained in our quasi-static measurements of as-quenched samples (See Chapter 4) were used to calculate nine data sets of loss moduli as a function of ω using Eqn. (3.16.b) from 100 ^oC to 140 ^oC at 5 ^oC intervals (Fig. 5.1 (a)). The ΔE_a values range from $\Delta E_{a,n=14}$ = 0.83 eV to $\Delta E_{a,n=21}$ = 1.26 eV at ~ 0.06 eV intervals for the different STZ sizes. From these loss moduli, 11 data points for each temperature, spaced logarithmically from 10^{-3} $sec.^{-1}$ to 10^{2} $sec.^{-1}$ on ω at $\Delta\ln(\omega)$ intervals of ~ 1.15, were used to obtain a master curve[2–4] at T_{ref} = 120 ^oC. $\omega_x(T_i)$ was arbitrarily chosen as 3 × 10^{-3} $sec.^{-1}$, consistently for all $E''(\omega, T_i)$ to be shifted, and the corresponding $\omega_{ref}(T_i)$ was calculated for each T_i. Then, all ω in $E''(\omega, T_i)$ data were multiplied by $(\omega_{ref}(T_i)/\omega_i(T_{ref}))$ to obtain a master curve at T_{ref}. Finally, the $\Delta\ln(\omega_i)$ values, plotted as a function of $1/T_i$, were fitted using Eqn. (5.1) to obtain ΔE_a.

The gray dots in Fig. 5.1 (b) show the master curve, approximated by shifting each data set by $\Delta\ln(\omega_i)$, superimposed on the original T_{ref} = 120 ^oC curve, showing reasonably good agreement. The fit of $\Delta\ln(\omega_i)$ as a function of $1000/T$ is shown in the inset. The plot shows Arrhenius behavior, and the fit performed with Eqn. (5.1) yields a ΔE_a value of ~ 1.25 eV, which is close to the input $\Delta E_{a,n=21}$ = 1.26 eV.

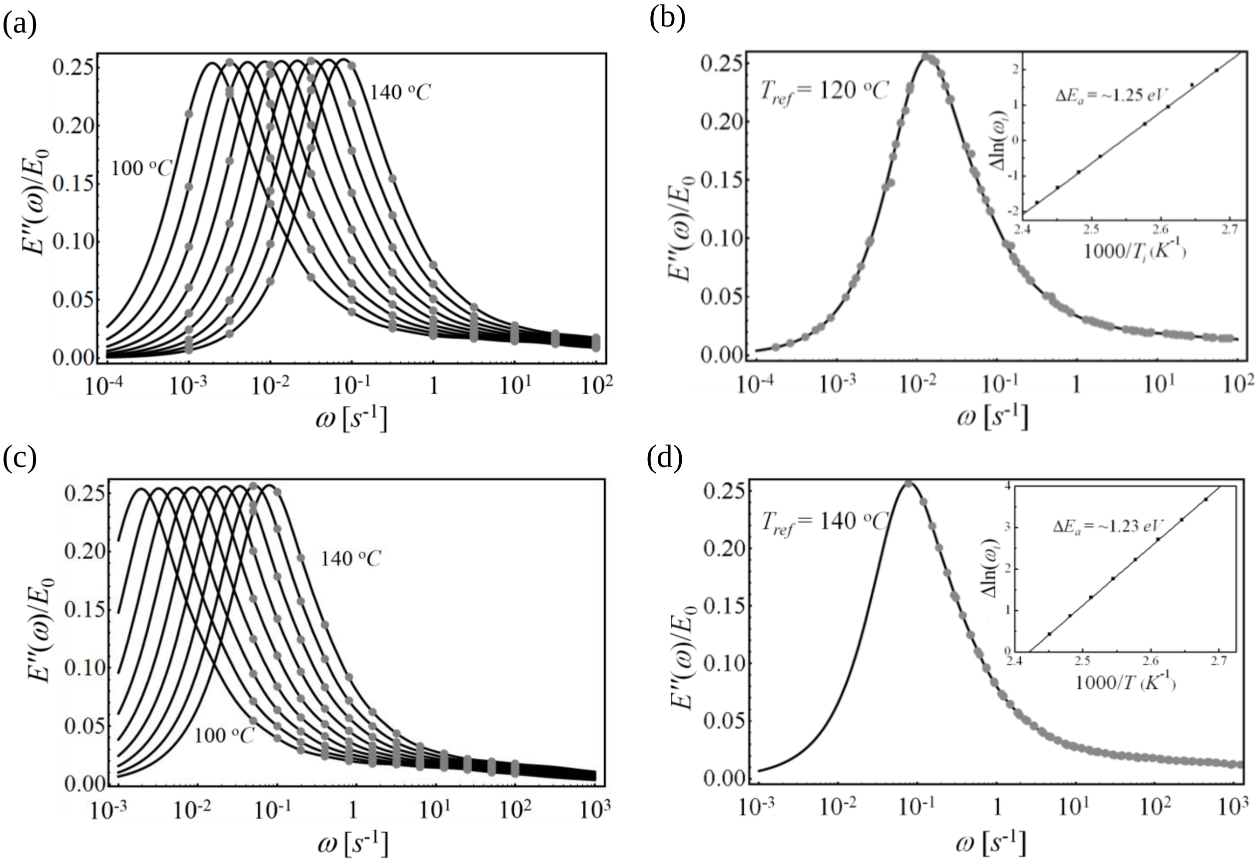

Figure 5.1 (a) Loss moduli (solid line), normalized by the high frequency Young's modulus (E_0) as a function of ω calculated using Eqn. (3.16.b) from 100 ^{o}C to 140 ^{o}C at 5 ^{o}C intervals, using $\tau_n(T = 295\ K)$ and c_n values obtained in our quasi-static measurements of as-quenched samples (See Chapter 4). For each temperature, 11 data points (gray dots), spaced logarithmically from 10^{-3} $sec.^{-1}$ to 10^{2} $sec.^{-1}$ on ω at $\Delta\ln(\omega)$ intervals of ~ 1.15 are used to approximate the master curve (b) at $T_{ref} = 120$ ^{o}C. $\Delta\ln(\omega_i)$ as a function of $(1000/T)$ is shown in the inset. (c) Same as (a), but with a narrower ω range: 12 data points (gray dots), from ~ 5×10^{-2} $sec.^{-1}$ to 10^{2} $sec.^{-1}$ at $\Delta\ln(\omega)$ intervals of ~ 0.69 for each temperature are used. (d) Same as (b) at $T_{ref} = 140$ ^{o}C using the data in (c).

Since the master-curve method is often employed with loss modulus data, where the frequency range may not include the peaks,[2] the same analysis was performed with the same original data, but with a narrower ω range: 12 data points for each temperature, spaced logarithmically from ~ $5 \times 10^{-2}\, s^{-1}$ to $10^{2}\, s^{-1}$ on ω at $\Delta\ln(\omega)$ intervals of ~ 0.69, as shown in Fig. 5.1 (c). T_{ref} is set as 140 ^{o}C, since the data at this temperature included the peak. $\omega_x(T_i)$ was arbitrarily chosen as $10^{-1}\ s^{-1}$, consistently for all $E''(\omega,\ T_i)$ that were shifted, and the corresponding $\omega_{ref}(T_i)$ for each T_i was calculated.

The master curve in Fig. 5.1 (d) shows good agreement with the original curve at 140 ^{o}C, and agrees with that in Fig. 5.1 (b). The fit, using Eqn. (5.1), performed with $\Delta\ln(\omega_i)$ as a function of $1000/T$ in the inset, however, yields a slightly smaller ΔE_a of ~ 1.23 eV. This value is in between the input $\Delta E_{a,n=20} = 1.20\ eV$ and $\Delta E_{a,n=21} = 1.26\ eV$.

Although the absolute errors in ΔE_a of the two sample tests are not significant, these tests show the uncertainty of ΔE_a obtained by the master-curve method. It should be noted that these are performed with the calculated loss moduli, which allow us to obtain $\Delta\ln(\omega_i)$ with high accuracy: In the analysis of experimental data, it is expected that the error in $\Delta\ln(\omega_i)$ will be more significant, resulting in larger errors in ΔE_a. In addition, the pre-exponential factor, τ_0, which allows for assessing the reliability of ΔE_a, cannot be obtained by the master-curve method. More importantly, this method does not fully account for the broad, asymmetric, loss modulus, which is different from a Debye peak for a single activation process (See Section 2.2.3). Most importantly, we observe that the fact that a master-curve is obtained does not prove a single activation energy.

5.2 STZ HIERARCHY EFFECT FROM LOSS MODULUS DATA

We have analyzed the experimental loss modulus data in Ref. 5, employing DSA to obtain relaxation-time spectra. The data[5] comprised a series of loss moduli as a function of ω at fixed T, ranging from 320 to 370 ^oC at intervals of 5 ^oC, for amorphous $Zr_{46.8}Ti_{8.2}Cu_{7.5}Ni_{10}Be_{27.5}$ (*at.* %). The glass transition temperature of this alloy is T_g = 348 ^oC.[6,7] Their eleven data sets were digitized using an image analyzer, Enguage Digitizer V. 4.1. Each data set contained ~ 500 – 800 data points. The digitized data sets of loss moduli ($E''(\omega)$), normalized by the high-frequency Young's modulus (E_0), are superimposed on the original plot in Fig. 5.2, showing good agreement.

We performed DSA for each digitized data set using $E''(\omega) = \sum_{i=1}^{N_2} E_i \frac{\omega \tau_i}{1+\omega^2 \tau_i^2}$ in Eqn. (3.16.b) with N_2 = 70, and the τ_i are spaced logarithmically: $\tau_{min} = (\omega_{max})^{-1}/2$ and $\tau_{max} = 2 \times (\omega_{min})^{-1}$. The E_i are fitting parameters. For the data sets below T_g, while most of the relaxation-time spectra obtained contained nearly the entire lowest-τ peak, all spectra obtained with $\tau_{max} = 2 \times (\omega_{min})^{-1}$ showed only part of the highest-τ peak near the τ_{max}. A similar observation was made in a spectrum obtained by DSA from truncated simulated data (See Section 3.6). Therefore, in order to verify these peaks, DSA was repeated with the same condition, but increased τ_{max} value: $4 \times (\omega_{min})^{-1}$ (See below). The procedure was the same as that used for simulated data, as explained in Section 3.6. τ were determined by fitting the spectrum for each temperature with a sum of log-normal distribution functions.

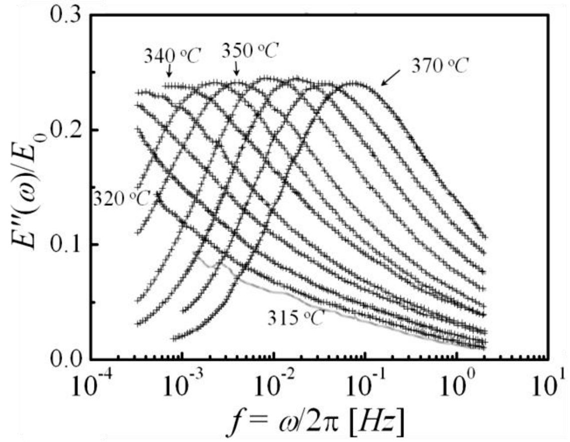

Figure 5.2 Digitized loss moduli (cross symbol, +) data sets normalized by the high frequency Young's modulus (E_0) from Ref. 5, measured as a function of $f = 2\pi/\omega$ at fixed T, ranging from 315 to 370 ^oC at intervals of 5 ^oC, for an amorphous $Zr_{46.8}Ti_{8.2}Cu_{7.5}Ni_{10}Be_{27.5}$ (*at.* %), superimposed on the original data.

The relaxation-time spectra obtained by DSA for each data set are plotted in Fig. 5.3 (a) and (b) for above and below T_g, respectively. For the loss modulus data below T_g, the highest-τ peak observed near $\tau_{max} = 2 \times (\omega_{min})^{-1}$ was further investigated by performing DSA with a larger τ_{max} value of $4 \times (\omega_{min})^{-1}$, yielding the entire peak in all spectra, with consistent behavior at smaller τ with that obtained with $\tau_{max} = 2 \times (\omega_{min})^{-1}$. These results are consistent with our DSA tests performed with the truncated simulated loss modulus data (See Section 3.6).

Fits calculated using Eqn. (3.16.b) are superimposed on the digitized data in Fig. 5.3 (c). The fits at the three lowest temperatures, extrapolated to ω below 10^{-3} *sec.*$^{-1}$, show relatively lower peaks compared to those at higher temperatures. This is likely due to low-frequency processes that were not accessible experimentally. All fits show good agreement within the experimentally accessible ω, yielding $R^2 > 0.9997$ for each. Because of the experimental limits on accessible frequencies, one expects significant peaks to be missed for high and low τ.

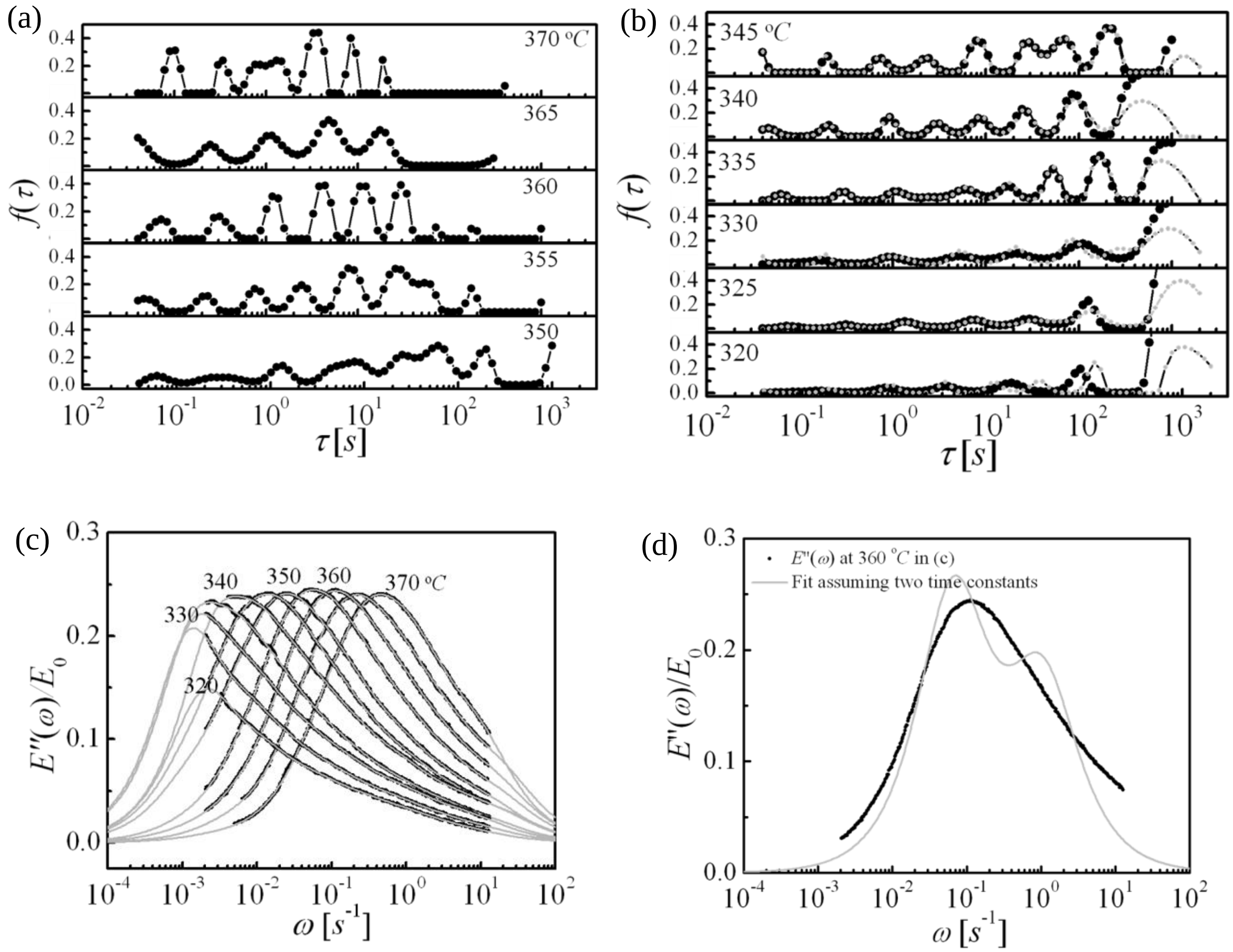

Figure 5.3 Relaxation-time spectra obtained by DSA, employing the digitized data sets of Fig. 5.2 above $T_g = 348\ ^oC$[6,7] (a) and below T_g (b). For data below T_g, DSA was performed with both $\tau_{max} = 2 \times (\omega_{min})^{-1}$ (black dots) and $\tau_{max} = 4 \times (\omega_{min})^{-1}$ (gray dots). (c) Fits (gray lines) calculated with the relaxation-time spectra plotted in (b) with $\tau_{max} = 4 \times (\omega_{min})^{-1}$ using Eqn. (3.16.b) are superimposed on the digitized data. (d) Fit performed assuming two time constants using the data set at 360 ^oC in (c).

The relaxation-time spectra display distinct peaks in each spectrum, and their distribution over a wide range of τ allows for successfully fitting the wide loss modulus spectrum. Fits performed with a single or two time constants did not yield adequate fits: A sample fit performed with two time constants using loss modulus data at 360 ^{o}C in Fig. 5.3 (c) is given in Fig. 5.3 (d). It shows disagreement with the data due to the narrow intrinsic width of the Debye peak, indicating that several processes are involved in dynamic relaxation.

We propose that the peaks in relaxation-time spectra correspond to STZs of distinct sizes, as we have observed in the quasi-static measurements. The series of loss-modulus spectra in Fig. 5.3 (a) and (b) for a range of temperatures allow us to analyze the STZ properties in $Zr_{46.8}Ti_{8.2}Cu_{7.5}Ni_{10}Be_{27.5}$, employing transition-state theory, based on our analyses discussed in Chapter 4.

Following the analysis of our quasi-static results (Chapter 4), we will now assume the peaks in Figs. 5.3 (a) and (b) correspond to STZs of volume $\Omega_n = n \times \Omega_0$, where Ω_0 is the average atomic volume and n is the number of atoms comprising an STZ. Combining the expressions for the respective time constants, $\tau_n = 3\eta_n^{'} / E_n^{'}$ and the volume fraction of potential STZs, $c_n = E_0 / E_n^{'}$, with the strain rate due to n-sized STZs given in Eqn. (4.6) in Section 4.1, $\dot{\gamma}_n = 2 c_n \gamma_0^C \nu_G \exp\left(-\frac{\Delta E_{a,n}}{kT}\right) \sinh\left(\frac{\sigma_s \gamma_0^T \Omega_n}{2kT}\right)$, τ_n at low shear stress (Newtonian flow) is reduced to:

$$\tau_n = \frac{3kT}{2\mu(1+\nu)\nu_G \gamma_0^C \gamma_0^T \Omega_n} \exp\left[\frac{\Delta E_{a,n}}{kT}\right], \tag{5.3}$$

where $\Delta E_{a,n} = \Delta \times n$ is the corresponding activation energy, given in Eqn. (7) in Section 4.1, with $\Delta = \left[\left(\frac{(7-5\nu)}{30\,(1-\nu)} + \frac{2\,(1+\nu)}{9\,(1-\nu)}\bar{\beta}^2\right)\gamma_0^T + \frac{1}{2}\frac{\bar{\sigma}_{STZ}}{\mu}\right]\mu\,\gamma_0^T\,\Omega_0$. $\ln[\tau_n]$ is rewritten in terms of $n = (n_0 + m)$, where n_0 is the number of atoms in the smallest STZ and m is a non-negative integer:

$$\ln[\tau_n] = \ln[\Gamma^{-1}\,T] - \ln[n_0 + m] + \frac{\Delta \times (n_0 + m)}{k\,T}\,, \tag{5.4}$$

where $\Gamma^{-1} = \frac{3k}{2\,\mu(1+\nu)\,\nu_G\,\gamma_0^C\,\gamma_0^T\,\Omega_0}$.

It has been reported that while the high-frequency Young's modulus of metallic glasses is relatively temperature-insensitive upon heating below T_g, it varies significantly as a function of T above T_g.[8,9] Therefore, approximate linear temperature dependence of the shear modulus:[8–11]

$$\mu_{aboveT_g} = \mu_{Tg}\,[1 - \alpha(T - T_g)]\,, \tag{5.5}$$

where α is the fractional decrease in μ per K, is incorporated into μ in both Γ^{-1} and Δ in Eqn. (5.4) to analyze the results obtained above T_g.

Equation (5.4) will now be used to determine STZ properties from the spectra in Fig. 5.3. The challenge is to determine which sets of peaks at different temperatures corresponds to each STZ size, n. When $\ln[\tau]$ values, determined from the medians of the respective peaks in the spectrum, are plotted against $1/kT$, sets of τ_n points, each set corresponding to the same n value, are selected tentatively. The slope of each correctly chosen set is equal to $\Delta E_{a,n}$ for a particular n, separately below and above T_g. Once the groupings of τ_n are determined, fitting these τ_n plotted against $1/kT$ for a range of m values simultaneously using Eqn. (5.4) yields the variables, n_0, Γ^{-1} and Δ. These allow us to calculate the STZ properties, as detailed below.

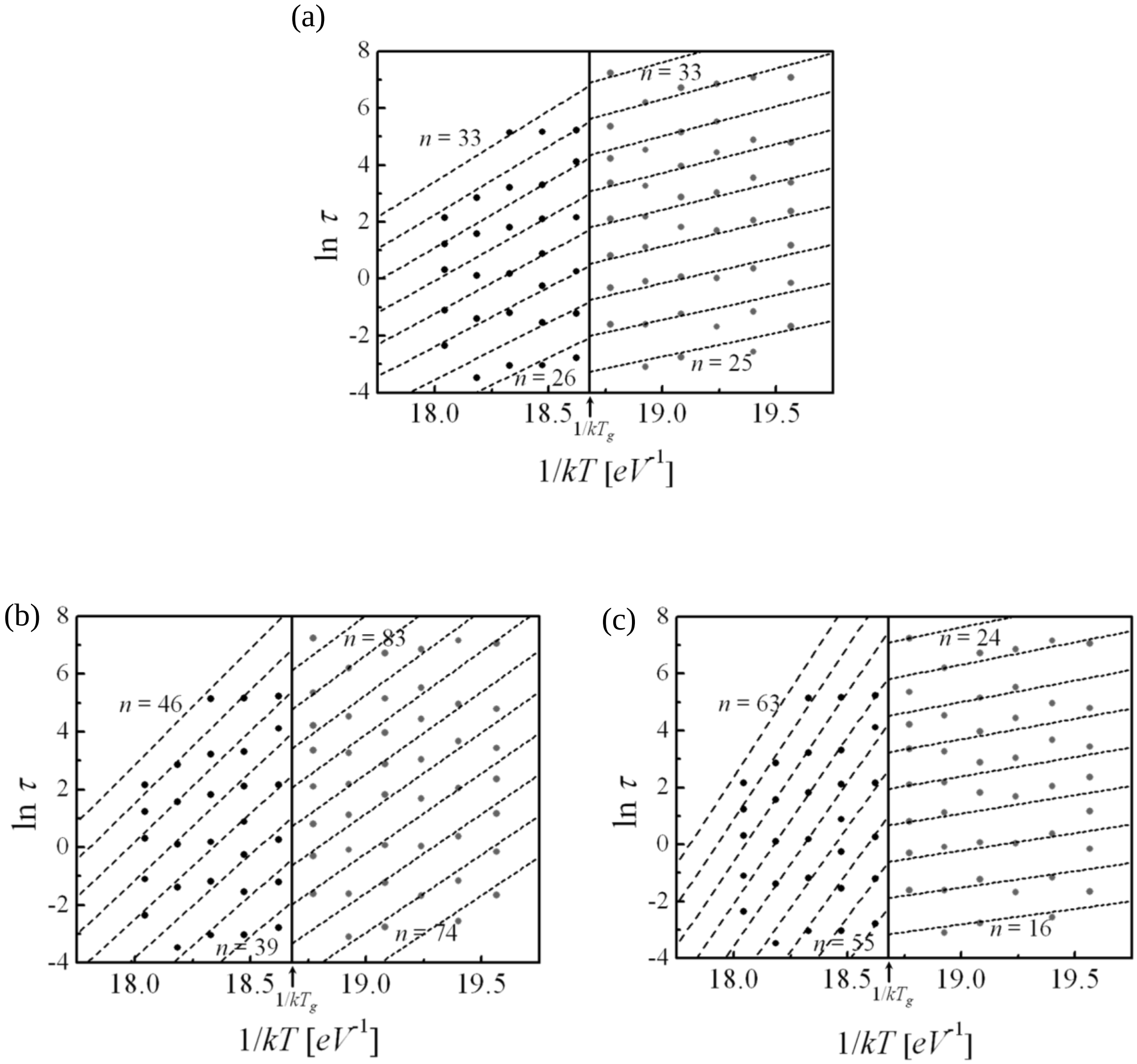

Figure 5.4 ln[τ], determined from the median of the respective peak in the relaxation-time spectra, plotted as a function of 1/kT for three tentative groupings of τ_n (a) through (c) below (gray circles) and above T_g (black circles). Simultaneous fit performed using Eqn. (5.4) is shown with dashed lines for each $n = (n_0 + m)$. Above T_g, $\alpha = 2 \times 10^{-3}$ /K was used in Eqn. (5.5). (a) provides the best fit. Out of nine possible combinations, continuity of the fits at T_g is obtained only for the combination displayed in (a).

Plots of ln[τ] as a function of $1/kT$, separately fitted below and above T_g with three possible groupings of τ_n for each temperature regime, are shown in Fig. 5.4 (a) to (c). For these, the simultaneous fit results, calculated using Eqn. (5.4), or Eqn. (5.4) and (5.5), respectively, are plotted with dashed lines. Above T_g, $\alpha = 2 \times 10^{-3}$ /K was used in Eqn. (5.5), see discussion below. Of the nine possible combinations of groupings, only that of Fig. 5.3 (a) shows continuity at T_g. The simultaneous fit in Fig. 5.4 (a) below T_g yields $R^2 = 0.991797$, as compared with $R^2 =$ 0.987152 and 0.987543 for (b) and (c), respectively. The plot in (a) shows Arrhenius behavior of τ, and more importantly, the processes observed have a range of apparent activation energies. In addition, while three to four relaxation-time constants out of total 45 time constants slightly deviate from the fit below T_g, the results, showing good agreement with Eqn. (5.4) for over 40 time constants, support our notion of a hierarchy of STZs in single atomic increments, as designated with $n = (n_0 + m)$ on the plot.

While Arrhenius behavior was assumed in Chapter 4, it is directly exhibited by the data here. Also, our previous analysis in Chapter 4 to yield the STZ volumes was performed with assumed variables, γ_0^T, $\nu_{G.}$ In contrast, the fits to the present dynamic data allow us to determine two of the three quantities, γ_0^T, ν_G and Ω_0, by assuming one of them as detailed below. We use the Γ^{-1} and Δ values obtained from the simultaneous fit in Fig. 5.4 (a), the literature value, $\mu =$ 37.4 GPa and an estimated $\nu = 0.35$ for the metallic glass used.[12,13]

We first discuss the fitting results below T_g. Assuming $\Omega_0 = 1.67 \times 10^{-29}$ m^3, as estimated by Vegard's law[14] from the alloy composition, Γ^{-1} and Δ obtained from the simultaneous fit yield $\nu_G = 2.7 \times 10^{14}/s$ and $\gamma_0^T = 0.15$. Alternatively, if we assume $\gamma_0^T = 0.2$,[15] we obtain $\Omega_0 = 9.45 \times 10^{-30}\, m^3$ and $\nu_G = 2.6 \times 10^{14}/s$. Both sets are similar to the values we had previously assumed (See

Chapter 4), and physically reasonable.[15] The simultaneous fit yields the number of atoms in STZs in atomic increments, ranging from n = 25 (m = 0) to 33 (m = 8) for both γ_0^T used. The fact that the window of n values obtained lies higher than for our quasi-static results (Chapter 4) is expected since the dynamic data were acquired at higher temperatures. While γ_0^T calculated from the simultaneous fit results in Fig. 5.4 (b) and (c) is similar to the value obtained for Fig. 5.4 (a), 0.15, ν_G differs by several orders of magnitude: ν_G = ~ 3.1 × 10^{44}/*sec.* and ~ 3.5 × 10^9/*sec.* for (b) and (c), respectively, both of which are unphysical. We thus conclude that the grouping in Fig. 5.4 (a) yields the best fit and the most physical results below T_g.

The fitting results above T_g are now discussed. Although the quality of the simultaneous fit is not as good as below T_g, the continuity of data at T_g for individual n values is noted. In particular, such continuity was obtained only with the choice of τ_n groupings below and above T_g shown in Fig. 5.4 (a), out of nine possible combined plots. The fitting parameters, n_0, Γ^{-1} and Δ above T_g, are dependent on the linear temperature coefficient of shear modulus, α, but the slope in Fig. 5.4 is weakly affected by the choice of different α values. We performed calculations with different α for the ln[τ_n] grouping above T_g in Fig. 5.4 (a). Assuming $\alpha = 2 \times 10^{-3}$ /K, the simultaneous fit yield Ω_n ranging from 26 (m = 1) to 33 (m = 8) atoms, the same as that obtained below T_g, with mutual agreement of γ_0^T, ν_G and Ω_0 with fitting results below T_g as well: Assuming $\Omega_0 = 1.67 \times 10^{-29}$ m^3, Γ^{-1} and Δ obtained from the simultaneous fit yield γ_0^T = ~ 0.15, ν_G = ~ 1.25 × 10^{14}/*sec.*; assuming γ_0^T = 0.2, they yield $\Omega_0 = 9.4 \times 10^{-30}\, m^3$ and ν_G = ~ 1.22 × 10^{14}/*sec*. Simultaneous fits performed with three different α values, 5 × 10^{-3}, 3 × 10^{-3} and 5 × 10^{-4} /K , yield ν_G values of ~ 1.3 × 10^7 /*sec.*, ~ 5.4 × 10^{10} /*sec.* and ~ 1.6 × 10^{25} /*sec.*, respectively, all of which are unphysical. The assumed α value may need to be experimentally verified at high temperature, however, since a range of values was reported in literature.[8–11] For the groupings of τ_n in Fig. 5.4 (b) and (c), the simultaneous fit yields the ν_G value of ~ 2.1 × 10^{24} /*sec.* and ~ 3.1 × 10^{38} /*sec.*, respectively, which are unphysical either, and more importantly, there is no continuity at T_g.

In summary, relaxation-time spectra are obtained by DSA from the loss modulus data for $Zr_{46.8}Ti_{8.2}Cu_{7.5}Ni_{10}Be_{27.5}$ in Ref. 5. Each spectrum contains several distinct peaks, as observed in our quasi-static data, and these peaks allow for resolving distinct processes contributing a wide loss modulus spectrum. To our knowledge, this is the first time in which relaxation-time spectra were obtained from dynamic data. Combining our analysis of an atomically quantized hierarchy of STZs in Chapter 4 with transition-state theory, the peak positions at different temperatures are analyzed by performing simultaneous fits. These simultaneous fits performed with different groupings of τ_n allow us to obtain the STZ properties: γ_0^T, ν_G and *n*. The γ_0^T and *n* values obtained from the best fit in Fig. 5.4 (a), which also yields a physical ν_G value, are ~ 0.15 and n = 25 to 33, respectively. The compatibility of the *n* values below and above T_g is noted. These results strongly confirm with our interpretation of the quasi-static measurement data.

5.3 REFERENCES

[5.1] J. R. Cost, *J. Appl. Phys.* **54**, 2137 (1983).
[5.2] H. T. Jeong, E. Fleury, W. T. Kim, D. H. Kim and K. Hono, *Phys. Soc. Jap*. **11**, 3192 (2004).
[5.3] K. L. Ngai, D. J. Plazek and R. W. Rendell, *Rheol. Acta.* **36**, 307 (1997).
[5.4] L. Salmén, *J. Mater. Sci.* **19**, 3090 (1984).
[5.5] J. M. Pelletier, *J. Alloys Comp*. **393**, 223 (2005).
[5.6] V. H. Hammond, M. D. Houtz and J. M. O’Reilly, *J. Non-Crys. Sol.* **325**, 179 (2003).
[5.7] W. H. Wang, C. Dong and C. H. Shek, *Mater. Sci. Eng.* ***R*44**, 45 (2004).
[5.8] V. Keryvin, M-L. Vaillant, T. Rouxel, M. Huger, T. Gloriant and Y. Kawamura, *Intermetallics* **10**, 1289 (2002).
[5.9] T. Rouxel, *J. Am. Ceram. Soc*. **90**, 3019 (2007).

[5.10] J. Q. Wang, W. H. Wang and H. Y. Bai, *J. Non-Crys. Sol*. **357**, 223 (2011).
[5.11] W. H. Wang, *Prog. Mater. Sci.* **57**, 487 (2012).
[5.12] G. Duan, M. L. Lind, K. D. Blauwe, A. Wiest and W. L. Johnson, *Appl. Phys. Lett*. **90**, 211901 (2007).
[5.13] J. Lu, G. Ravichandran and W. L. Johnson, *Acta Mater*. **51**, 3429 (2003).
[5.14] L. Vegard, *Z. Phys.* **5**, 17 (1921).
[5.15] J. D. Ju, D. Jang, A. Nwangkpa and M. Atzmon, *J. Appl. Phys.* **109**, 053522 (2011).

Chapter 6

DISCUSSION

6.1 ACTIVATION ENERGY SPECTRA – EVALUATION OF THE TEMPERATURE-STEPPING APPROACH

The relaxation-time spectra obtained by DSA from our experimental quasi-static relaxation data have shown distinct time constants, τ_n. Although smaller number of distinct peaks have been observed in the spectra for other metallic glasses, due to the limited experimental time scale,[1–3] their results indicate that our results are not unique to the present alloy but universal in the anelastic deformation of metallic glasses.

In addition, we have observed discrete time constants for anelastic relaxation in spectra obtained from dynamic loss modulus data.[4] The loss modulus as a function of ω at constant temperature, $E''(\omega)$, exhibits a broad, asymmetric peak in $\ln(\omega)$ (See Section 2.1.2 and Chapter 5),[5,6] presumably due to a distribution of time constants. Using DSA, we have been able to obtain the relaxation-time spectra, even though their features are obscured in $E''(\omega)$ by overlap of Debye peaks corresponding to distinct processes. For each temperature, the spectra obtained display distinct peaks in a range of time constants, as in the quasi-static experimental data.

We have shown that the distinct peaks in the relaxation-time spectra represent isolated STZs with distinct volumes, undergoing irreversible shear during anelastic relaxation. An STZ type labeled with m in Section 4.1 consists of ($n = n_0 + m$) atoms, where n_0 is the number of atoms in the smallest STZ type obtained (See Chapter 5). The activation energy barrier for a shear transformation is proportional to the STZ volume, as shown in Eqn. (2.21), i.e., larger STZs have higher activation energy, $\Delta E_a(\Omega_n)$, where Ω_n is the volume of an n-size STZ. Therefore, for each STZ size, Ω_n, τ_n has distinct temperature dependence, as given in Eqn. (5.3) and (5.4): $\tau_n = \frac{3kT}{2\mu(1+\nu)\nu_G \gamma_0^C \gamma_0^T \Omega_n} \exp\left[\frac{\Delta E_a(\Omega_n)}{kT}\right]$.

Our results may also be relevant to atomic diffusion in metallic glasses.[7,8] It has been suggested[8] that diffusion in metallic glasses is accommodated cooperatively in atomic clusters rather than a series of single atomic hops[9] mediated by vacancy-like defects, i.e., self-diffusion. This process may be explained by successive shear transformations, suggesting that diffusion may take place via STZs, in which atoms experience cooperative atomic rearrangements. This has also been observed in molecular dynamics simulations.[10] In fact, it has been observed in simulation studies by Delogu[11] that the atoms, which are involved in the cooperative diffusion without external stress, also preferentially undergo microscopic strain under shear. In addition, Yu[12] and coworkers have proposed that the relaxation process corresponding to the low-temperature tail in loss modulus (termed a slow secondary (β) relaxation process in Ref. 12, which may refer to smaller τ_n in our analysis) and cooperative diffusion are closely related: while diffusion of a large alloy element in a multi-component metallic glass, such as Pd in a $Pd_{43}Ni_{10}Cu_{27}P_{20}$ glass, is correlated with α relaxations,[13] which correspond to the apparent peak with high intensity at high temperature, that of a small element, such as P, is related to the β relaxation, based on the experimental data showing similar activation energies. Cooperative diffusion has been observed not only in as-quenched but also structurally relaxed metallic glasses.[14,15]

While c_n, i.e., the n (or corresponding activation energy, $\Delta E_{a,n_m}$)-dependent distribution of the volume fraction of potential STZs, has not been resolved by other studies, we note the experimental study of the activation energy spectrum in metallic glasses carried out by Argon and Kuo.[16] Although their temperature stepping method had limited resolution, as discussed in Section 2.2.3, it is instructive to re-evaluate their activation energy spectra,[16] and compare them with our c_n.

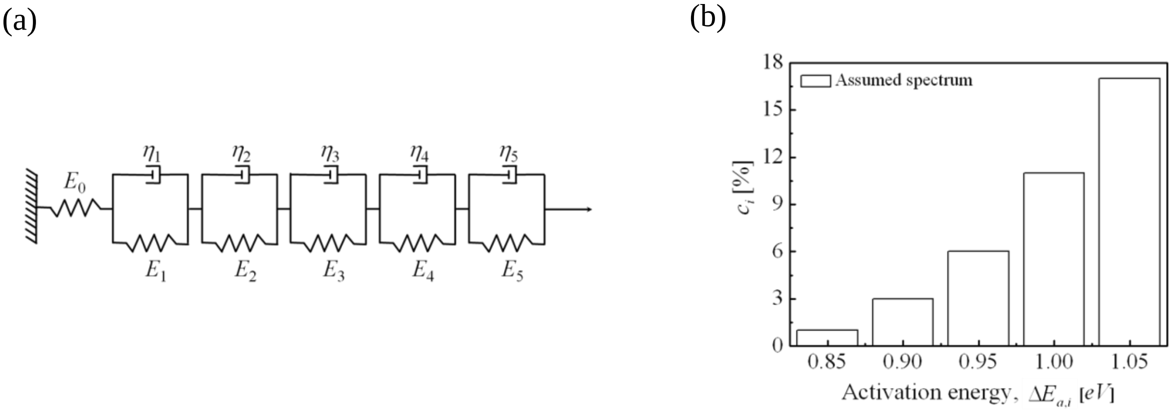

Figure 6.1 (a) A linear model for a simulated solid with five distinct processes. (b) Histogram of assumed c_i for individual processes of the linear series of the standard anelastic solids on the left plotted as a function of $\Delta E_{a,i}$.

In order to evaluate the temperature-stepping approach of Ref. 16 (See Section 2.2.3), we have performed numerical simulations. With the benefit of our present results,[17] we now attribute the distribution of activation energies to the quantized hierarchy of STZs. A solid was modeled with a series of five Voigt units, Fig. 6.1 (a), it is assumed that the corresponding processes have activation energies ranging from 0.85 to 1.05 *eV* at 0.05 *eV* intervals, resulting in five distinct relaxation-time constants at each temperature T_i, τ_{i,T_i} , where i = 1,…,5, using Eqn. (5.1). The smallest STZ size is assumed arbitrarily to be 20 atomic volumes, $n_0 = 20$.

The spectrum height is taken to increase as a function of i such that c_i is qualitatively similar to our results, plotted in Ref. 17. Figure 6.1 (b) shows the assumed c_i as a function of $\Delta E_{a,i}$. Following Argon and Kuo,[16] the simulated solid, which is first equilibrated under stress at high temperature, is assumed to not recover upon quenching to 0 ^{o}C or during the time it takes to step up the temperature. The simulated solid is allowed to relax at increasing temperature steps of 20 ^{o}C.

According to the temperature stepping method[16] employing the step-function approximation, the overall anelastic strain measured at T_i is attributed to the relaxation process, $\Delta E_{a,i}$. Since five distinct anelastic processes, i = 1,…,5, were assumed for current simulation, anelastic strain recovery was calculated as a function of time at increasing temperatures, $T_{i=1,\ldots,5}$ = 20, 40, 60, 80 and 100 ^{o}C, for each to obtain c_i : T_i is the temperature step at which the overall anelastic strain of the simulated solid for anelastic process, *i*, is calculated as a function of time.

In addition, at each temperature step, T_i, the total relaxation time, t_i, up to which the anelastic strain is calculated, is set consistently to $3\tau_{i,T_i}$ (dotted line in Fig. 6.2 (a)). While each $3\tau_{i,T_i}$ allows for 95 % relaxation of the corresponding processes for each, it does not exceed τ_{i+1} at T_i (See Fig. 6.2 (a)), which allows us to attribute the anelastic strain recovery calculated up to $3\tau_{i,T_i}$ at T_i to the anelastic process, *i*. Figure 6.2 (b) was used to determine the approximated c_i (Fig. 6.2 (c)).

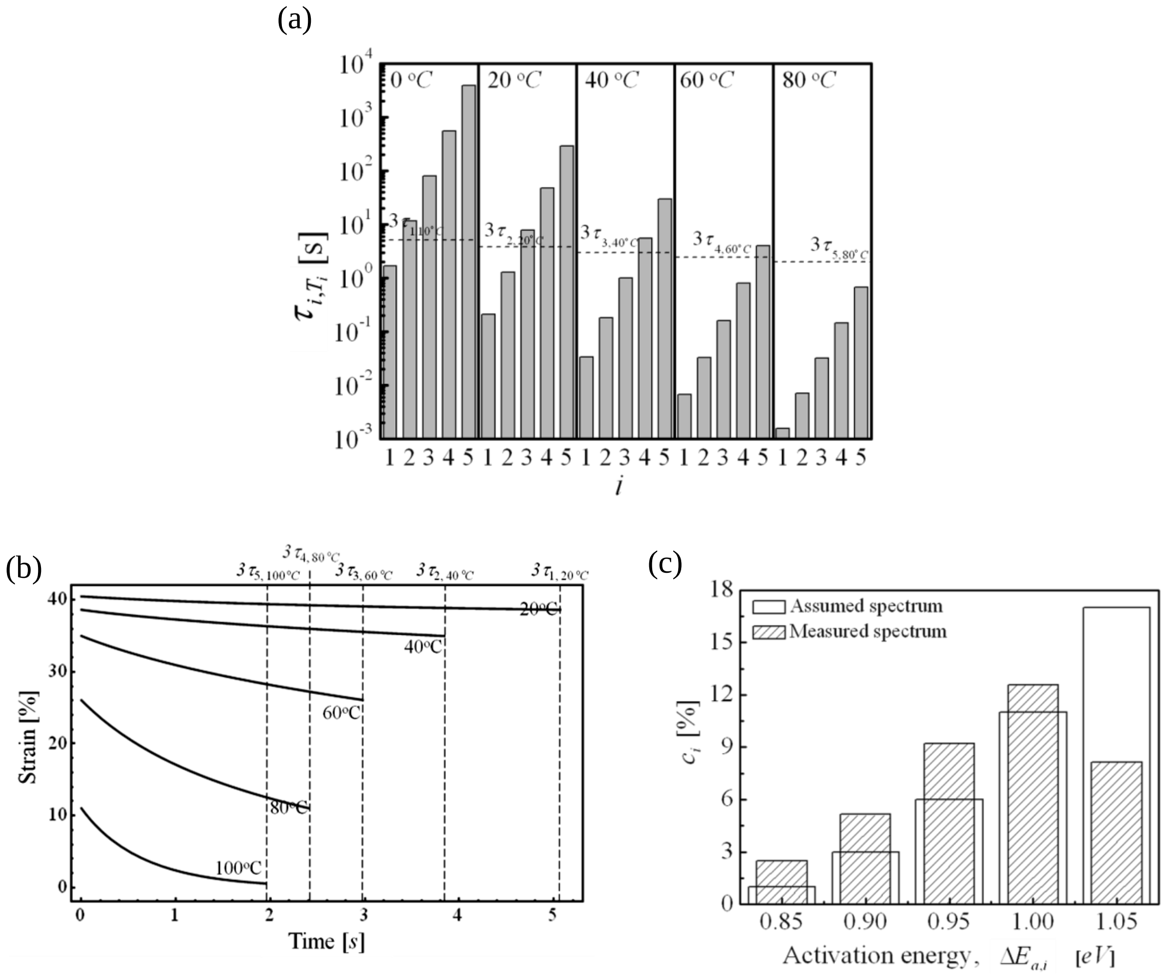

Figure 6.2 (a) τ_{i,T_i} of the simulated solid, calculated at respective $T_{i=1,\ldots,5}$ = 20, 40, 60, 80 and 100 ^oC. $3\tau_{i,T_i}$, at which the overall anelastic strain was determined are shown with dotted lines. (b) Anelastic strain recovery as a function of time for temperature steps of 20 ^oC for a linear series of the standard anelastic solids in 6.2 (a). (c) Histogram of approximate c_i (dashed box) obtained by simulating isothermal measurements of anelastic strain recovery at $3\tau_{i,T_i}$ for temperature steps, T_i from T_1 (20 ^oC) to T_5 (100 ^oC), are superimposed on the original, assumed, c_i (blank box).

We observe in Fig. 6.2 (c) that processes with $\Delta E_{a,i}$, previously neglected at $T < T_{i+1}$ due to their slow relaxation processes, substantially contribute to the strain relaxation at lower temperatures, and therefore, make a reduced subsequent contribution at higher T. This results in an overestimation of the spectrum in the low activation energy regime and an underestimation for high activation energies. It is emphasized that although Argon and Kuo's stepping method[16] suffers from this experimentally inevitable limitation, it provides a major contribution to understanding of the spectrum of activation energies, as emphasized in Section 2.2.3.

6.2 REFERENCES

[6.1] P. M. Bronsveld, J. Groote Schaarsberg, J. Nauta, and J. Th. M. De Hosson, *Mater. Sci. Eng.* **97**, 541 (1988).
[6.2] A. Kursumovic, M. G. Scott and R. W. Cahn, *Scripta Metall.* **24**, 1307 (1990).
[6.3] K. Csach, V. Ocelik, J. Miskuf, V. Bengus, and P. Duhaj, *Trans. IEEE* **30**, 496 (1994).
[6.4] J. M. Pelletier, *J. Alloys Comp.* **393**, 223 (2005).
[6.5] M. Barmatz and H. S. Chen, *Phys. Rev.* ***B*9**, 4073 (1974).
[6.6] B. S. Berry, W. C. Pritchet and C. C. Tsuei, *Phy. Rev. Lett.* **41**, 410 (1978).
[6.7] F. Faupel, W. Frank, M.-P. Macht, H. Mehrer, V. Naundorf, K. Rätzke, H. R. Schober, S. K. Sharma and H. Teichler, *Rev. Modern Phys.* **75**, 237 (2003).
[6.8] K. Rätzke, P. W. Hüppe and F. Faupel, *Phy. Rev. Lett.* **68**, 2347 (1992).
[6.9] F. Spaepen, *Acta Metall.* **25**, 407 (1977).
[6.10] D. Deng, A. S. Argon and S. Yip, *Phil. Trans. R. Soc. Lond.* ***A*329**, 613 (1989).
[6.11] F. Delogu, *Phy. Rev. Lett.* **100**, 075901 (2008).
[6.12] H. B. Yu, K. Samwer, Y. Wu and W. H. Wang, *Phy. Rev. Lett.* **109**, 095508 (2012).
[6.13] A. Bartsch, K. Rätzke, A. Meyer and F. Faupel, *Phy. Rev. Lett.* **104**, 195901 (2010).
[6.14] F. Faupel, P. W. Hüppe and K. Rätzke, *Phy. Rev. Lett.* **65**, 1219 (1990).
[6.15] A. Heesemann, V. Zöllmer, K. K. Rätzke and F. Faupel, *Phy. Rev. Lett.* **84**, 1467 (2000).
[6.16] A. S. Argon and H. Y. Kuo, *J. Non-Crys. Sol.* **37**, 241 (1980).
[6.17] J. D. Ju, D. Jang, A. Nwankpa and M. Atzmon, *J. Appl. Phys.* **109**, 053522 (2011).

Chapter 7

SUMMARY AND SUGGESTIONS FOR FUTURE WORK

7.1 SUMMARY

We have probed STZ properties using anelasticity measurements. Relaxation-time spectra, obtained from the experimental data by DSA,[1] exhibit distinct peaks. Our computational studies, performed for testing DSA with simulated data that include noise, have confirmed that the method is able to resolve the input relaxation-time spectra with accuracy. Our analysis of the relaxation-time spectra in terms of the standard anelastic solid model with a linear combination of spring-dashpot, in combination with Ref. 2, allows for calculating the STZ volumes (Ω_n) and the volume fraction of potential STZs (c_n). Active STZs are resolved by a single atomic volume and are shown to consist of n = 14 – 21 atoms in $Al_{86.8}Ni_{3.7}Y_{9.5}$. An atomically quantized hierarchy, with the same STZ sizes, is observed in structurally relaxed samples. DSA, performed with dynamic data in amorphous $Zr_{46.8}Ti_{8.2}Cu_{7.5}Ni_{10}Be_{27.5}$ in Ref. 3, also yields relaxation-time spectra exhibiting distinct peaks, and these peaks are analyzed to verify the STZ properties, obtained in our quasi-static measurements. The analyses, employing simultaneous fits to account for Arrhenius behavior of respective time constants and their n-dependence, yield n = 25 – 33, with mutual agreement of n, γ_0^T and ν_G below and above T_g. The window of n values corresponds to STZs that can be characterized under the given experimental conditions (See Chapter 4), and are part of a wider hierarchy.

While structural relaxation leading to an increase in effective viscosity ($\eta_n^{'}$) does not change Ω_n, the c_n values decrease substantially due to the relaxation. The annihilation of potential STZs and the resulting effect on their distribution is interpreted in terms of the free volume model.[4,5] The Cohen and Turnbull free volume model (Ref. 4 and 5), based on an atomic flow unit, is modified to account for STZs as the basic units. The resulting expression is fitted to c_n, indicating that ~ 2 % change in average free volume, v_f, due to the structural relaxation reduces c_n substantially, resulting in a $\eta_n^{'}$ rise.[6] In addition, the n dependence of c_n and Ω_n, with the corresponding activation energies, account for (a) the low-temperature tail in loss moduli[7,8] and (b) Argon and Kuo's[2] activation-energy spectra obtained using the temperature-stepping method. For the temperature-stepping method, a simple simulation shows that the contribution of c_n with higher activation energy processes is underestimated due to the overestimation of those of lower activation energies.

In the present work, the STZ properties, analyzed by applying DSA to experimental anelasticity data at low stress and strain levels, have been studied. Based on our current findings, experimental/theoretical research can be expanded to improve the microscopic understanding of a broader range of mechanical properties of metallic glasses. For this purpose, future work that may contribute to a more comprehensive understanding of the mechanical properties is proposed:

7.2 SUGGESTIONS FOR FUTURE WORK

1. *Composition effects on STZs*. Our analyses have not taken into account composition effects on STZs. These analyses can be improved by considering the effects on STZs due to the different types of alloying elements. For example, while many metallic glasses show a low-temperature tail in loss moduli measured at fixed frequency as a function of temperature, as

expected according to our interpretation of c_n, amorphous $La_{68}Al_{10}Cu_{20}Co_2$ shows a prominent peak at low temperature.[7] The results may indicate that c_n for small STZs in this alloy is higher than in the other alloys. Although this observation is limited to $La_{68}Al_{10}Cu_{20}Co_2$, the result suggests that the anelastic relaxation processes are not only dependent on STZ sizes but also on the alloying elements.

It has been reported in Ref. 8 that activation energies for α and β relaxations in loss moduli are similar to those for diffusion of large and small alloying elements, respectively: Pd in $Pd_{43}Cu_{27}Ni_{10}P_{20}$,[9] and P in $Pd_{40}Cu_{30}Ni_{10}P_{20}$ or Be in $Zr_{46.75}Ti_{8.25}Cu_{7.5}Ni_{10}Be_{27.5}$. Although clear conclusions have not been drawn from the observations, these observations suggest that diffusion and anelastic relaxation are closely related to each other, since α and β relaxations termed in Ref. 8 correspond to large and small STZs, respectively, in our analyses. Based on the prior experimental results, therefore, detailed studies of STZs, taking the sizes of alloying elements and their interactions into account, to rationalize the composition effects on STZs may be of great impact. These proposed studies may allow for improving the current, basic, understanding of STZs. Analyzing the STZ properties in different glass-forming alloys that are useful in terms of their engineering properties, e.g., glass forming ability, strength and strain-to-failure, may provide an opportunity for designing alloy compositions for applications as well.

2. *Temperature dependence of anelastic behavior and activation energies*. We have analyzed quasi-static anelastic relaxation data based on assumptions of Arrhenius behavior of relaxation processes derived from the constitutive equation,[10,11] Eqn. (2.20), using Argon's[11,12] expression for the activation energies, Eqn. (2.21). While Arrhenius behavior is observed directly in our analyses of loss moduli of Ref. 3, it is instructive to evaluate these assumptions experimentally in a range of temperatures.

In principle, anelastic strain evolution measured by quasi-static methods at different temperatures, followed by DSA of these data, may allow for directly evaluating the assumptions, by analyzing the temperature dependence of respective time constants in relaxation-time spectra (See Chapter 5). In practice, however, *in-situ* measurements of the strains at elevated temperatures can be challenging due to the difficulty of strain measurements inside a furnace. *Ex-situ* measurements may be an alternative, but they suffer from potential artifacts: temperature drop/overshoot and limitation on strain measurements at short times during the measurements.

Dynamic experiments, therefore, may be more appropriate than quasi-static measurements for the given objectives. Performing the measurements at different applied stress levels may also allow for detailed studies of anelastic properties in the linear and non-linear regime[13], at low and high applied stress, respectively. It is noted that structural relaxation does not lead to changes in activation energies but in c_n (See Chapter 4). In order to characterize the STZ sizes, dynamic data measured as a function of frequency at fixed temperature can be used to obtain the relaxation-time spectra by DSA, followed by analyzing them using the methods discussed in Chapter 5. In addition to the STZ sizes, important STZ properties, γ_0^T, Ω_0 and ν_G can also be obtained using the methods. These studies will allow for verifying not only our observations on the STZ properties in quasi-static data using a different experimental technique, but also the temperature dependence.[14,15,16]

3. *Pre-compression effects on subsequent plastic deformation behavior*. Based on the experimental observations in physical analogues,[17,18] it has been suggested that shear bands, which accommodate intense local plastic strain in the high stress and strain regime (See Chapter 1),[19] likely originate from sequential cascades of STZs due to their elastic interactions.[20] It may

suggest that formation of shear bands is initiated by STZs that are activated prior to yielding, followed by rapid propagation with increasing applied strain.[19]

It has been reported that samples, subjected to pre-compression at ~ 90 % of their yield strengths, σ_y, for ~ 12 *hr.*, subsequently show significant increase in the compressive strain-to-failure in uniaxial tests at the expense of yield strength loss of ~ 20 %.[21] Based on molecular dynamic simulations,[21] this ductility increase has been attributed to an increase in the number of loosely packed atomic clusters due to the dilatation during pre-compression at ~ 90 % of σ_y. The term, "loosely packed clusters" may refer to the potential STZs in our interpretation, but a correlation between dilatation, i.e., increase in the free volume, v_f, and such clusters has not been clarified.

It has been suggested that pre-compression at ~ 90 % of σ_y[21] may result in enhanced formation of multiple shear bands during subsequent plastic deformation.[22,23] It is not clear at this point whether such a change in plastic behavior is the signature of multiple nuclei formed simultaneously prior to their propagation, or of the sequential formation from the primary band fronts due to stress concentration. In order to elucidate the formation processes of shear bands, pre-compression at ~ 90 % of σ_y, followed by deforming the samples plastically and subsequent characterization of the resulting shear bands is proposed. For the characterization, an optical or a scanning electron microscopy, depending on the required resolution, can be used. The observed shear-band morphology can be compared with that in (a) as-quenched and (b) structurally relaxed samples that are plastically deformed without pre-compression as a baseline.

In Ref. 21, it is claimed that the anelastic strain developed during ~ 12 *hr.* of pre-compression at ~ 90 % of σ_y completely recovered during 4 *hr.* in a stress-free condition. For anelastic processes with time constants longer than the duration of the experiment, the time for anelastic strain recovery is much longer than that spent to develop it under constraint (See Section 2.1.1 and Chapter 4). The authors' claim,[21] therefore, need to be experimentally evaluated.

Measurements of the strain recovery of pre-compressed samples in a stress-free state for a long-period of time to evaluate the claim about the anelasticity are proposed. The measurements may also allow for elucidating whether the strain-to-failure of pre-compressed samples is higher due to potentially remaining anelastic sites. It can be also useful to measure stress-strain curves for pre-compressed samples that have undergone stress-free anelastic strain recovery for different durations. These measurements will allow for identifying microscopic processes that result in the increased strain-to-failure of pre-compressed samples.

If the measurements show that plastic deformation is altered by residual anelastic strain of the pre-compressed samples, detailed analysis of the anelastic strain recovery of pre-compressed samples are proposed to characterize the STZ properties in them. The uni-axial anelastic strain data can be analyzed by DSA to obtain the relaxation-time spectra. From the spectra, while STZ properties may be directly obtained, using the methods discussed in Chapter 4, their interactions due to the stress field around individual STZs[18,20] may require additional computational studies, employing Eshelby inclusion theory.[24] The analysis of Ω_n, c_n and the stress fields acting on individual STZs may allow for modeling of the formation process for shear bands. Theoretical/experimental studies of the formation of shear bands may be expanded by comparing the results with those in atomic-scale simulations.

The proposed work would be of great impact not only on the basic understanding of the distinct plastic deformation of metallic glasses, but also on their engineering applications. For example, while many experimental studies have made progress in increasing the strain-to-failure of metallic glasses,[21,25,26,27] theoretical understanding of such increase has been limited to the phenomenological interpretations, e.g., multiple shear bands. The proposed work, based on our current study that allows for probing the STZ properties in detail, however, will improve the understanding of microscopic mechanisms that lead to the distinct plastic deformation.[21] In addition, the fundamental study may allow for engineering metallic glasses to take advantage of their remarkable properties as well.

7.3 REFERENCES

[7.1] J. R. Cost, *J. Appl. Phys.* **54**, 2137 (1983).
[7.2] A. S. Argon and H. Y. Kuo, *J. Non-Crys. Sol.* **37**, 241 (1980).
[7.3] J. M. Pelletier, *J. Alloys Comp*. **393**, 223 (2005).
[7.4] M. H. Cohen and D. Turnbull, *J. Chem. Phys.* **31**, 1164 (1959).
[7.5] F. Spaepen, *Acta Metall*. **25**, 407 (1977).
[7.6] A. I. Taub and F. Spaepen, *Acta Metall*. **28**, 1781(1980).
[7.7] Z. Wang, H. B. Yu, P. Wen, H. Y. Bai and W. H. Wang, *J. Phys.*: *Condens. Matter* **23**, 142202 (2011).
[7.8] H. B. Yu, K. Samwer, Y. Wu and W. H. Wang, *Phy. Rev. Lett*. **109**, 095508 (2012).
[7.9] A. Bartsch, K. Rätzke, A. Meyer and F. Faupel, *Phy. Rev. Lett*. **104**, 195901 (2010).
[7.10] F. Spaepen, *Acta Metall*. **25**, 407 (1977).
[7.11] A. S. Argon, *Acta Metall*. **27**, 47 (1979).
[7.12] A. S. Argon and L. T. Shi, *Acta Metall*. **4**, 499 (1983).
[7.13] M. Heggen, F. Spaepen and M. Feuerbarcher, *J. Appl. Phys*. **97**, 033506 (2005).
[7.14] W. Flügge, *Viscoelasticity*, Springer-Verlag, (1975).
[7.15] W. N. Findley and F. A. Davis, *Creep and relaxation of nonlinear viscoelastic materials, with an introduction to linear viscoelasticity*, North-Holland Publishing Company, (1976).
[7.16] A. S. Nowick and B. S. Berry, *Anelastic relaxation in crystalline solids*, Academic Press, (1972).
[7.17] A. S. Argon and H. Y. Kuo, *Mater. Sci. Eng*. **39**, 101 (1979).
[7.18] P. Schall, D. Weitz, F. Spaepen, *Science* **318**, 1895 (2007).
[7.19] P. S. Steif, F. Spaepen and J. W. Hutchinson, *Acta Metall*. **30**, 447 (1982).
[7.20] V. V. Bulatov and A. S. Argon, *Modelling Simul. Mater. Sci. Eng*. **2**, 167 (1994).
[7.21] K-W. Park, C-M. Lee, M. Wakeda, Y. Shibutani, M. L. Falk and J-C. Lee, *Acta Mater*. **56**, 5440 (2008).
[7.22] J. Schroers and W. L. Johnson, *Phy. Rev. Lett*. **93**, 255506 (2004).
[7.23] L. F. Liu, L. H. Dai, Y. L. Bai, B. C. Wei and J. Eckert, *Mater. Chem. Phy*. **93**, 174 (2005).
[7.24] J. D. Eshelby, *Proc. R. Soc*. **252**, 561 (1959).

[7.25] D. C. Hofmann, J.-Y. Suh, A. Wiest, G. Duan, M.-L. Lind, M. D. Demetriou and W. L. Johnson, *Nature* **451**, 1085 (2008).

[7.26] L. Y. Chen, Z. D. Fu, G. Q. Zhang, X. P. Hao, Q. K. Jiang, X. D. Wang, Q. P. Cao, H. Franz, Y. G. Liu, H. S. Xie, S. L. Zhang, B. Y. Wang, Y. W. Zeng and J. Z. Jiang, *Phy. Rev. Lett.* **100**, 075501 (2008).

[7.27] N. Zheng, R. T. Qu, S. Pauly, M. Calin, T. Gemming, Z. F. Zhang and J. Eckert, *Appl. Phy. Lett.* **100**, 141901 (2012).

Appendix A

The first two sections in this appendix comprise a derivation of of Eqn. (2.2) and (2.21), including their physical meanings. The effective stress and strain rate in Eqn. (2.2) are discussed in Section A.1, and the activation energy in Eqn. (2.21)[1–3] is discussed in Section A.2. The Einstein summation convention[4] is used in both sections.

A.1 EFFECTIVE STRESS AND STRAIN RATE

It has been proposed by Huber[5] that a solid flows when the second stress invariant, J_2, exceeds a critical value. According to von Mises,[6] J_2 is given by:[5–8]

$$J_2 = \frac{1}{2}[(\sigma_1 - p)^2 + (\sigma_2 - p)^2 + (\sigma_3 - p)^2] = \frac{1}{2} S_{ij} S_{ij}, \tag{A.1}$$

where σ_1, σ_2 and σ_3 are the principal stresses, p the mean stress, $p = \frac{\sigma_{kk}}{3} = \frac{\sigma_1 + \sigma_2 + \sigma_3}{3}$, and S_{ij} the deviatoric stress, $S_{ij} = \sigma_{ij} - \frac{1}{3}\delta_{ij}\sigma_{kk}$, where δ_{ij} is the Kronecker delta.

Hencky[9] added a physical interpretation to von Mises' criterion: J_2 is proportional to the elastic distortion energy: when it reaches a critical value, k^2, flow begins. The distortion energy is the strain energy per unit volume involved in a shape change, as opposed to a change in volume.[7] The criterion, $J_2 = k^2$, yields an expression for the effective stress, $\bar{\sigma}$, (often also called the equivalent stress or von Mises stress):

$$\bar{\sigma} = \sqrt{\frac{3}{2} S_{ij} S_{ij}} \,, \tag{A.2}$$

such that yield occurs when $\bar{\sigma} = \sigma_y$, where σ_y is the tensile yield strength. Equation (A.2) allows for calculating the effective stress for multiaxial stress states. For example, in the case of a uniaxial test, the only stress component in the stress tensor is σ_{11}, yielding the effective stress, $\bar{\sigma} = \sigma_{11}$.

For a pure shear condition, such as in a torsion experiment, the effective shear stress for flow can be obtained. A schematic illustration of the stress state is given in Fig. A.1.

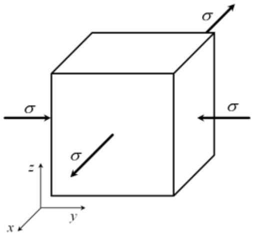

Figure A.1 Stress states for the pure shear condition. Tensile and compressive stresses (σ) are applied along the *x* and *y* axes, respectively.

When biaxial stress, $\sigma_{11} = -\sigma_{22} = \sigma$, is applied, shown in Fig. A.1, the maximum shear stress acting on the plane that is 45° inclined with respect to the principal axes is equal to the principal stress, $\sigma = \tau$. S_{ij} for this condition is given by:

$$S_{ij} = \begin{pmatrix} \sigma - (\sigma - \sigma + 0)/3 & 0 & 0 \\ 0 & -\sigma - (\sigma - \sigma + 0)/3 & 0 \\ 0 & 0 & 0 - (\sigma - \sigma + 0)/3 \end{pmatrix}, \tag{A.3}$$

and therefore, the effective stress in a pure shear state in terms of the shear stress, using Eqn. (A.2), is given by:

$$\bar{\sigma} = \sqrt{\frac{3}{2}(2\tau^2)} = \sqrt{3}\,\tau \,. \tag{A.4}$$

Since for a uniaxial test $\bar{\sigma} = \sigma_{11}$, as discussed above, the von Mises equivalent shear stress, $\bar{\tau}$, which is the pure shear stress in Eqn. (A.4) is given by:

$$\bar{\tau} = \frac{\bar{\sigma}}{\sqrt{3}} \,. \tag{A.5}$$

The effective strain rate for uniaxial and pure shear condition can also be derived. In order to find the relationship between these two states, the power (the rate of work) dissipated during flow, *dW/dt,* is used, assuming that $dW/dt = \sigma_{11}\,\dot{\varepsilon}_{11}$ for a uniaxial test.[8] The power is the product of the effective stress, $\bar{\sigma}$, and the effective strain rate, $\dot{\bar{\varepsilon}}$. Taking the second invariant form for the strain rate: $\dot{\bar{\varepsilon}} = \sqrt{\alpha\,\dot{\varepsilon}_{ij}\,\dot{\varepsilon}_{ij}}$, as shown for $\bar{\sigma}$ in Eqn. (A.2), the power is given by:

$$\frac{dW}{dt} = \bar{\sigma}\,\dot{\bar{\varepsilon}} = \sqrt{\frac{3}{2}S_{ij}\,S_{ij}} \cdot \sqrt{\alpha\,\dot{\varepsilon}_{ij}\,\dot{\varepsilon}_{ij}} \;, \tag{A.6}$$

where $\dot{\varepsilon}_{ij}$ is the strain rate tensor and α is a multiplier, to be determined. For a constant volume of a material during flow in a uniaxial test, $\dot{\varepsilon}_{ij}$ in Eqn. (A.6) is given by:

$$\dot{\varepsilon}_{ij} = \begin{pmatrix} \dot{\varepsilon}_{11} & 0 & 0 \\ 0 & -\dot{\varepsilon}_{11}/2 & 0 \\ 0 & 0 & -\dot{\varepsilon}_{11}/2 \end{pmatrix}, \tag{A.7}$$

where $\dot{\varepsilon}_{11}$ is the uniaxial strain rate. For the uniaxial condition, noting that $\dot{\bar{\varepsilon}} = \dot{\varepsilon}_{11}$ from the assumption for *dW/dt,* α = 2/3 is obtained using Eqn. (A.6) and (A.7), yielding:

$$\dot{\bar{\varepsilon}} = \sqrt{\frac{2}{3}\dot{\varepsilon}_{ij}\,\dot{\varepsilon}_{ij}}\ . \tag{A.8}$$

Noting that the only strain components in the strain tensor for pure shear state are $\dot{\varepsilon}_{12} = \dot{\varepsilon}_{21}$, the effective shear strain rate, $\dot{\bar{\gamma}}$ is defined by $\dot{\varepsilon}_{12} = \dot{\varepsilon}_{21} = \dot{\bar{\gamma}}/2$ and is obtained using Eqn. (A.8):

$$\dot{\bar{\gamma}} = \sqrt{3}\,\dot{\bar{\varepsilon}}\ . \tag{A.9}$$

Combining Eqn. (A.5) and (A.9), noticing that the shear viscosity is the resistance of a fluid to flow, $\eta \equiv \frac{\bar{\tau}}{\dot{\bar{\gamma}}}$, an expression for shear viscosity is obtained in terms of the experimentally measurable properties, such as the uniaxial stress, σ, and strain rate, $\dot{\varepsilon} = \frac{d\varepsilon}{dt}$:

$$\sigma = 3\eta\frac{d\varepsilon}{dt}\ . \tag{2.2}$$

A.2 STRAIN ENERGY STORED BY AN ESHELBY INCLUSION[10]

The Eshelby inclusion theory[10] expresses a relation between the strain of an inclusion in an elastic medium and the resulting total elastic strain energy. This energy is calculated in three steps. First, a local inclusion of volume, Ω, is cut from the matrix, which is stress free, and undergoes transformation strain. Next, surface traction is applied to restore the strained inclusion elastically to its original shape and to embed it back into the hole in the matrix. Up to this step, the total strain is zero because the transformation strain is canceled out by the strain reversal due to surface traction. Finally, the material is rejoined and is allowed to relax by removing the surface traction. Since the inclusion is now constrained by the matrix, the transformation strain is reduced, as expressed in terms of a forth order tensor, A_{ijkl}:[10,11]

$$\varepsilon_{ij}^{C} = A_{ijkl}\,\varepsilon_{kl}^{T}\,. \qquad \text{(A.10)}$$

ε_{kl}^{T} is the transformation strain tensor in a stress-free state and ε_{ij}^{C} is the constrained strain tensor.

For an ellipsoidal inclusion in a homogenous matrix, since the matrix causes the strain of the inclusion to be smaller than the unconstrained transformation strain, the difference between those strains, $(\varepsilon_{kl}^{C} - \varepsilon_{kl}^{T})$, results in elastic strains, $\varepsilon_{kl}^{el.}$, and stresses, σ_{ij} that are uniform inside the inclusion.[10] An expression for the stress tensor is obtained by applying Hooke's law:

$$\sigma_{ij} = C_{ijkl}\,\varepsilon_{kl}^{el.} = C_{ijkl}\,(\varepsilon_{kl}^{C} - \varepsilon_{kl}^{T})\,, \qquad \text{(A.11)}$$

where C_{ijkl} is the material's elastic stiffness and $\varepsilon_{kl}^{el.} = \varepsilon_{kl}^{C} - \varepsilon_{kl}^{T}$. For an isotropic material, such as for metallic glasses, the stress tensor given in Eqn. (A.11) can be rewritten as: [5,7,10,11]

$$\sigma_{ij} = 2\,\mu(\varepsilon_{ij}^{C} - \varepsilon_{ij}^{T}) + \lambda\,\delta_{ij}\,(\varepsilon_{kk}^{C} - \varepsilon_{kk}^{T})\,, \qquad \text{(A.12)}$$

where λ and μ are the Lamé first and second parameters,[5,7,11] respectively.

The net resulting strain energy, *W*, of a material due to an inclusion that has experienced transformation strain is obtained by integrating the elastic strain energy per unit volume over the total volume of a material, *V*:[10,11]

$$W = \frac{1}{2}\int_{V} \sigma_{ij}\,\varepsilon_{ij}^{el.}\,dV = -\frac{1}{2}\sigma_{ij}\,\varepsilon_{ij}^{T}\,\Omega\,. \qquad \text{(A.13)}$$

W is equal to the superposed work done during the three steps discussed above, and it includes the energy increase by the elastic strain existing inside and outside the inclusion.

For a spherical inclusion, such as for an STZ, an analytical solution to the Eshelby problem has been obtained:[10,11]

$$A_{ijkl} = \frac{5\nu - 1}{15(1-\nu)} \delta_{ij} \delta_{kl} + \frac{4 - 5\nu}{15(1-\nu)} (\delta_{ik} \delta_{jl} + \delta_{il} \delta_{jk}) . \tag{A.14}$$

Therefore, the strain energy due to the shear transformation of the inclusion can be obtained by incorporating the transformation strain tensor into Eqn. (A.10) through (A.13).

For example, when a spherical inclusion experiences engineering shear strain outside the matrix, γ_0^T, the shear strain components of the transformation strain tensor are $\varepsilon_{12}^T = \varepsilon_{21}^T = \gamma_0^T / 2$. From Eqn. (A.10), the constrained shear strains are obtained: $\varepsilon_{12}^C = \varepsilon_{21}^C = \frac{4-5\nu}{15(1-\nu)} \gamma_0^T$,[10] where ν is Poisson's ratio. Thus, the engineering constrained shear strain is $\gamma_0^C = \frac{2(4-5\nu)}{15(1-\nu)} \gamma_0^T$, as discussed in Section 2.2.1. The strain components are incorporated into Eqn. (A.12) and (A.13) to yield the corresponding elastic stress and energy, and the resulting strain energy due to the sheared inclusion is $W_{shear} = \frac{7-5\nu}{30(1-\nu)} \mu (\gamma_0^T)^2 \Omega$, which is the first term in the activation energy.[1–3]

The strain energy resulting from expansion or contraction can also be obtained in a similar fashion. When a spherical inclusion undergoes uniform volume change (Δ*V*), $\varepsilon_0^T = \Delta V / V$ is the volumetric strain due to the dilatation or thermal expansion, and the normal strain components in the transformation strain tensor is $\varepsilon_{ij}^T = \delta_{ij} (\varepsilon_0^T / 3)$. Equation (A.10) and (A.14) yield the constrained principal strains,[10] $\varepsilon_{11}^C = \varepsilon_{22}^C = \varepsilon_{33}^C = \frac{1+\nu}{3(1-\nu)} \frac{\varepsilon_0^T}{3}$, and the resulting strain energy is obtained using Eqn. (A.12) and (A.13): $W_{dilatation} = \frac{2(1+\nu)}{9(1-\nu)} \mu (\varepsilon_0^T)^2 \Omega$. Since it has been experimentally observed in bubble rafts that the dilatancy factor, $\bar{\beta} = \varepsilon_0^T / \gamma_0^T$, is about equal to 1,[1–3] the expression is rewritten as $W_{dilatation} = \frac{2(1+\nu)}{9(1-\nu)}\mu(\overline{\beta}\gamma_0^T)^2\Omega$, which is the second term in the activation energy, in Eqn. (2.21):

$$\Delta E_a = \left[\left(\frac{(7-5\nu)}{30(1-\nu)} + \frac{2(1+\nu)}{9(1-\nu)}\overline{\beta}^2\right)\gamma_0^T + \frac{1}{2}\frac{\overline{\sigma}_{STZ}}{\mu}\right]\mu\gamma_0^T\Omega \cdot \tag{2.21}$$

Appendix B

B CODES FOR DIRECT SPECTRUM ANALYSIS[12]

B.1 INTRODUCTION

In this appendix, computation codes written for direct spectrum analysis (DSA)[12] to obtain relaxation time spectra, from quasi-static, bend-stress relaxation (**B.B**) and cantilever bending (**B.C**), and from dynamic data (**B.D**), are detailed. The procedure is the same for the three measurement methods except where denoted in bold. DSA employs a least-squares fit of anelastic relaxation curves using large numbers (30 – 100) of fitting parameters (See Chapter 3).

Comments explain the role of technically important commands, which may need to be modified, depending on experimental conditions, e.g., experimental time scale or boundary conditions. While the codes are written in ‘Calibri’ font, comments are written in ‘Times New Roman’ font in the parentheses between asterisk symbols, i.e., (* and *). Prior to reading this appendix, it is recommended that Chapter 3 be read first, since details on DSA, including equations employed for the analyses, as well as examples tested with simulated data, are described in it.

B.2 THE CODES

```
ClearAll
Amplnewcurvefit[data_,coeflist_,tau_,tauexp_, initcoef_:{1},weights_:{1}]:=
```

(***Amplnewcurvefit** executes the fit for DSA. In the square bracket, [], sets of variables to be included prior to performing DSA are written. The name of each set is followed by underscore, e.g., **name_**. The sets of variables are:

data_ is the experimental (or simulated) data set. It consists of two columns: the time (t) and normalized anelastic strain $(\varepsilon_{an}(t)/\varepsilon_{el}^{0})$ for quasi-static data, and of the angular frequency (ω) and loss modulus ($E''(\omega)$) for dynamic data. The present author used an Excel© workbook (97-2003 version: '*Datafile.xls*'), in which the first and second columns consist of t (or ω) and the corresponding $(\varepsilon_{an}(t)/\varepsilon_{el}^{0})$ (or ($E''(\omega)$)), respectively. This workbook will be imported below. When using Mathematica© with this data set instead of an Excel© workbook, the data should be given between brackets, e.g., $\{\{t_1, (\varepsilon_{an}(t_1)/\varepsilon_{el}^{0})\}, \{t_2, (\varepsilon_{an}(t_2)/\varepsilon_{el}^{0})\}, \ldots,\{t_n, (\varepsilon_{an}(t_n)/\varepsilon_{el}^{0})\}\}$ for quasi-static data, where t_j and $(\varepsilon_{an}(t_j)/\varepsilon_{el}^{0})$ are the measurement time and corresponding anelastic strain, respectively, measured up to t_n.

coeflist_ is the list of fitting parameters that will be determined from DSA. These parameters are used to determine the relaxation-time spectrum. Using Mathematica©, their list is given in brackets: {a_0, a_2, …, a_{nmax}}, where the a_i are the individual fitting parameters, as described on page 156. The total number of the parameters on the list is ($nmax$+1).

tau_ is τ_{min} and **tauexp_** is $\Delta\ln\tau$ in Eqn. (3.12), which have specific values that will be stated below.

initcoef_:{1} is the list of initial guesses for each fitting parameter in **coeflist_** above. Therefore, the number of initial guesses is the same as that of **coeflist_**. Using Mathematica©, the list of these initial guesses is given in brackets, {}, separated by commas, as described on page 157. For example, when the number of parameters is 3 and the initial guess for each parameter is 0.01, **initcoef_:{1}** is given by: {0.01, 0.01, 0.01}. The default value of **initcoef_:{1}** is '1' for each fitting parameter, as indicated in **:{1}** following the underscore: if individual values of the initial guesses are not specified when DSA is executed, fitting will be performed automatically with the initial guesses of '1' for individual variables in **coeflist_**.

weights_:{1} is the list of weighting factors that allow for weighting individual data points during the fit. Therefore, the number of these factors is the same as that of the points in **data_**. Their numerical values are also given in brackets, {}, separated by commas. The default value of **weights_:{1}** is '1' for each data point, as indicated in **:{1}** following the underscore: if individual values of these weighting factors are not specified when DSA is executed, fitting will be performed by equally weighting each data point in **data_**. The present author did not use specific weighting factors for DSA, but the default value, '1'.

Further details on these variables are explained below.*)

```
Module [{},
s=OpenWrite[];
WriteString[s,"param tau;param tauexp;param N;param nvar;
set I := 0..nvar;set J := 1..N;param t{1..N};
param rtot{J};param Weights{J};
var a{i in I};
var tot{j in J} = sum{i in 0..(nvar-1)} a[i]^2*(exp(-t[j]/(tau*(tauexp)^i)));
var tot2{j in J} = tot[j] +a[nvar];
```

(*The first six lines do not have to be modified prior to performing DSA with different data sets. In these lines, expressions for the number of fitting parameters, **nvar** + 1, and the j^{th} time (or angular frequency) point, t_j (or ω_j), where **j** is an integer between 1 and **N** (**N** = the number of data points), are written. These values are automatically set when the fit is executed with the fitting parameters and data set in the square bracket following **Amplnewcurvefit** on page 158. The last two lines, however, may need to be modified depending on the data set employed for DSA. These two lines contain the fitting equation for the anelastic strain for bend-stress relaxation data (**B.B**). For cantilever and dynamic data, use the expressions below in **B.C** and **B.D**, respectively:

B.B Bend-stress relaxation

```
var tot{j in J} = sum{i in 0..(nvar-1)} a[i]^2*(exp(-t[j]/(tau*(tauexp)^i)));

var tot2{j in J} = tot[j] +a[nvar];
```

B.C Cantilever bending

```
var tot{j in J} = sum{i in 0..(nvar-2)} a[i]^2*(1-exp(-t[j]/(tau*(tauexp)^i)));

var tot2{j in J} = tot[j] + a[nvar-1]^2*t[j] + a[nvar];
```

B.D Dynamic (Loss modulus)

```
var tot{j in J} = sum{i in 0..(nvar)}

a[i]^2*((t[j]*(tau*(tauexp)^i))/(1+(t[j]*(tau*(tauexp)^i))^2));

var tot2{j in J} = tot[j];
```

The fitting equation for the anelastic strain at t_j (or ω_j), $j = 1,\ldots,n$, where n is the number of data points, is given in the expression for **tot2{j in J}**. **tot[j]** is equal to:

$$\textbf{B.B:}\ \sum_{i=0}^{N-1} a_i^{\,2} \exp[t_j / \tau_i],$$

$$\textbf{B.C:}\ \sum_{i=0}^{N-2} a_i^{\,2} (1 - \exp[t_j / \tau_i]),$$

$$\textbf{B.D:}\ \sum_{i=0}^{N} a_i^{\,2} \frac{\omega_j \tau_i}{1 + \omega_j^{\,2} \tau_i^{\,2}},$$

where (N + 1 = **nvar** + 1) is the total number of fitting parameters, a_i = **a[i]**, $i = 0,\ldots,N$, are the fitting parameters, a_N = **a[nvar]** for **B.B** and **B.C** is equal to A in Eqn. (3.11), and **a[nvar-1]^2*t[j]** for **B.C** is the linear term, $B\,t$, in Eqn. (3.11.a). (**tot[j]** + **a[nvar]**) for **B.B**, and (**tot[j]** + **a[nvar-1]^2*t[j]** + **a[nvar]**) for **B.C** correspond to Eqn. (3.11.a) and Eqn. (3.11 b), respectively. For **B.D**, **tot[j]** is equal to Eqn. (3.15.b). Note that while the summation in **B.D** is up to (N), those in **B.B** and **B.C** are up to (N-1) and (N-2), respectively: A = **a[nvar]** for **B.B** and **B.C**, and $B\,t$ = **a[nvar-1]^2*t[j]** for **B.C** are listed separately*)

```
minimize Obj:

sum{j in J} ((tot2[j]-rtot[j])*Weights[j])^2;\n\n
```

(***Amplnewcurvefit** fits the experimental (or simulated) data by varying the unknown parameters, a_i, B and A in Eqn. (3.11), through a number of iterations, minimizing sum of the squares of the residuals that is given by:

$$\sum_{j=1}^{n}(y_j - h(t_j))^2 , \tag{B.1}$$

where y_j is the j^{th} value of the experimental (or simulated) data, j = 1,…,n, and $h(t_j)$ is the fit value at t_j. In the preceding commands, **rtot[j]** and **tot2[j]** are equal to y_j and $h(t_j)$ in Eqn. (B.1), respectively. **Weights[j]** allows for weighting individual data points by multiplying them by the residuals, set prior to performing DSA. The sum to be minimized is then:

$$\sum_{j=1}^{n}((y_j - h(t_j)) \times w_j)^2 , \tag{B.2}$$

where w_j = **Weights[j]** is the weighting factor for the j^{th} residual. As explained above (See the description of "**weights_:{1}**" above), if **weights_:{1}** is not set, each weighting factor is '1', and therefore, DSA is performed by equally weighting each data point in **data_**.*)

```
subject to con1 {i in 0..(nvar-2)}:\n

1 >= a[i] >= -1;\n

subject  to con2:\n

1 >= a[nvar] >= -1;\n
```

subject to con3:\n

1 >= a[nvar-1] >= -1;\n

B.B Bend-stress relaxation	subject to con1 {i in 0..(nvar-2)}:\n 1 >= a[i] >= -1;\n subject to con2:\n 1 >= a[nvar] >= -1;\n subject to con3:\n 1 >= a[nvar-1] >= -1;\n
B.C Cantilever bending	subject to con1 {i in 0..(nvar-2)}:\n 1 >= a[i] >= -1;\n subject to con2:\n 1 >= a[nvar] >= -1;\n subject to con3:\n 1 >= a[nvar-1] >= -1;\n
B.D Dynamic (Loss modulus)	subject to con1 {i in 0..(nvar-2)}:\n 0.4 >= a[i] >= -0.4 ;\n subject to con2:\n 0.4 >= a[nvar] >= -0.4 ;\n subject to con3:\n 0.4 >= a[nvar-1] >=-0.4 ;\n

(*The preceding commands allow for constraining individual fitting parameters in **coeflist_** by imposing upper/lower limits on them. In order for the user to be able to apply the constraints to the fitting parameters separately, a_i, B and A in Eqn (3.11), when necessary, the constraints for the parameters are separately written in **con1**, **con2** and **con3**, respectively. For example, in the case of cantilever bending data (**B.C**), commands written in **con1** indicate that all **a[i]**, which correspond to a_i in **B.C:** $\sum_{i=0}^{N-2} a_i^2 (1-\exp[t/\tau_i])$, are constrained within the limits of ± 1. Likewise, **a[nvar]** and **a[nvar-1]**, which correspond to A and B in Eqn. (3.11.a), respectively, are constrained within ±1 as well, as shown in **con2** and **con3**. When calculating the relaxation-time spectrum, the a_i^2 are normalized by $\Delta \ln \tau$ that is equal to $\ln[\tau_{\max}/\tau_{\min}]/(N-1)$, as given in Eqn. (3.13): The current upper/lower limits on **a[i]** for quasi-static and dynamic data, ± 1 and ± 0.4, corresponds to ~ 3 and ~ 0.8 in the spectrum, respectively, which are not expected to be exceeded.*)

```
data;\n\n"];
datalen=Length[data];
nmax=Length[coeflist];


If[Length[weights]=== 1 , w2=Table[1,{i,1,datalen}];,w2=weights;];
If[Length[initcoef]=== 1 ,icoef=Table[1,{i,1,nmax-2}];,icoef=initcoef;];
WriteString[s,"#",Length[initcoef]," ",Length[weights],"\n"];
WriteString[s,"var a :=\n"];
```

```
For[i=0,i<Length[icoef],i++,   WriteString[s,i," ",icoef[[i+1]],"\n"];]
WriteString[s," ;\n"];
WriteString[s,"param tau:= ",tau," ;\n"];
WriteString[s,"param N:= ",datalen," ;\n"];
WriteString[s,"param nvar:= ",nmax-1," ;\n"];
WriteString[s,"param tauexp:= ",tauexp," ;\n"];
```

(*The preceding commands do not have to be modified prior to performing DSA with different data sets. These commands create the variables (default weighting factors and initial guesses, which are ‘1’ for all the variables unless specified, fitting parameters (a_i), τ_{min} in Eqn. (3.12) and the total number of fitting parameters) in the temporary directory. These variables in the directory are imported by AMPL to perform the fit.*)

```
WriteString[s,"option ipopt_options 'tol=1e-001      ';\n"];
```

(*The nonlinear solver IPOPT employed in DSA allows for fitting data using options that can be adjusted for the algorithm (See http://www.coin-or.org/Ipopt/documentation/). In the current study, tolerance = **tol** may need to be varied for **B.D** (See Chapter 3), which terminates the fit when the convergence condition given in Eqn. (3.19) is satisfied:

$$tolerance > \left|\sum_j (y_j - (h(\omega_j))_k)^2 - \sum_j (y_j - (h(\omega_j))_{k+1})^2\right| / \left(1 + \left|\sum_j (y_j - (h(\omega_j))_k)^2\right|\right), \qquad (3.19)$$

where y_j is the j^{th} value of the experimental (simulated) data, $(h(\omega_j))_k$ is the fit value at ω_j for k^{th} iteration, respectively. The tolerance value can be varied from ‘0’ to ‘+inf’, by varying the number written above: 1e-001. In our study, DSA is performed with the convergence tolerance value of 1e-001 for **B.B** and **B.C**, and from 1e-000 to 1e-006 for **B.D** (See Chapter 3), beyond which the results do not vary. For **B.B** and **B.C**, the result is insensitive to the tolerance value.*)

```
s1 = OpenWrite[];
inp2=Close[s1];
s2 = OpenWrite[];
out1=Close[s2];
outw=Table[Join[data[[i]],{w2[[i]]}],{i,1,datalen}];
Export[inp2,outw,"Table"];
WriteString[s, "read {i in 1..N}(t[i],rtot[i],Weights[i])"," < ",inp2,";\n"];
WriteString[s,"option solver ipopt;\n"];
WriteString[s,"printf \"AMPL/Minos is solving for %d parameters\",nvar;\nsolve;\n"];
WriteString[s,"print {i in 0..nvar}:a[i]  >",out1,";\nquit;\n"];
inp1=Close[s];
Run["ampl","<",inp1];
tempa=Import[out1,"Table"];
tr1=Table[coeflist[[i]] ->tempa[[i,1]],{i,1,nmax}]
];
```

(*The preceding commands do not have to be modified. These are written for AMPL to convert the variables set on page 158 in the square bracket following “**Amplnewcurvefit**” into the AMPL format, and to export the fit results into the temporary directory. These fit results are imported on page 159.*)

```
data=Import["Datafile.xls"];
```

(*Import the experimental/simulated data set for **data** summarized in an Excel© workbook.*)

```
coeflist[nmax_]:=Table[Subscript[a,n],{n,0,nmax}];
```

(*A list of fitting parameters for **coeflist_** is set as a_n, $n = 0,\ldots,nmax$, where $(nmax+1)$ is the total number of parameters: For bend-stress relaxation data (**B.B**), a_0 to $a_{(nmax-1)}$ are the ε_i and a_{nmax} is A in Eqn. (3.11.b). In the case of cantilever bending data (**B.C**), a_0 to $a_{(nmax-2)}$ are the ε_i, $a_{(nmax-1)}$ is B and a_{nmax} is A in Eqn. (3.11.a). For loss modulus data (**B.D**), a_0 to a_{nmax} are the E_i in Eqn. (3.15.b).*)

```
taumin=0.1;
taumax=4*10^4;
```

(*The minimum and maximum time constants, i.e., τ_{min} and τ_{max} in Eqn. (3.12), are set as 0.1 and 4×10^4 *sec.*, respectively. These values can be varied depending on the experimental time scale (See Chapter 3).*)

```
nvar=30;
```

(*The number of exponents in the summation in Eqn. (3.11) (or that of Debye peaks in Eqn. (3.15.b) for **B.D**) is set as 30. Note that, for example, when '**nvar**' is set as 30, (*N*-1) for **B.B**, (*N*-2) for **B.C** and (*N*) for **B.D** in the summation are equal to 30, 29 and 31, respectively.*)

```
i01 =Table[N[0.01],{i,1,(nvar+1)}];
```

(*The initial guesses of the fitting parameters are set as 0.01 and these numerical values are listed in the table, labeled as '**i01**'. These values can be varied by creating the table with a different initial guess for each parameter. Since the number of exponents is labeled as '**nvar**', and '**coeflist[nmax_]**' includes the constant, *A*, in Eqn. (3.11), the total number of initial guesses is equal to **(nvar+1)** for **B.B**, as indicated above. When performing DSA with cantilever bending (**B.C**) and loss modulus data (**B.D**), **(nvar+1)** needs to be replaced by **(nvar+2)** and **(nvar)**, respectively, since there is an extra linear term, $B\,t$, in Eqn. (3.11.a), and there is no *A* term in Eqn. (3.15.b).*)

```
tautable=Table[taumin*E^((n (Log[taumax]-Log[taumin]))/(nvar-1)),{n,0,(nvar-1)}];
```

(*A table of relaxation time constants, τ_i, is set such that the τ_i are logarithmically spaced from $\tau_{min.}$ to $\tau_{max.}$, as given in Eqn. (3.12), depending on the experimental time scale (See Chapter 3).*)

```
myamplfit=Amplnewcurvefit[data[[1]],coeflist[nvar],taumin,E^((Log[taumax]-Log[taumin])/(nvar -1)),i01];
```

B.B Bend-stress relaxation

```
coeflistnorm=(coeflist[nvar -1]/.myamplfit)^2/(Log[taumax]-Log[taumin])/(nvar -1);
coefA=(coeflist[nvar]/.myamplfit)[[Length[coeflist[nvar]]]];
coeflistnormFinal=Table[coeflistnorm[[i]],{i,1,Length[coeflistnorm]+1}]/.x_/;x==coeflistnorm[[Length[coeflistnorm]+1]]->coefA;
```

B.C Cantilever bending

```
coeflistnorm=(coeflist[nvar -2]/.myamplfit)^2/(Log[taumax]-Log[taumin])/( nvar -1);
coefsqrtB=(coeflist[nvar -1]/.myamplfit)[[Length[coeflist[nvar -1]]]];
coefA=(coeflist[nvar]/.myamplfit)[[Length[coeflist[nvar]]]];
coeflistnormFinal1=Table[coeflistnorm[[i]],{i,1,Length[coeflistnorm]+1}]/.x_/;x==coeflistnorm[[Length[coeflistnorm]+1]]->(coefsqrtB)^2;
coeflistnormFinal=Table[coeflistnormFinal1[[i]],{i,1,Length[coeflistnormFinal1]+1}]/.x_/;x== coeflistnormFinal1[[Length[coeflistnormFinal1]+1]]->coefA;
```

B.D Dynamic (Loss modulus)

```
coeflistnormFinal=(coeflist[nvar -1]/.myamplfit)^2/(Log[taumax]-Log[taumin])/( nvar -1);
```

(*DSA is executed by **Amplnewcurvefit[]**, where the square brackets contains experimental/simulated data (**data[[1]]**), fitting parameters (**coeflist[nvar]**), τ_{min} (**taumin**), $\Delta \ln \tau$, calculated as (**E^((Log[taumax]-Log[taumin])/(nvar-1))**), and a list of initial guesses for the fitting parameters (**i01**). The results of the current fit are labeled as “**myamplfit**”.*)

```
coeflistnorm=(coeflist[nvar -1]/.myamplfit)^2/(Log[taumax]-Log[taumin])/( nvar -1);
coefA=(coeflist[nvar]/.myamplfit)[[Length[coeflist[nvar]]]];
coeflistnormFinal=Table[coeflistnorm[[i]],{i,1,Length[coeflistnorm]+1}]/.x_/;x==coeflistnorm[[Le
ngth[coeflistnorm]+1]]->coefA;
```

(*Fitting parameters obtained from DSA are listed in ‘**coeflistnormFinal**’. These values are used to calculate the fit and R^2 below. The lists of values in ‘**coeflistnorm**’ for **B.B** and **B.C**, and that in ‘**coeflistnormFinal**’ for **B.D**, correspond to the relaxation time spectrum, and are calculated as ($a_i^2/\Delta\ln\tau$), as given in Eqn. (3.13), where a_i are the parameters obtained from DSA and $\Delta\ln\tau = \ln[\tau_{\max}/\tau_{\min}]/(N-1)$ given in Eqn. (3.12).*)

```
displacement=Table[data[[1]][[i,2]],{i,1,Length[data[[1]]]}];
meandisplacement=Mean[displacement];
difference1=displacement-meandisplacement;
sumsquare=Sum[difference1[[i]]^2,{i,1,Length[difference1]}];
time=Table[data[[1]][[i,1]],{i,1,Length[data[[1]]]}];
NIcurve[t_,nmax_]:=Sum[(Subscript[a,n])^2(Exp[-t/(taumin*(E^((Log[taumax]-
Log[taumin])/(nvar -1)))^n)]),{n,0,nmax-1}]+Subscript[a,nmax];
NIcurvetable=Table[NIcurve[time[[i]],nvar]/.myamplfit,{i,1,Length[time]}];
```

```
difference2=NIcurvetable-displacement;

residualsumsquare=Sum[difference2[[i]]^2,{i,1,Length[difference2]}];

rsquared=1-(residualsumsquare/sumsquare);
```

B.B Bend-stress relaxation	NIcurve[t_,nmax_]:=Sum[(Subscript[a,n])^2(Exp[-t/(taumin*(E^((Log[taumax]-Log[taumin])/(nvar -1)))^n)]),{n,0,nmax-1}]+Subscript[a,nmax];
B.C Cantilever bending	NIcurve[t_,nmax_]:=Sum[(Subscript[a,n])^2(Exp[-t/(taumin*(E^((Log[taumax]-Log[taumin])/(nvar -1)))^n)]),{n,0,nmax-2}]+ Subscript[a,nmax-1] t+Subscript[a,nmax];
B.D Dynamic (Loss modulus)	NIcurve[t_,nmax_] :=Sum[(Subscript[a,n])^2 ((t taumin E^((n*(Log[taumax]-Log[taumin]))/(nvar -1)))/(1+(t taumin E^((n*(Log[taumax]-Log[taumin]))/(nvar -1)))^2)),{n,0,nmax}];

(*R^2 = **rsquared** ≡ 1 - (sum of the squares of the residuals/the total sum of squares) is calculated using Eqn. (3.15): $R^2 \equiv 1 - \left(\sum_{j=1}^{n} (y_j - h(t_j))^2 / \sum_{j=1}^{n} (y_j - \bar{y})^2 \right)$, where y_j is the j^{th} value of the experimental (or simulated) data, which comprise n data points, $h(t_j)$ is the fit value at t_j, and $\bar{y}$ is the mean of the data. **NIcurve[t_,nmax_]** written in the preceding expression is for **B.B**. Replace the expression with those for **B.C** and **B.D** given above:*)

```
FitparameterFinal=Table[{tautable[[x]],coeflistnormFinal[[x]],rsquared},{x,1,(nvar +1)}];

Export["Outputfile1.xls ",FitparameterFinal]
```

```
maxpower=7;

minpower=-2;

time2=Table[10^i,{i,minpower, maxpower,0.005}];

NIcurvetable2=Table[{time2[[i]],NIcurve[time2[[i]],(nvar)]/.myamplfit},{i,1,Length[time2]}];

Export["Outputfile2.xls ",NIcurvetable2]
```

(*Two Excel© workbooks that include the results are generated. The file, '**Outputfile1.xls**', consists of the relaxation time spectrum, τ and corresponding amplitude, in the first two columns, and R^2 in the third column. The fit to the data, calculated using the relaxation time spectrum, is given in '**Outputfile2.xls**'. The range of the fit can be changed, depending on the experimental time scale, by setting different values for "**minpower**" and "**maxpower**" in the preceding expression.*)

B.3 REFERENCES

[A.1] A. S. Argon, *Acta Metall.* **27**, 47 (1979).
[A.2] A. S. Argon, *J. Phys. Chem. Solids* **10**, 945 (1982).
[A.3] A. S. Argon and L. T. Shi, *Acta Metall*. **4**, 499 (1983).
[A.4] A. Einstein, *Annalen der Phys*. **354**, 769 (1916).
[A.5] M. A. Meyers and K. K. Chawla, *Mechanical Metallurgy: Principles and Application*, Prentice-Hall, Inc. (1983).
[A.6] R. von Mises, *Nachr. Math. Phys*. **1**, 582 (1913).
[A.7] G. E. Dieter, *Mechanical metallurgy*, McGraw-Hill (1986).
[A.8] F. Spaepen, *Lecture notes*.
[A.9] R. Hill, *The Mathematical Theory of Plasticity*, Clarendon Press (1950).
[A.10] J. D. Eshelby, *Proc. R. Soc. A* **241**, 376 (1957).
[A.11] T. Mura, *Micromechanics of defects in solids*, Springer, (1987).
[A.12] J. R. Cost, *J. Appl. Phys.* **54**, 2137 (1983).